

Astrometry and geodesy with radio interferometry: experiments, models, results

Ojars J. Sovers

Jet Propulsion Laboratory, California Institute of Technology, Pasadena, California 91109

John L. Fanselow

*Jet Propulsion Laboratory, California Institute of Technology, Pasadena, California 91109
and Remote Sensing Analysis Systems, Inc., Altadena, California 91001*

Christopher S. Jacobs

Jet Propulsion Laboratory, California Institute of Technology, Pasadena, California 91109

Interferometry at radio frequencies between Earth-based receivers separated by intercontinental distances has made significant contributions to astrometry and geophysics during the past three decades. Analyses of such Very Long Baseline Interferometric (VLBI) experiments now permit measurements of relative positions of points on the Earth's surface, and angles between celestial objects, at the levels of better than 1 cm and 1 nanoradian, respectively. The relative angular positions of extragalactic radio sources inferred from this technique presently form the best realization of an inertial reference frame. This review summarizes the current status of radio interferometric measurements for astrometric and geodetic applications. It emphasizes the theoretical models that are required to extract results from the VLBI observables at present accuracy levels. An unusually broad cross-section of physics contributes to the required modeling. Both special and general relativity need to be considered in properly formulating the geometric part of the propagation delay. While high-altitude atmospheric charged particle (ionospheric) effects are easily calibrated for measurements employing two well separated frequencies, the contribution of the neutral atmosphere at lower altitudes is more difficult to remove. In fact, mismodeling of the troposphere remains the dominant error source. Plate tectonic motions of the observing stations need to be taken into account, as well as the non-point-like intensity distributions of many sources. Numerous small periodic and quasi-periodic tidal effects also make important contributions to space geodetic observables at the centimeter level, and some of these are just beginning to be characterized. Another area of current rapid advances is the specification of the orientation of the Earth's spin axis in inertial space: nutation and precession. Highlights of the achievements of VLBI are presented in four areas: reference frames, Earth orientation, atmospheric effects on microwave propagation, and relativity. The order-of-magnitude improvement of accuracy that was achieved during the last decade has provided essential input to geophysical models of the Earth's internal structure. Most aspects of VLBI modeling are also directly applicable to interpretation of other space geodetic measurements, such as active and passive ranging to Earth-orbiting satellites, interplanetary spacecraft, and the Moon.

To be published, Reviews of Modern Physics, Vol. 70, Oct. 1998

95.75Kk, 95.70Dk, 95.10Jk

CONTENTS

I. INTRODUCTION	6
II. EXPERIMENTS AND ANALYSIS	7
A. Experiment design and data collection	8
B. Correlation: Producing the interference pattern	11
C. Post correlation: Generating the observables	12
D. Modeling and parameter estimation	13
III. GEOMETRIC DELAY MODELS	15
A. Wave front arrival time difference	17
1. Plane wave front	17
2. Curved wave front	18
3. Gravitational delay	20
B. Time information	23
C. Station locations	24
1. Tectonic plate motion	25

2.	Tidal station motion	26
a.	Solid Earth tides	26
b.	Pole tide	29
c.	Ocean loading	30
3.	Non-tidal station motion	30
a.	Atmosphere loading	31
b.	Post-glacial relaxation	32
D.	Earth orientation	32
1.	UT1 and polar motion	33
a.	Tidal UTPM variations	35
b.	Solid Earth tide UTPM variations	35
c.	Ocean tide UTPM variations	36
2.	Nutation	36
3.	Precession	39
4.	Perturbation rotation	40
E.	Earth orbital motion	41
F.	Source structure	45
G.	Antenna structure	47
IV.	INSTRUMENTAL DELAY MODELS	52
V.	ATMOSPHERIC DELAY MODELS	53
A.	Ionosphere	53
B.	Troposphere	57
1.	Mapping functions	59
2.	Limitations of mapping	60
VI.	APPLICATIONS AND RESULTS	62
A.	Reference frames	62
B.	Earth orientation and structure	65
C.	Troposphere and ionosphere	70
D.	Relativity	70
VII.	PROGNOSIS FOR FUTURE MODEL IMPROVEMENTS	71
	ACKNOWLEDGMENTS	72
	References	72

Symbols and abbreviations

A_{ij}	nutation amplitudes in longitude
\mathbf{B}	baseline vector
B_{ij}	nutation amplitudes in obliquity
BIH	Bureau International de l'Heure
BIPM	Bureau International des Poids et Mesures
CDP	Crustal Dynamics Project
CIO	Conventional International Origin
$C_{\psi j}$	planetary nutation amplitudes in longitude (Eq. 3.116)
$C_{\varepsilon j}$	planetary nutation amplitudes in obliquity (Eq. 3.117)
c	speed of light
D	mean elongation of Moon from Sun
E	elevation angle
F	latitude argument of Moon
f	flattening factor of the Earth
f	pressure loading factor
G	universal gravitational constant
GPS	Global Positioning System
GSFC	Goddard Space Flight Center
g	gravitational acceleration at Earth's surface
g	angle for barycentric dynamic time (Eq. (3.32))
H	hour angle
h	altitude above reference ellipsoid
h_{Υ}	hour angle of mean equinox of date

h_i	vertical Love number ($i = 2,3$: quadrupole, octupole)
$h_{1,2}$	ionosphere or troposphere height limits
IAU	International Astronomical Union
ICRF	International Celestial Reference Frame
IERS	International Earth Rotation Service
IRIS	International Radio Interferometric Surveying
ITRF	International Terrestrial Reference Frame
IUGG	International Union of Geodesy and Geophysics
JD	Julian date
$\hat{\mathbf{k}}$	unit vector in signal propagation direction
LLR	Lunar Laser Ranging
l	mean anomaly of Moon
l'	mean anomaly of Sun
l_E	mean longitude of Earth
l_J	mean longitude of Jupiter
l_M	mean longitude of Mars
l_S	mean longitude of Saturn
l_V	mean longitude of Venus
l_i	horizontal Love number ($i = 2,3$: quadrupole, octupole)
mas	milliarcsecond
MERIT	Monitor Earth Rotation and Intercompare Techniques
MIT	Massachusetts Institute of Technology
m	speed of precession in right ascension
m_p	mass of body p
M_w	first moment of wet troposphere refractivity
$\mathcal{M}_{d,w}$	Mapping functions for dry, wet troposphere
\mathbf{N}	nutation transformation matrix
N	atmospheric refractivity
N'	lunar node argument
NASA	National Aeronautics and Space Administration
NEOS	National Earth Orientation Service
NMF	Niell mapping function
NNR	No Net Rotation
NOAA	National Oceanic and Atmospheric Administration
NRAO	National Radio Astronomy Observatory
Nuvel	New velocity model for plate tectonics
n	refractive index
n	speed of precession in declination
\mathbf{P}	precession transformation matrix
\bar{p}	extended pressure anomaly
p_A	general precession
p_{LS}	lunisolar precession
p_{PL}	planetary precession
p_{STD}	reference atmospheric pressure
\mathbf{Q}	rotation matrix for terrestrial to celestial transformation
RA	Right ascension
R_E	Earth equatorial radius
\mathbf{R}_c	Earth center coordinates in SSB frame
\mathbf{R}_p	position of perturbing body in geocentric celestial system
$\hat{\mathbf{R}}_p$	geocentric unit vector to perturbing body
R_{EG}	distance from Earth to gravitating body G
$\hat{\mathbf{r}}$	unit vector in radial direction
r_0	classical electron radius
\mathbf{r}_0	station position in terrestrial system, excluding motions
\mathbf{r}_c	station position in geocentric celestial system

\mathbf{r}_s	phase shifted station position
$\hat{\mathbf{r}}_s$	geocentric unit vector to station position
\mathbf{r}_t	station position in terrestrial frame
$\mathbf{r}_{1,2}$	position of station 1,2 in SSB frame
\mathbf{r}_{date}	station position of date
r_{sp}	station cylindrical radius from spin axis
$S(E)$	slant range factor
S/X	S-band + X-band
SGP	Space Geodesy Project
SLR	Satellite Laser Ranging
SSB	Solar System Barycenter
S_{ψ_j}	planetary nutation amplitudes in longitude
S_{ε_j}	planetary nutation amplitudes in obliquity
$\hat{\mathbf{s}}$	geocentric celestial unit vector to source
$\hat{\mathbf{s}}_0$	SSB celestial unit vector to source
TDB	Temps Dynamique Barycentrique
TDT	Terrestrial Dynamic Time
T	time in centuries since J2000.0
t_0	reference time
t_1	time of arrival of wave front at station 1
t'_1	proper time of arrival of wave front at station 1
t_2	time of arrival of wave front at station 2
t_e	time of emission by source
t_{tr}	light transit time
\mathbf{U}	UT1 transformation matrix
U	gravitational potential
UT1	Universal Time 1
UTC	Universal Time Coordinated
UTPM	Universal Time and Polar Motion
u, v	projections of \mathbf{B} on plane of sky
\mathbf{VW}	transformation matrix from local to equatorial frame (Eqs. 3.61)
VEN	Vertical, East, North (local geodetic coordinates)
VLA	Very Large Array
VLBA	Very Long Baseline Array
VLBI	Very Long Baseline Interferometry
V_i	astronomical argument of tidal constituent i
W	atmospheric temperature lapse rate
WVR	Water Vapor Radiometer
\mathbf{X}	polar motion transformation matrix, x component
x_i, y_i, z_i	Cartesian coordinates of station i
x_i^0, y_i^0, z_i^0	Cartesian coordinates of station i at reference time t_0
$\dot{x}_i, \dot{y}_i, \dot{z}_i$	Cartesian velocities of station i
\mathbf{Y}	polar motion transformation matrix, y component
Z	auxiliary angle for precession (Eq. 3.129)
$Z_{\text{d,w}}$	zenith dry, wet troposphere delay
ZMOA	Zhu, Mathews, Oceans, Anelasticity (nutation model)
α	right ascension
α_E	equation of the equinoxes
$\beta_{1,2}$	velocity of station 1, 2
γ_{PPN}	general relativity (Parametrized Post-Newtonian) gamma factor
Δ	total tidal shift in terrestrial coordinate system
Δ_{atm}	atmospheric loading station position shift
Δ_{gd}	ionosphere contribution to group delay
Δh	height of antenna reference point above surface
Δ_{ocn}	ocean loading station position shift

Δp	local pressure anomaly
Δ_{pd}	ionosphere contribution to phase delay
Δ_{pol}	pole tide station position shift
Δ_{sol}	solid tide station position shift
$\Delta_{\mathbf{x},\mathbf{y},\mathbf{z}}$	components of perturbation rotation matrix
ΔG_p	gravitational contribution to coordinate time delay, body p
$\Delta G'_p$	gravitational contribution to proper time delay, body p
ΔU	Earth gravitational potential
$\Delta \Theta$	gravitational deflection
$\Delta \Theta_t$	tidal contribution to UTPM
$\Delta \Theta_{t'}$	companion tidal contribution to UTPM
$\Delta \psi$	nutations in (celestial) longitude
$\Delta \psi^0$	out of phase nutation in longitude
$\Delta \psi^f$	free core nutation in longitude
$\Delta \varepsilon$	nutations in obliquity
$\Delta \varepsilon^0$	out of phase nutation in obliquity
$\Delta \varepsilon^f$	free core nutation in obliquity
$\Delta \tau_s$	source structure contribution to delay
$\Delta \dot{\tau}_s$	source structure contribution to delay rate
δ	declination
δ	tidal displacement in local (VEN) coordinates
$\delta_{1,2,3}^i$	Cartesian local solid tidal displacements ($i = 2,3$: quadrupole, octupole)
$\delta \psi$	empirical correction to longitude
$\delta \varepsilon$	empirical correction to obliquity
$\varepsilon_{1,2}$	curved wave front expansion quantities (Eqs. 3.8)
$\bar{\varepsilon}$	mean obliquity
$\bar{\varepsilon}_0$	mean obliquity at J2000.0
ζ	auxiliary angle for precession (Eq. 3.128)
Θ	auxiliary angle for precession (Eq. 3.130)
Θ	gravitational deflection angle
$\Theta_{1,2,3}$	angular coordinates of Earth rotation axis
$\hat{\lambda}$	unit vector in longitude direction
λ_s	station longitude
μas	microarcsecond
μ_p	Gm_p
ν_S	S-band VLBI frequency ≈ 2.3 GHz
ν_X	X-band VLBI frequency ≈ 8.4 GHz
ν_g	electron gyrofrequency
ν_p	electron plasma frequency
ξ_{ij}	amplitude of component j of tidal constituent i
ρ	number density of electrons
Σ	SSB reference frame
Σ'	geocentric celestial reference frame
σ	correlation function
τ	geometric delay
τ_c	delay due to clock imperfections
τ_{gd}	group delay
τ_{pd}	phase delay
τ_{sr}	delay due to antenna subreflector motion
τ_{tr}	troposphere delay
$\hat{\phi}$	unit vector in latitude direction
φ_{ij}	phase of component j of tidal constituent i
ϕ_s	structure phase
ϕ_s	geocentric station latitude
$\phi_{s(\text{gd})}$	geodetic station latitude

ψ	phase shift of solid tidal effect
Ω	mean longitude of ascending lunar node
$\mathbf{\Omega}$	perturbation transformation matrix
ω_E	rotational speed of Earth
ω_f	free core nutation frequency
ω_{xyz}^j	Cartesian components of angular velocity of tectonic plate j

I. INTRODUCTION

Astrometry and geodesy have undergone a revolution during the past three decades. This revolution was initiated in the mid-1960s by the advent of interferometry at radio frequencies using antennas separated by thousands of kilometers. Developments during the following decades refined this “Very Long Baseline Interferometry” (VLBI) technique to reach its present capability of point positioning on the Earth’s surface at the centimeter level, and angular positioning for point-like extragalactic radio sources at the sub-milliarcsecond (nanoradian) level. These refinements are expected to continue until insurmountable problems are reached, probably in the sub-millimeter accuracy regime. Geodetic measurements on the Earth’s surface have been enormously expanded and densified by satellite tracking methods developed during the past decade, but VLBI remains the prime technique for astrometry employing natural radio sources. It is unique in its ability to measure the Earth’s orientation in an inertial frame of reference.

Detection and processing of the extremely weak signals from distant radio sources requires long integration times, sophisticated data acquisition systems, and customized computers. Analyses of VLBI observables involve an uncommonly broad cross-section of the disciplines of physical science, ranging from consideration of the effects of the Earth’s internal structure on its dynamics, to the tectonic plate motions and various terrestrial tidal effects, to quantification of turbulence in the atmosphere, to special relativistic description of the radio signals traveling from the distant sources, to general relativistic retardation. With the exception of gravimetric and oceanographic experiments, VLBI is perhaps the most demanding technique for many aspects of global Earth models. It therefore provides results that are used in a number of related fields. While extension of experiments to platforms in Earth orbit and elsewhere in the Solar System is in its infancy (Burke, 1991; Hirabayashi *et al.*, 1991; Adam, 1995), the present review is limited to Earth-based observations. A large portion of the modeling we shall discuss here is common to VLBI and Earth-satellite techniques such as laser ranging to reflectors on the Moon (lunar laser ranging, LLR) and ranging to passive (Lageos, SLR) and active satellites (Global Positioning System, GPS). For these reasons, it is important to review the complete details of current models of VLBI observables. Following the principle that the accuracy of a theoretical model should exceed the accuracy of the experiments which it interprets by at least an order of magnitude, the VLBI model should ideally be complete at the 1 picosecond level. Unfortunately this requirement is currently not satisfied by a number of parts of the model. As experimental techniques are refined, possibly to improve the accuracy by another order of magnitude, numerous aspects of the model will need to be re-examined.

The field of radio astronomy was initiated in the 1930s by the discovery of celestial radio emission by Jansky (1932; 1933). Development of instrumentation continued, and in the 1940s Reber (1940; 1944) used a parabolic antenna to construct the first maps of radio emission from the Milky Way galaxy at frequencies of 160 and 480 MHz. Subsequent evolution of radio astronomy through the post-war years has been traced in the comprehensive collection of memoirs edited by Sullivan (1984). Following the discovery of the powerful non-thermal radio sources called quasars (Schmidt, 1963), which are extremely distant and emit vast quantities of energy, intense interest developed in characterizing their intrinsic nature, as well as in using them as the basis for a novel astronomical reference frame. The 3rd Cambridge survey (Edge *et al.*, 1959) and the Parkes survey (Bolton *et al.*, 1979) identified many of the radio sources used today for geodetic and astrometric VLBI.

The basic ideas of the VLBI technique were first demonstrated in experiments detecting decametric bursts of Jupiter by a group at the University of Florida in 1965 (Carr *et al.*, 1965; May and Carr, 1967). Subsequent history can be traced from the first extragalactic interferometric observations by the NRAO-Arecibo group (Bare *et al.*, 1967) at 0.6 GHz on a 220-km baseline, the MIT-NRAO group (Moran *et al.* (1967); 1.7 GHz, 845 km), and the Canadian Long Baseline Interferometry group (Brotten *et al.* (1967); 0.4 GHz, 3074 km). Early work in geodesy, astrometry, and clock synchronization was done in 1969 (Hinteregger *et al.*, 1972; Cohen, 1972), yielding accuracies in distances of 2–5 meters and in source positions on the order of 1 arc second. After the first decade spent in developing the technique, numerous applications matured in succeeding years using networks of fixed antennas. Extension to

transportable antennas was also implemented during the 1970s (MacDoran, 1974; Ong *et al.*, 1976; Davidson and Trask, 1985). During that period, several basic reviews of VLBI instrumentation, experiments, and analysis appeared as chapters in the series “Methods of Experimental Physics: Astrophysics” (Meeks, 1976). Some Ph. D. dissertations of that era are those of Whitney (1974), Robertson (1975), and Ma (1978). After the currently standard Mark III VLBI data acquisition system was developed (Rogers *et al.*, 1983), large-scale international cooperation began in 1979 with the establishment of the Crustal Dynamics Project (CDP) by NASA (Bosworth *et al.*, 1993). In the 1980s, radio interferometry progressed to the point of yielding some of the most accurately measured physical quantities. Increasingly larger and more sensitive antennas were used to extend observations to ever weaker sources of emission, and the results have made important contributions to our understanding of a wide variety of astrophysical and geodynamic phenomena. Such advances in instrumentation culminated in the construction of instruments such as the Very Large Array (VLA) in 1980 (Hjellming and Bignell, 1982), and the Very Long Baseline Array (VLBA) in 1993 (Napier, 1994).

Useful references which provide an introduction to the principles of very long baseline interferometry are several articles in the above-mentioned volume 12 of “Methods of Experimental Physics” (Rogers, 1976; Pooley, 1976; Moran, 1976; Vessot, 1976; Shapiro, 1976), the book by Thompson, Moran and Swenson (1986), and two reports by Thomas (1981; 1987). Additional background material can be found in the review of geophysical VLBI applications by Robertson (1991), and in more detail and more recently, in the three-volume compilation that summarizes the accomplishments of NASA’s Crustal Dynamics Project during the past decade (Smith and Turcotte, 1993). Various periodic reviews, including the quadrennial IUGG geodesy reports (Clark (1979), Carter (1983); Robertson (1987); Ray (1991); Herring (1995)), the IERS annual reports (*e.g.* IERS, 1996a), and the yearly reports on CDP results [*e.g.* Ma *et al.* (1992), more recently at <http://lupus.gsfc.nasa.gov/vlbi.html>], are also good sources for detailed information concerning current VLBI techniques and results. The International Earth Rotation Service (IERS) periodically publishes a compilation of standard models recommended for analyses of space geodetic data (1992; 1996b); also available at <http://maia.usno.navy.mil/conventions.html>. In large part, the model description in the present paper is in agreement with the specifications of these “IERS Standards”.

The intent of this paper is to review astrometric and geodetic VLBI from a description of the experiments through analysis of the results, with emphasis on the details of theoretical modeling. Section II summarizes experiment design, single-station signal collection and recording, signal combination, and observable extraction. This section also reviews the general approach to extracting parameters of astrometric and geodetic interest from the observables. The three succeeding sections (III-V) consider the theoretical model in detail, partitioning the interferometric delay model into three major components: geometry, instrumentation (clocks), and atmosphere, and presenting the best current models of each of these components. The longest section (III) deals with the purely geometric portion of the delay, wave front curvature, and gravitational bending, and considers time definitions, tectonic motion, tidal and source structure effects, coordinate frames, Earth orientation (universal time and polar motion), nutation, precession, Earth orbital motion, and antenna offsets. Sections IV and V discuss the non-geometric components of the model: clocks and the atmosphere. Section VI presents a brief overview of the accomplishments of VLBI and its contributions to our understanding of astrometry and geophysics during the past two decades. Section VII outlines model improvements that we anticipate will be required by more accurate data in the future.

The most convenient units for use in astrometric and geodetic VLBI are millimeters, picoseconds, and nanoradians. The first two are connected by the speed of light = 299,792,458 m/s \approx 1 mm/3 ps, and will be used interchangeably. Most commonly for the purposes of illustration, a 10,000-km baseline will be considered. A length change of 1 cm on such a baseline is equivalent to an angular change of 1 nrad (1 part per billion, ppb) or 0.2 milliarcseconds (mas); the equivalent conversion factors in millimeters are 10 mm/nrad or 50 mm/mas.

II. EXPERIMENTS AND ANALYSIS

Interferometric measurements permit resolution on the order of the wavelength of the radiation. For radio waves at the typical astrometric/geodetic frequencies of 2.3 GHz (S band) and 8.4 GHz (X band), the wavelengths are 13 and 3.5 cm, respectively. Some recent activity is focusing on even higher frequencies (*e.g.* Lebach *et al.*, 1995), and numerous interferometric observations are planned at millimeter wavelengths, spanning the gap between the radio and optical regions. For experiments that are dominated by random errors, gains can be achieved by repeated measurements, thereby reducing the errors substantially. Thus, the accuracy at X band may be expected to surpass 1 cm in many cases.

Early radio interferometric experiments employed antennas that were separated by distances on the order of 1 km. These experiments had the advantage that the stations shared a frequency standard, and signal correlation

was performed in real time (*e.g.* Batty *et al.*, 1982). Such an arrangement is now known as a “connected element interferometer” to distinguish it from interferometers with separated elements that are not in direct communication. A connected element interferometer is a close analogue of the Michelson stellar interferometer which manipulates signals with mirrors to produce a physical interference pattern at the detector. Frequency standards (“clocks”) and the technology associated with measurements at centimeter wavelengths improved dramatically as a result of radar development during World War II. It became possible to separate the two components of the interferometer with independent clocks and instrumentation, and to use high-speed data recording techniques, thus eliminating the need for close physical proximity. With such an arrangement there are no physical real-time interference “fringes”, although the terminology of optical interferometry has been carried over to the radio wavelength region. Remote radio interferometry is now commonplace. With the two antennas separated by long baselines, the experimental observables are no longer obtained in real time, but are instead generated by subsequent analysis of recorded information. Such experiments have become known as “very long” baseline interferometry or VLBI. With the recent explosive advances in communications, computing, and data storage technology, connected element experiments over intercontinental distances may again become standard in the future.

Large dish antennas (20 to 100 m in diameter) that are used for radio astronomy and VLBI are found in approximately 50 globally distributed locations. An equivalent number of sites have been occupied by smaller transportable antennas during the past two decades. The premier sites are at relatively high altitudes and in arid climates, which were selected to minimize the impact of atmospheric turbulence on measurement quality.

A. Experiment design and data collection

A diagram of a contemporary VLBI experiment is sketched in Fig. 1. Two antennas, separated by a baseline \mathbf{B} , are simultaneously pointed at the same radio source, and detect the incoming wave front propagating along unit vector $\hat{\mathbf{k}}$.

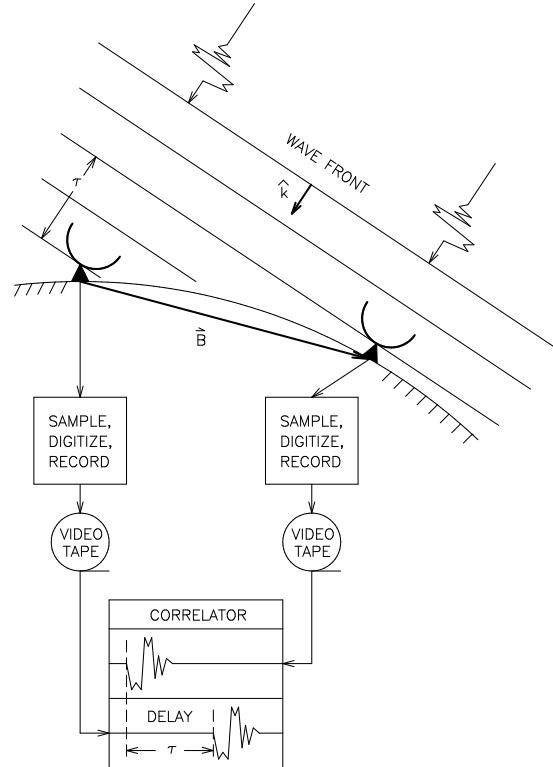


FIG. 1. Schematic diagram of a VLBI experiment. Waveforms are shown impinging from the direction $\hat{\mathbf{k}}$ on two antennas separated by a baseline \mathbf{B} on the Earth’s surface. They are followed through the data acquisition system to the point where the correlator determines the delay τ . The signal waveforms are exaggerated for effect. The actual waveforms are random Gaussian processes.

More than two antennas (stations) commonly participate in an experiment, but its fundamentals can be adequately illustrated by considering only one of the many pairs of stations. Prior to its arrival at the first antenna, the signal has already been affected by the electromagnetic and gravitational fields that it encountered along its journey through interstellar space, the Solar System, and the Earth’s atmosphere. Between this time and the time of reception at the second antenna, any motions of the Earth also make their influence felt. All these varied aspects need to be taken into account in analyses of the experiment. We note that the VLBI technique is differential in the sense that the observables depend on the *relative* station locations and source positions, but they are fairly insensitive to the stations’ absolute geocentric locations and the origin of right ascension (celestial longitude). Other techniques (*e.g.*, SLR, GPS) must supply such information, which minimally consists of the geocentric position of one of the observing stations at a given epoch, and the right ascension of one source.

The information content of the VLBI observables depends critically on the design of the experiment (*e.g.* Shapiro, 1976). The observing schedule (station network, observation epochs, and local azimuth and elevation angles of the selected sources) plays a crucial role in determining the types and precision of parameters that can be extracted in the subsequent data analyses. At a bare minimum there must be at least one observable for each parameter to be estimated. The experimenter must first decide how many parameters he wishes to measure. To consider a simple example: after having fixed the station location and clock parameters of a reference station, a typical astrometric or geodetic analysis will want to estimate, at a minimum, for each of the remaining stations three site coordinates, a zenith tropospheric delay parameter, and linear clock parameters (offset and rate). In addition to these station-specific parameters, a number of “global” parameters are also usually estimated. These are common to the entire network, and describe the orientation of the Earth (5 parameters) and the positions of the sources (2 angular parameters per source); the right ascension of one source must be fixed to establish the origin of the celestial reference frame. Thus for an experiment with N stations and M sources, there would be N_p parameters to determine, where $N_p = 6N + 2M - 1$. In recent years, analyses have tended to estimate increasingly larger numbers of station-specific parameters for the clocks and tropospheres, thereby increasing the coefficient of the N term many-fold.

Note that the observable delay in arrival times is approximately proportional to the scalar product of the baseline and signal propagation vectors, and thus contains information concerning both the station and source coordinates. With sufficiently redundant measurements, therefore, both the station and source coordinates are accessible to estimation, subject to the limitations imposed by only observing the scalar product. Naturally, it is highly desirable to have more observables than the minimum (N_p) required for a non-singular solution in the analysis. The additional observables permit reduction of the formal statistical uncertainties in the estimated parameters. They also allow the level of systematic errors to be characterized using various tests of the repeatability of the results. Such tests may include root-mean-square of the residuals (observed minus theoretical) and repeatability of estimated parameters derived from subsets of the data. Excess observables also leave open the option of estimating additional parameters whose importance may become known only after the data are collected. For all these reasons, the experiment design usually provides for many more observables than the expected number of parameters. In fact, a typical astrometric/geodetic experiment will have several hundred observables per baseline.

Given a network of stations, how are the source observations chosen? To answer this question, and to generate an optimal observing schedule, the experimenter is guided by a few key principles. First the experiment must have sufficient spatial and temporal sampling in order to permit unambiguous separation of the parameters of interest during analysis. As an example of the need for good spatial sampling, consider the dry zenith tropospheric delay parameter Z_d and the station local vertical coordinate v . The measured delays τ will have sensitivities to these parameters that scale approximately as

$$\partial\tau/\partial Z_d \propto 1/\sin E \tag{2.1}$$

$$\partial\tau/\partial v \propto -\sin E, \tag{2.2}$$

where E is the elevation angle above the horizon. These two parameters will be correlated if E is sampled only close to 45° . In order to separate the parameters the experiment must observe sources over a wide range of elevations. In particular the low-elevation ($E < 10^\circ$) measurements will be most sensitive to the troposphere, while those at higher elevation angles will be most sensitive to the station vertical coordinate.

Next we consider the need for good temporal sampling. Simply put, the experiment must sample the parameter of interest more quickly than it changes. For periodic effects this implies that one must take at least two samples within one full period of the effect of interest. In astrometric and geodetic VLBI one is often interested in tides with periods of 12 and 24 hours, 2 weeks, 1 month, a half a year, and one year. Components of the Earth’s nutation have periods ranging from days up to 18.6 years. In practice experiments collect data at the rate of many observations per hour for a full 24-hour session. Such sessions have been carried out many times per year during the last two decades,

allowing VLBI to measure parameters which vary on all of the aforementioned time scales. Day-long experiments also have the benefit of allowing observations through the full range of source right ascension. This minimizes problems that would otherwise arise in connecting observations from one right ascension zone to another. As a result, VLBI can avoid the zonal RA errors that have plagued optical observations which can only be performed at night. Because VLBI measurements are done at microwave frequencies, they are also much less sensitive to weather (clouds, rain) than optical techniques.

The experimenter must next decide how long to observe each source. While collecting more data bits improves the detection signal-to-noise ratio (SNR), the desire to increase the SNR must be balanced against the reality of finite recording bandwidths which are 50-100 Mbits/sec for the Mark III VLBI system (Rogers *et al.*, 1983). As a result the optimal integration times typically range from 2 to 13 minutes. A technique known as bandwidth synthesis (Rogers, 1970) provides the highly accurate delays possible with a large radio frequency bandwidth, while requiring a recording bandwidth that is only a small fraction of the former. This technique has been essential in overcoming the limitations of currently available recording bandwidths. For very weak sources, much longer integration times may be required. The coherent integration time may be extended considerably with the phase referencing technique (Lestrade *et al.*, 1990), in which a strong nearby source is observed alternately with the weak source, and the phase of the strong source is used as a reference.

Lastly, we consider how best to use a given network of antennas. For antennas separated by a few thousand kilometers or less it is often practical to have all antennas simultaneously observing the same source. With such modest baselines, each station can observe over a broad spatial extent. However, for networks with baselines significantly longer than an Earth radius, the desires for simultaneous visibility of the source and for broad geometric coverage start to be in conflict. Because the area of the sky that is simultaneously visible from both observing sites shrinks rapidly as baselines approach an Earth diameter in length, options for observing strategies become severely limited. The solution has been to create “sub-networks”. This observing strategy assigns a subset of the stations in the network to observe one source, while another subset of stations observes a different source. While this complicates the experiment logistics, it has allowed the design of experiments with very strong geometries.

Having considered the experiment design, we will now discuss how the signal is detected and recorded. For a Cassegrain antenna (see Fig. 9 in Sec. III.G), the incoming signal first strikes the primary paraboloidal dish of the antenna, is then reflected up to the hyperboloidal subreflector, and finally into the feed horn on the central axis. For a prime focus antenna, the signal goes directly from the paraboloidal reflector to the feed at the focus position. Past the feed horn, the signal undergoes an initial stage of amplification, either by transistor amplifiers such as field-effect or high-electron-mobility transistors or by a traveling wave maser. System temperatures typically range from 20-100 K at S and X band. After the first stage of amplification the signal is heterodyned from radio frequency to a lower intermediate frequency of several hundred MHz. Next the signal is further heterodyned down to “video” frequencies. There the signal is band limited to a width of a few MHz, sampled, and digitized. Lastly, it is formatted and recorded on digital video tape (see the lower half of Fig. 1).

The signal is digitized at a minimum level of quantization to make the most effective use of the limited recording bandwidth. The digitized signals are recorded on high capacity video tapes for a period of several minutes, yielding a total of ≈ 10 gigabits of data. In routine observing sessions lasting 24 hours, this procedure is repeated many times, with as many as a hundred distinct sources sampled at several distinct hour angles. Note that the independent station clocks must remain well enough synchronized to obtain signal samples that will form a coherent interference pattern. The signal flux density is on the order of 1 Jansky ($\text{Jy} = 10^{-26} \text{ W m}^{-2} \text{ Hz}^{-1}$), necessitating antennas with large collecting areas and high sampling and recording rates, as well as highly sensitive and stable detectors and frequency standards. Pointing and mechanical characteristics of the antenna structure must be sufficiently responsive to permit movement between sources widely separated in the sky within a few minutes.

The fundamental measurement in VLBI times the arrival of the wave front at the two ends of the baseline. In order to take full advantage of the timing precision possible with current frequency standards (*e.g.*, hydrogen masers stable to 1 part in 10^{14}) care must be taken to calibrate phase shifts induced by the measurement instrumentation. Such phase shifts can corrupt the estimated phase and hence the group delay of the incoming signal. In order to correct for these instrumental phase shifts a technique known as phase calibration has been developed (Rogers, 1975; Fanselow, 1976; Thomas, 1978; Sigman, 1987). This technique compensates for instrumental phase errors by generating a signal of known phase, injecting this signal into the front end of the VLBI signal path, and examining the signal’s phase after it has traversed the instrumentation. This calibration signal is embedded in the broadband VLBI data stream as a set of low level monochromatic “tones” along with the signal from the radio source. Typically the calibration signal power is $< 1\%$ of the broadband VLBI signal level. The tones are extracted from the data at the time of subsequent processing.

B. Correlation: Producing the interference pattern

After the signals at each antenna site are collected and recorded, the next step initiates the analysis of a VLBI experiment. The signals recorded at all participating antennas are combined pairwise, thereby producing the interference pattern. This progression is shown in Fig. 1. The facilities for signal combination are called correlators. Several such installations are presently operating in the U. S. A. (Haystack Observatory, Jet Propulsion Laboratory, U. S. Naval Observatory, Very Long Baseline Array), Germany (Bonn), and Japan (Kashima). They consist of special-purpose signal processing hardware which is used to determine the difference in arrival times at the two stations by comparing the recorded bit streams. Moran (1976) and Thomas (1980; 1981; 1987) discuss the details of this process. In brief, the two bit streams representing the antenna voltages as functions of time t , $V_1(t)$ and $V_2(t)$, are shifted in time relative to each other until their cross-correlation function R is maximized:

$$R(\tau) = \frac{1}{T} \int_0^T dt V_1(t) V_2^*(t - \tau) . \quad (2.3)$$

T is the averaging interval, $*$ denotes complex conjugate, and the time τ corresponds to the difference in arrival times (the normalization is arbitrary for the purposes of our present discussion).

Following Thomas (1987), a simplified diagram of the processing of data bits in a VLBI correlator is shown in Fig. 2. For purposes of this illustration we have only shown 8-bit averaging, one trial delay offset (known as a “lag”), artificially small delays, high fringe rates, and large amplitudes. Various fixed delays which occur in actual implementations are omitted in order to emphasize only the essential steps.

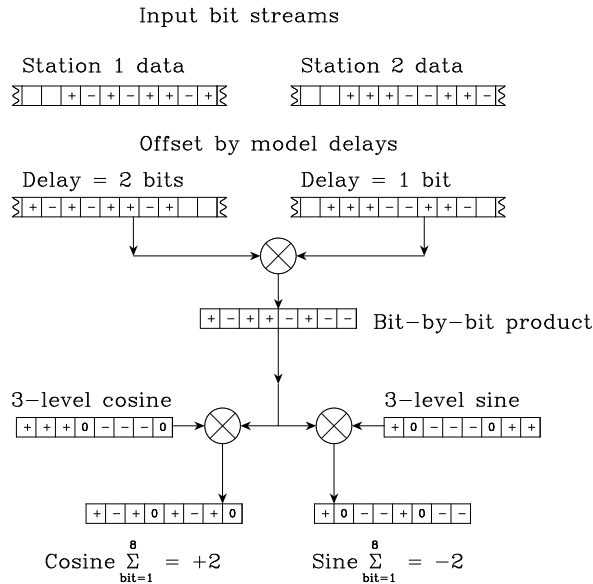


FIG. 2. Functional diagram of a VLBI correlator. The input bit streams are processed to the point of yielding the sine and cosine correlation sums.

Starting at the top, Fig. 2 shows a short segment of the bit stream from each of two stations. The data were recorded using 1-bit sampling; when the signal voltage $V > 0$ the bit is “+”, and when $V < 0$ the bit is “-”. Some of the bit locations have been left blank in this illustration, in order to show more clearly only the eight bits that are followed through all steps of the example. In the second step, the bit streams have been delayed by 2 bits for station 1 and by 1 bit for station 2. In reality these delays are typically on the order of 10^5 bits, where one bit is recorded every $0.25 \mu\text{s}$. In step 3, the two bit streams have been cross-correlated. The resulting product is “+” when the corresponding bits from the two streams match, and “-” when they differ.

Since the Earth’s rotational velocity induces Doppler shifts on the order of 10^{-6} times the observing frequency, VLBI observations at X band (8.4 GHz) will have their signals oscillating at several kHz. VLBI signals are typically very weak (only 1 bit in 10^3 or 10^4 correlates between the two stations), and one must therefore average over many bits to detect the signal. To achieve this the signals must first be “counter-rotated”. This involves multiplying the

cross-correlated bits by sine and cosine waves to remove the above-mentioned Doppler shifts. Thus counter-rotation may also be thought of as a digital heterodyning of the cross-correlation signal from kHz to near zero frequency. In step 4, the bits are counter-rotated by multiplying them with 3-level approximations of sine and cosine waves. (This counter-rotation can also be performed prior to cross-correlating in step 3). Step 5: having been counter-rotated, the signal may now be averaged over many bits in order to allow the weak VLBI signals to be detected. For clarity the diagram shows averaging over only eight bits. The resulting cosine and sine sums are then root-sum-squared and normalized to obtain the signal amplitude, and the arctangent (sine/cosine) is taken to yield the signal's phase. Note that for the purposes of this illustration the signal amplitudes are unrealistically large.

Several aspects of the process described above distort the extracted signal and must be accounted for. First we note that 1-bit sampling causes a loss in SNR and introduces a $2/\pi$ scale factor in the amplitudes (van Vleck and Middleton, 1966). The quantization of the delay to steps of one bit changes both the amplitude and phase, while the use of a 3-level approximation to the sine and cosine functions scales the amplitude. Thomas (1980; 1987) and Thompson, Moran and Swenson (1986) discuss these effects and their rectification in detail.

C. Post correlation: Generating the observables

The correlation process is carried out in parallel for many (typically 14) frequency channels, with each channel producing average amplitudes and phases every 1-2 seconds, as described in the previous section. These results are stored for later analyses with post-correlation software, which is discussed in detail by Lowe (1992). Briefly, such code performs many functions in order to prepare the data for the final processing by the modeling/estimation software. Some of these tasks are rejection of unreliable data by means of statistical tests, establishment of reference times t_0 and frequencies ω_0 for the observables, phase calibration via the tones that were injected soon after signal detection, and removal of any rudimentary model information that was introduced during correlation. The core task of the post-correlation software is to take the set of phase samples $\phi(\omega_i, t_j)$ from the various frequency channels ω_i and times t_j , and to fit the set of $\phi(\omega_i, t_j)$ with three parameters: the phase ϕ_0 , the group delay τ_{gd} , and the phase rate $\dot{\tau}_{\text{pd}}$. To accomplish this, the set of $e^{i\phi(\omega_i, t_j)}$ are first Fourier transformed from the frequency and time domain to the delay and delay rate domain respectively. Figure 3 shows the result of this operation for a high-SNR observation. Next the delay and delay rate domain data are searched for peaks (at 763.784 ns, -0.3878 ps/s for the example in Fig. 3). This peak supplies the *a priori* values for a least squares fit which determines the observables ϕ_0 , τ_{gd} , and $\dot{\tau}_{\text{pd}}$ (phase, group delay, and phase delay rate).

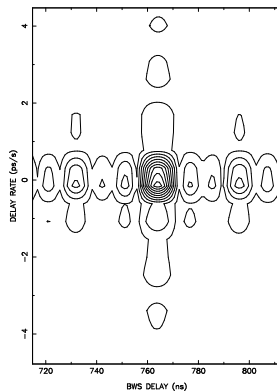


FIG. 3. Fourier transform of the phase $\phi(\omega_i, t_j)$ into the delay, delay rate domain.

These phase-derived observables are determined (for phase ϕ and circular frequency ω) from a bilinear least-squares fit to the measured phases $\phi(\omega, t)$:

$$\phi(\omega, t) = \phi_0(\omega_0, t_0) + \frac{\partial\phi}{\partial\omega}(\omega - \omega_0) + \frac{\partial\phi}{\partial t}(t - t_0) , \quad (2.4)$$

where the phase, group delay, and phase rate are respectively defined as

$$\tau_{\text{pd}} = \phi_0/\omega, \quad \tau_{\text{gd}} = \frac{\partial\phi}{\partial\omega}, \quad \dot{\tau}_{\text{pd}} = \frac{\partial\phi}{\partial t}. \quad (2.5)$$

Formal uncertainties of each observable are also produced (for the example in Fig. 3, $\sigma_{\tau_{\text{gd}}} = 0.010\text{ns}$, $\sigma_{\dot{\tau}_{\text{pd}}} = 0.0008\text{ps/s}$). When data at two distinct frequencies are present (*e.g.*, S and X bands), charged particle (ionospheric) effects are removed by applying a simple model of dispersion, and combined (S/X) observables are formed (see Sec. V.A, Eq. 5.11). Problems with resolving 2π ambiguities in the signal phase over large distances usually preclude the direct use of the phase delay observable τ_{pd} . This problem can be overcome in differenced observations of pairs of nearby sources, for which “phase connection” is possible (Marcaide *et al.*, 1994). Under routine conditions, the uncertainties in the delay observables are on the order of 10 picoseconds. Numerous aspects of hardware, instrumentation, and software contribute to this limit (Rogers, 1991). During correlation and post-correlation processing, the amount of data is compressed by a factor of 10^9 , from terabits to kilobits.

To summarize, the interferometer is capable of producing four data types: phase delay, group delay, phase delay rate, and amplitude. The time rate of change of group delay cannot be measured accurately enough to be useful for geodetic or astrometric purposes. The delay models discussed in Secs. III, IV, and V are directly applicable to either group delay or to phase delay. Amplitudes are not usually modeled in astrometric/geodetic VLBI [for an exception see Charlot (1990a; 1990b)]. Phase delay rate models may be built from the delay models as discussed immediately below.

The model for the time rate of change of phase delay must be constructed from either analytical or numerical time derivatives. If the latter route is taken, then only models of delay are needed. The model phase delay rate $\dot{\tau}_{\text{pd}}(t)$ is approximated as a finite difference R by

$$R = [\tau_{\text{pd}}(t + \Delta) - \tau_{\text{pd}}(t - \Delta)]/(2\Delta). \quad (2.6)$$

In the limit $\Delta \rightarrow 0$, this expression for differenced phase delay approaches the instantaneous time rate of change of phase delay (fringe frequency) at time t . In practice, Δ must be large enough to avoid roundoff errors, but should also be small enough to allow R to be a reasonably close approximation to the instantaneous delay rate. A suitable compromise appears to be a Δ in the vicinity of 0.1 second. Fortunately, the capability to model interferometer performance accurately is relatively insensitive to the choice of Δ over a fairly wide range of values. To be specific, if $\tau_{\text{pd}}(t)$ is expanded to third order in Δ , the numerically evaluated rate becomes

$$R = \dot{\tau}_{\text{pd}}(t) + \ddot{\tau}_{\text{pd}}(t) \Delta^2/6. \quad (2.7)$$

Thus the error made in approximating the time derivative as R is proportional to $\ddot{\tau}_{\text{pd}}\Delta^2$. This term amounts to a few times 10^{-16} s/s for a 10,000 km baseline and $\Delta = 0.1$ s. Comparisons of numerical and analytic derivatives have demonstrated equivalence of the two methods to better than 10^{-15} s/s.

D. Modeling and parameter estimation

Prior to the detailed exposition in the next three sections of the theoretical modeling required by geodetic and astrometric VLBI, we present a brief summary of the VLBI modeling and parameter estimation process, its history, and key references. To form a perspective, we start by listing in Table I the approximate relative importance of the various portions of the VLBI model. Each tabulated maximum delay is given in distance units, and represents the potential model error that would be caused by its complete omission from the theoretical model. Of the seven major components in this table, the purely geometric delay clearly dominates, since it can approach one Earth diameter. Aberration effects due to the Earth’s orbital motion are four orders of magnitude smaller. The remaining components range over several orders of magnitude, with Earth orientation, antenna structure, instrumentation, and atmospheric effects being the most important. Most portions of the station coordinate and Earth orientation models become significant only in analyses of data extending over time spans much longer than a typical observing session of 24 hours. The maximum delays arising from these models were therefore estimated for data extending over one year. Models of the last four major categories, on the other hand, can exhibit their total variation over the duration of one experiment, and their maximum contributions were therefore estimated over a time span of one day.

We also attempt to provide an “error budget” for the VLBI model by tabulating rough estimates of modeling uncertainties in the last column of Table I. Extreme situations are considered for these estimates: Earth-sized baselines, extended sources, large antenna axis offsets, uncalibrated instrumentation, and observations at low elevations. It will be noted that many of the components can be modeled to accuracies that are several orders of magnitude better than

their maximum contributions. Thus, while this table indicates the general significance of the physical effects, their ranking does not necessarily reflect the uncertainties of their contributions to VLBI observables. Interactions between theory and experiment are quite important in interpretation of VLBI measurements: empirical analyses point out inadequate parts of the model, which can then be improved. Such iteration has taken place to varying degrees for different model components. Presently, each of the three basic aspects of a VLBI measurement (source, intervening medium, and receiver) are seen to impose limits to VLBI resolution and accuracy that are roughly of comparable magnitude.

The effort expended in improvement of various model components has by no means been proportional to their relative contributions to the observables. For example, the ionosphere can be nearly totally eliminated as an error source if the measurements are performed at two widely separated frequencies. In recent years, much more attention has focused on station motion effects, despite their smaller size. While recent methods of treating Earth orientation and troposphere errors have produced substantial reductions of their contributions to the VLBI error budget, they nevertheless remain as two of the leading error sources in contemporary VLBI analyses. Two other important errors are due to incomplete modeling of the time-dependent structures of the radio sources and receiving antennas. Both may amount to tenths of a milliarcsecond (mas) (1 nrad, many mm). For day-long Earth-based measurements, the dominant error is due to the troposphere: commonly used models of atmospheric propagation can be incomplete at nearly the 10-20 mm level. In fact, present troposphere modeling is probably less accurate than the formal precision of the VLBI observables. Details of tidal motions on the Earth's surface have also not been fully characterized at the few mm level. For longer periods (on the order of 1 year), aperiodic time-dependent processes come into play. At present, these are likewise not well enough understood *a priori* at the nrad or mm level. The error budget of Table I leads to a (conservative) total modeling uncertainty of approximately 30 mm. More complete models of the Earth's tidal response and atmosphere, the physical processes in quasars, and the mechanical response of large antenna structures, will be required to realize the full potential accuracy of the VLBI technique and to reduce this limit to below 10 mm. It is hoped that this review provides a good point of departure for such model improvements.

The *a priori* model is refined by estimating model parameter corrections which best fit the data. In astrometric and geodetic applications of radio interferometry, the values of the observables from many different radio sources are processed by a multiparameter least-squares estimation algorithm to extract refined model parameters. As the accuracy of the observables improves with advances in instrumentation, increasingly complete models of the delays and delay rates need to be developed, which will be the thrust of this review.

Linear least-squares methods are employed to extract the best estimates of model parameters from the VLBI observables. Fortunately, nonlinearities in this mathematical problem are small, and the *a priori* knowledge of most aspects of the model is sufficiently good to permit efficient estimation via linearized least squares. The only operational complication is caused by the sheer volume of data: more than two million pairs of delay and delay rate observations have been accumulated in experiments through 1997. This necessitates careful bookkeeping procedures to keep computing requirements manageable when tens or hundreds of thousands of parameters are estimated in simultaneous analyses of all extant data. The most important of these is the separation of the parameters into "local" and "global" categories in order to minimize the need to invert very large matrices. For example, in processing data which extend over many observing sessions, the clock and atmosphere model parameters apply only to individual sessions, while station and source coordinates might be determined by the entire data set. Specialized least-squares or filtering methods are usually employed in VLBI parameter estimation. Particular attention needs to be paid to numerical stability, and to retaining correlation information in experiments that are widely separated in time. The "square root information filter" (SRIF) (Bierman, 1977) is one such formalism for achieving these goals.

Severe limitations are imposed on the information content of the VLBI observables by the fact that the geometric delay measures only the scalar product of the baseline and source direction vectors. Thus the data determine the *relative* directions of the sources and baseline, and only the orientation of the whole Earth relative to the sources is strongly determined. Weak ties of the baseline to geographic features of the Earth are provided by effects such as the Earth's motion in its orbit (aberration), tidal displacements, and tropospheric delay. These fix the baseline in the terrestrial frame at an uncertainty level of a few tenths of an arcsecond. A more rigid link can only be provided by the introduction of a reference station with known coordinates (*e.g.*, from satellite techniques) in the terrestrial reference frame, and the adoption of a conventional origin for celestial orientation (*e.g.*, the right ascension of one reference source).

A further complication in analysis is introduced by degeneracy in the parameter space of the multi-faceted model. Linear combinations of a subset of the parameters describing one portion of the model may produce identical changes in the observables to those described by parameters of another portion of the model. The tidal displacements of a global network of stations provide an illustrative example: certain linear combinations of station tidal motions are

equivalent to the three components of rotation of the Earth as a whole. All such potential degeneracies must be identified and accounted for in parameter estimation procedures.

The account of the physical models presented here is intended to be helpful in providing a general understanding of the analysis of VLBI observations. Since modeling is intimately connected to the software that is used for data analysis, we take advantage of our own experience and adhere to the outline of the mathematical description of model implementation for the multiparameter estimation code “Masterfit/Modest” (Fanselow, 1983; Sovers and Jacobs, 1996) in the succeeding sections. The theoretical foundation of this large-scale computer implementation was laid by J. G. Williams (1970a), who also developed many of the original algorithms. Software and model development has continued at the Jet Propulsion Laboratory since the 1970s. Independent code of similar scope and ancestry is the “Calc/Solve” package, which was developed at the Goddard Space Flight Center (GSFC) during the same time period (GSFC, 1981). This software has been used in the National Aeronautics and Space Administration (NASA) Crustal Dynamics and Space Geodesy Projects (CDP and SGP), National Oceanic and Atmospheric Administration (NOAA) International Radio Interferometric Surveying (IRIS), and National Earth Orientation Service (NEOS) analyses. It is an outgrowth of the original algorithms of Hinteregger *et al.* (1972) and Robertson (1975), and has been evolving predominantly at the Goddard Space Flight Center. Numerous mutations of Calc/Solve over the years have resulted in at least three related, but not identical, packages used for VLBI analyses in Germany (Campbell, 1988), Japan (Kunimori *et al.*, 1993), and Spain (Zarraoa *et al.*, 1989). More recently, independent software has been developed in Ukraine (Yatskiv *et al.*, 1991), France (Gontier, 1992), Norway (Andersen, 1995), and Russia (Petrov, 1995). There have been occasional comparisons between the various codes (Sovers and Ma, 1985; Gontier, 1992; Rius *et al.*, 1992). These comparisons have been beneficial in exposing discrepancies, correcting software problems, and clarifying the physical models. Such discrepancies have been surprisingly minor, given the complexity of these large computer programs.

III. GEOMETRIC DELAY MODELS

The geometric delay is defined as the difference in time of arrival of a signal at two geometrically separate points which would be measured by perfect instrumentation, perfectly synchronized, if there were a perfect vacuum between the observed extragalactic or Solar-System source and the Earth-based instrumentation. For Earth-fixed baselines, this delay is at most the light time of one Earth radius (20 milliseconds) due to non-transparency of the Earth. It can change rapidly (by as much as $3 \mu\text{s}$ per second) as the Earth rotates. While VLBI experiments are occasionally carried out with more than ten participating stations, the correlator generates observable delays and their time rates of change independently for each baseline connecting a pair of stations. Without loss of generality, the delay model can thus be developed for a single baseline involving only two stations, which is what we present here. The geometric component is by far the largest component of the observed delay. The main complexity of this portion of the model arises from the numerous coordinate transformations that are necessary to relate the celestial reference frame used for locating the radio sources to the terrestrial reference frame in which the station locations are represented.

We use the term “celestial reference frame” to denote a reference frame in which there is no net proper motion of the extragalactic radio sources which are observed by the interferometer. This is only an approximation to some truly “inertial” frame. Currently, this celestial frame is a Solar-System-barycentric (SSB), equatorial frame with the equator and equinox of Julian date 2000 January 1.5 (J2000.0) as defined by the 1976 International Astronomical Union (IAU) conventions, including the 1980 nutation series (Seidelmann *et al.*, 1992; Kaplan, 1981). In this equatorial frame, some definition of the origin of right ascension must be made. The right ascension is nearly arbitrary (neglecting small aberrational, tidal, and gravitational bending effects due to the Earth’s changing position within the Solar System). Any definition differs by a simple rotation from any other definition. The important point is that consistent conventions must be used throughout the model development. The need for this consistency has recently led to a definition of the origin of right ascension in terms of the positions of extragalactic radio sources (Ma *et al.*, 1997). Interferometric observations of both natural radio sources and spacecraft at planetary encounters will then connect the optical reference frame and planetary ephemeris with the radio reference frame (Newhall *et al.*, 1986; Folkner *et al.*, 1994; Lestrade *et al.*, 1995).

Unless otherwise stated, we will mean by “terrestrial reference frame” a frame tied to the mean surface features of the Earth. The most common such frame, which we use here, is a right-handed version of the Conventional International Origin (CIO) reference system with the pole defined by the 1903.0 pole. In practice, the tie is most simply realized by defining the position of one of the interferometric observing stations, and then determining the positions of the other stations under this constraint. This tie further requires that the determinations of Earth orientation agree on the average with measurements of the Earth’s orientation by the International Earth Rotation Service (IERS) (1996a)

[and its predecessor, Bureau International de l'Heure (BIH) (1983)] over some substantial time interval (\approx years). Such a procedure, or its functional equivalent, is necessary to tie the measurement to the Earth, since the interferometer is sensitive only to the baseline vector. With the exception of minor tidal and tropospheric effects, the VLBI technique does not have any preferred origin relative to the structure of the Earth. The rotation of the Earth does, however, provide a preferred direction in space which can be associated indirectly with its surface features.

In contrast, geodetic techniques which involve the use of artificial satellites or the Moon are sensitive to the center of mass of the Earth (*e.g.* Vigue *et al.*, 1992) as well as its spin axis. Thus, such techniques require only a definition of the origin of longitude. Laser ranging to the retroreflectors on the Moon allows a realizable definition of a terrestrial frame, accurately positioned relative to a celestial frame which is tied to the planetary ephemerides (Folkner *et al.*, 1994). The required collocation of the laser and VLBI stations is being provided by Global Positioning Satellite (GPS) measurements of baselines between VLBI and laser sites starting in the late 1980s (*e.g.* Ray *et al.*, 1991). Careful definitions and experiments of this sort are required to realize a coordinate system of centimeter accuracy.

Except for sub-centimeter relativistic complications caused by the locally varying Earth potential (as discussed below), construction of the VLBI model for the observed delay can be summarized in 7 steps as:

1. Specify the proper locations of the two stations as measured in an Earth-fixed frame at the time that the wave front intersects station 1. Let this time be the proper time t'_1 as measured by a clock in the Earth-fixed frame.
2. Modify the station locations for Earth-fixed effects such as solid Earth tides, tectonic motion, and other local station and antenna motion.
3. Transform these proper station locations to a geocentric celestial coordinate system with its origin at the center of the Earth, and moving with the Earth's center of mass (but not rotating). This is a composite of 12 separate rotations.
4. Perform a Lorentz transformation of these proper station locations from the geocentric celestial frame to a frame at rest relative to the center of mass of the Solar System, and rotationally aligned with the celestial geocentric frame.
5. In this Solar-System-barycentric (SSB) frame, compute the proper time delay for the passage of the specified wave front from station 1 to station 2. Correct for source structure. Add the effective change in proper delay caused by the differential gravitational retardation of the signal within the Solar System.
6. Perform a Lorentz transformation of this SSB geometric delay back to the celestial geocentric frame moving with the Earth. This produces the adopted model for the geometric portion of the observed delay.
7. To this geometric delay, add the contributions due to clock offsets (Sec. IV), to tropospheric delays, and to the effects of the ionosphere on the signal (Sec. V).

As indicated in step 5, the initial calculation of delay is carried out in a frame at rest relative to the center of mass of the Solar System (SSB frame). First, however, steps 1 through 4 are carried out in order to relate proper locations in the Earth-fixed frame to corresponding proper locations in the SSB frame. Step 4 in this process transforms station locations from the geocentric celestial frame to the SSB frame. This step incorporates special-relativistic effects to all orders of the velocity ratio v/c . From a general relativistic point of view, this transformation is a special relativistic transformation between proper coordinates of two local frames (geocentric and SSB) in relative motion. For both frames, the underlying gravitational potential can be taken approximately as the sum of locally constant potentials caused by all masses in the Solar System. The complications caused by small local variations in the Earth's potential are discussed below. The initial proper delay is then computed (step 5) in the SSB frame on the basis of these SSB station locations and an *a priori* SSB source location. A small proper-delay correction is then applied to account for the differential gravitational retardation introduced along the two ray paths through the Solar System, including retardation by the Earth's gravity. A final Lorentz transformation (including all orders of v/c) then transforms the corrected SSB proper delay to a model for the observed delay in the celestial geocentric reference frame. Note that, rather than transforming between frames, some formulations account for special relativistic effects as an *ad hoc* term expanded to order $(v/c)^2$. While this may be convenient for calculating the delay, it obscures the important physical insights that are gained by a clear definition of the reference frame used for each step.

Since the Earth's gravitational potential U_E varies slightly through the Earth ($\Delta U_E/c^2 \approx 3.5 \times 10^{-10}$ from center to surface), the specification of proper distance for a baseline passing through the Earth is not as straightforward

with respect to the Earth’s potential as it is with respect to the essentially constant potentials of distant masses. To overcome this difficulty, VLBI-derived station locations are now customarily specified in terms of the “TDT (Terrestrial Dynamic Time) spatial coordinates” that are used in Earth-orbiter models. A proper length that corresponds to a modeled baseline can be obtained through appropriate integration of the local metric (Shahid-Saless *et al.*, 1991). Such proper lengths deviate slightly (≤ 3 mm) from baselines modeled on the basis of the TDT convention in the worst case (a full Earth diameter). In practice, such a conversion is not necessary if baseline measurements obtained by different investigators are reported and compared in terms of TDT spatial coordinates.

The model presented here has been compared (Treuhaft and Thomas, 1991) with the “1-picosecond” relativistic model for VLBI delays developed by Shahid-Saless *et al.* (1991). When reduced to the same form, these two models are identical at the picosecond level, term by term, with one exception. (Treuhaft and Thomas, 1991) show that a correction is needed to the Shahid-Saless *et al.* modeling of the atmospheric delay in the SSB frame. This correction changes the Shahid-Saless *et al.* result by as much as 10 picoseconds. Comparisons of this formulation with the Goddard Space Flight Center implementation of the “consensus” model (Eubanks, 1991; IERS, 1996b) show agreement to better than 1 ps, suggesting that the atmospheric delay problem has been solved in the consensus model. The remainder of this section provides the details for the first six steps of the general outline given above.

A. Wave front arrival time difference

The fundamental part of the geometric model is the calculation (step 5 above) of the time interval for the passage of a wave front from station 1 to station 2. This calculation is actually performed in a coordinate frame at rest relative to the center of mass of the Solar System. The SSB coordinate system is used because source positions, planetary orbits, and motions of interplanetary spacecraft are most naturally modeled in this frame. This part of the model is presented first to provide a context for the subsequent sections, all of which are heavily involved with the details of time definitions and coordinate transformations. We will use the same subscript and superscript notation which is used in Sec. III.E to refer to the station locations as seen by an observer at rest relative to the center of mass of the Solar System.

First, we calculate the proper time delay that would be observed if the wave front were planar. This calculation is next generalized to a curved wave front, and finally we take into account the incremental effects which result from the wave front propagating through the various gravitational potential wells in the Solar System.

1. Plane wave front

Consider the case of a plane wave moving in the direction $\hat{\mathbf{k}}$ with station 2 having a velocity β_2 as shown in Fig. 4. As mentioned above, distance and time are to be represented as proper coordinates in the SSB frame. The speed of light c is set equal to 1 in the following formulation. The proper time delay is the time it takes the wave front to move the distance l at speed c . This distance is the sum of the two solid lines perpendicular to the wave front in Fig. 4:

$$t_2 - t_1 = \hat{\mathbf{k}} \cdot [\mathbf{r}_2(t_1) - \mathbf{r}_1(t_1)] + \hat{\mathbf{k}} \cdot \beta_2 [t_2 - t_1] . \quad (3.1)$$

Note that station 2 has moved since t_1 : the second term represents the distance that station 2 moves before receiving the signal at t_2 . This leads to the following expression for the geometric delay:

$$t_2 - t_1 = \frac{\hat{\mathbf{k}} \cdot [\mathbf{r}_2(t_1) - \mathbf{r}_1(t_1)]}{1 - \hat{\mathbf{k}} \cdot \beta_2} . \quad (3.2)$$

The baseline vector in the SSB frame, $\mathbf{r}_2(t_1) - \mathbf{r}_1(t_1)$, is computed from proper station locations Lorentz transformed from the geocentric celestial frame, using Eq. (3.158) in Sec. III.E. The source unit vector in the direction of signal propagation (source to receiver)

$$\hat{\mathbf{k}} = \begin{pmatrix} -\cos \alpha \cos \delta \\ -\sin \alpha \cos \delta \\ -\sin \delta \end{pmatrix} \quad (3.3)$$

is calculated from the SSB frame angular source coordinates α (right ascension) and δ (declination).

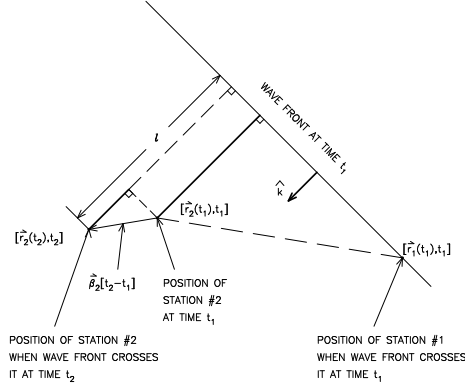


FIG. 4. Geometry for calculating the transit time of a plane wave front. Some refinements have been added to the schematic diagram of Fig. 1.

2. Curved wave front

In the case of a signal generated by a radio source within the Solar System it is necessary to include the effect of the curvature of the wave front. As depicted in Fig. 5, let a source irradiate two Earth-fixed stations whose positions are given by $\mathbf{r}_{1,2}(t)$ relative to the Earth's center. The position of the Earth's center in the SSB frame ($\mathbf{R}_c(t_1)$) as a function of signal reception time t_1 at station 1 is measured relative to the position of the emitter at the time of emission (t_e). While this calculation is actually done in the Solar System barycentric coordinate system, the development that follows is by no means restricted in applicability to that frame.

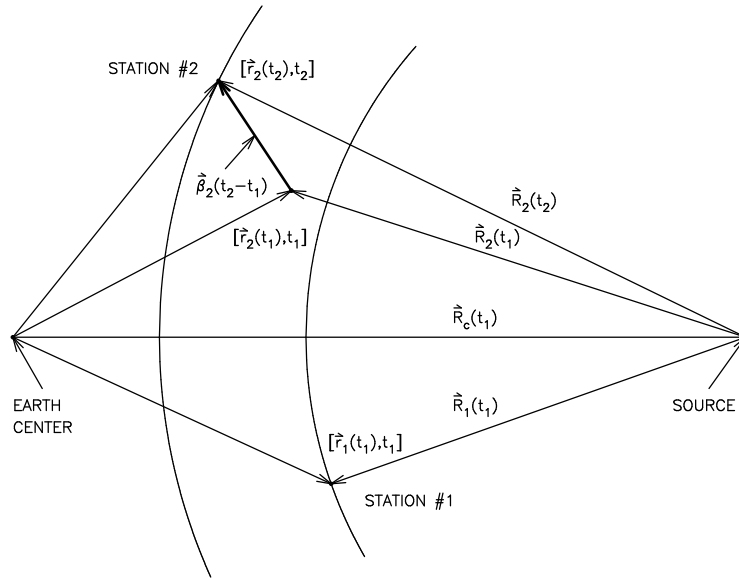


FIG. 5. Geometry for calculating the transit time of a curved wave front. It is only necessary to consider curvature effects for sources closer than ≈ 30 light years.

Suppose that a wave front emitted by the source at time t_e reaches station 1 at time t_1 and arrives at station 2 at time t_2 . The geometric delay in this frame will be given by

$$\tau = t_2 - t_1 = |\mathbf{R}_2(t_2)| - |\mathbf{R}_1(t_1)| , \quad (3.4)$$

where all distances are again measured in units of light travel time. If we approximate the velocity of station 2 by

$$\boldsymbol{\beta}_2 = \frac{\mathbf{R}_2(t_2) - \mathbf{R}_2(t_1)}{t_2 - t_1} \quad (3.5)$$

and use the relation ($i=1,2$)

$$\mathbf{R}_i(t_1) = \mathbf{R}_c(t_1) + \mathbf{r}_i(t_1) \quad (3.6)$$

we obtain:

$$\begin{aligned} \tau &= |\mathbf{R}_c(t_1) + \mathbf{r}_2(t_1) + \boldsymbol{\beta}_2\tau| - |\mathbf{R}_c(t_1) + \mathbf{r}_1(t_1)| \\ &= R_c(t_1) [|\widehat{\mathbf{R}}_c + \boldsymbol{\varepsilon}_2| - |\widehat{\mathbf{R}}_c + \boldsymbol{\varepsilon}_1|] , \end{aligned} \quad (3.7)$$

where

$$\begin{aligned} \boldsymbol{\varepsilon}_1 &= \mathbf{r}_1(t_1)/R_c(t_1) \\ \boldsymbol{\varepsilon}_2 &= [\mathbf{r}_2(t_1) + \boldsymbol{\beta}_2\tau]/R_c(t_1) . \end{aligned} \quad (3.8)$$

For $\boldsymbol{\varepsilon}_1$ and $\boldsymbol{\varepsilon}_2 \leq 10^{-4}$, only terms of order ε^3 need to be retained in expanding the expression for τ in Eq. (3.7) for computational purposes on machines that employ 15-16 decimal digit representations. This gives:

$$\tau = \frac{\widehat{\mathbf{R}}_c \cdot [\mathbf{r}_2(t_1) - \mathbf{r}_1(t_1)]}{[1 - \widehat{\mathbf{R}}_c \cdot \boldsymbol{\beta}_2]} + \frac{R_c \Delta_c(\tau)}{2 [1 - \widehat{\mathbf{R}}_c \cdot \boldsymbol{\beta}_2]} , \quad (3.9)$$

where to order ε^3

$$\Delta_c(\tau) = [\varepsilon_2^2 - \varepsilon_1^2] - [(\widehat{\mathbf{R}}_c \cdot \boldsymbol{\varepsilon}_2)^2 + (\widehat{\mathbf{R}}_c \cdot \boldsymbol{\varepsilon}_1)^2 + (\widehat{\mathbf{R}}_c \cdot \boldsymbol{\varepsilon}_2)^3 - (\widehat{\mathbf{R}}_c \cdot \boldsymbol{\varepsilon}_2)\varepsilon_2^2 - (\widehat{\mathbf{R}}_c \cdot \boldsymbol{\varepsilon}_1)^3 + (\widehat{\mathbf{R}}_c \cdot \boldsymbol{\varepsilon}_1)\varepsilon_1^2] . \quad (3.10)$$

The first term in Eq. (3.9) is just the plane wave approximation, *i.e.*, as $R_c \rightarrow \infty$, $\widehat{\mathbf{R}}_c \rightarrow \widehat{\mathbf{k}}$, with the second term in brackets in Eq. (3.10) approaching zero as r^2/R_c . Given that the ratio of the first term to the second term is $\approx r/R_c$, wave front curvature is not calculable using sixteen-decimal-digit arithmetic if $R > 10^{16}r$. For Earth-fixed baselines that are as long as an Earth diameter, requiring that the effects of curvature be less than 1 ps ≈ 0.3 mm implies that the above formulation (Eq. 3.10) must be used for $R < 3 \times 10^{14}$ km, or approximately 30 light years. At the same accuracy level, fourth and higher order terms in ε become important for $R < 2 \times 10^5$ km, or approximately inside the Moon's orbit. Fukushima (1994) has presented a formulation which should be applicable for Earth-based VLBI with radio sources as close as the Moon.

The procedure for the solution of Eq. (3.9) is iterative for $\varepsilon < 10^{-4}$, using the following:

$$\tau_n = \tau_0 + \frac{R_c \Delta_c(\tau_{n-1})}{2[1 - \widehat{\mathbf{R}}_c \cdot \boldsymbol{\beta}_2]} , \quad (3.11)$$

where

$$\tau_0 = \tau_{\text{plane wave}} . \quad (3.12)$$

For $\varepsilon > 10^{-4}$, directly iterate on Eq. (3.7) itself, using the procedure:

$$\tau_n = R_c [|\widehat{\mathbf{R}}_c + \boldsymbol{\varepsilon}_2(\tau_{n-1})| - R_c |\widehat{\mathbf{R}}_c + \boldsymbol{\varepsilon}_1|] , \quad (3.13)$$

where again τ_0 is the plane wave approximation.

3. Gravitational delay

As predicted by Einstein’s theory of general relativity (Einstein, 1911, 1916), an electromagnetic signal propagating in a gravitational potential is retarded relative to its travel time in field-free space. Shapiro (1964; 1967) pointed out that this produces both a deviation from a straight-line path and a time delay. For VLBI this implies that the computed differential arrival time value of the signals at $\mathbf{r}_1(t_1)$ and $\mathbf{r}_2(t_2)$ must be corrected for gravitational effects. For Earth-based experiments the dominant contribution comes from the Sun. Gravitational potential effects and curved wave front effects can be calculated independently of each other since the former are a small perturbation (≈ 8.5 microradians or $\leq 1''.75$), even for Sun-grazing rays.

Our formulation of the relativistic light travel time is based on Moyer’s (1971) implementation of the work of Tausner (1966) and Holdridge (1967). For the (exaggerated) geometry illustrated in Fig. 6, the required correction to *coordinate* time delay due to the p th gravitating body is

$$\Delta_{Gp} = \frac{(1 + \gamma_{\text{PPN}})\mu_p}{c^3} \left[\ln \left(\frac{r_s + r_2(t_2) + r_{s2}}{r_s + r_2(t_2) - r_{s2}} \right) - \ln \left(\frac{r_s + r_1(t_1) + r_{s1}}{r_s + r_1(t_1) - r_{s1}} \right) \right], \quad (3.14)$$

where r_{si} ($i = 1, 2$) is the separation of station i from source s :

$$r_{si} = |\mathbf{r}_i(t_i) - \mathbf{r}_s(t_e)|. \quad (3.15)$$

The gravitational constant μ_p is

$$\mu_p = Gm_p, \quad (3.16)$$

where G is the universal gravitational constant, and m_p is the mass of body p . A higher-order term ($\propto \mu_p^2/c^5$) contributes to Δ_{Gp} only for observations extremely close to the Sun’s limb (IERS, 1992). Here γ_{PPN} is the γ factor in the parametrized post-Newtonian gravitational theory (*e.g.* Misner *et al.*, 1973). In general relativity $\gamma_{\text{PPN}} = 1$, but it can be allowed to be an estimated parameter to permit experimental tests of general relativity, as originally proposed by Shapiro (1964). A dramatic demonstration of the importance of general relativity in estimating the delay can be made by “turning off” this added delay by setting $\gamma_{\text{PPN}} = -1$ in the model. This can increase the discrepancy between theoretical and observed delays by an order of magnitude because the Sun’s gravity induces a bending of 20 nrad (4 milliarcseconds) even for ray paths 90° removed from its position relative to the Earth.

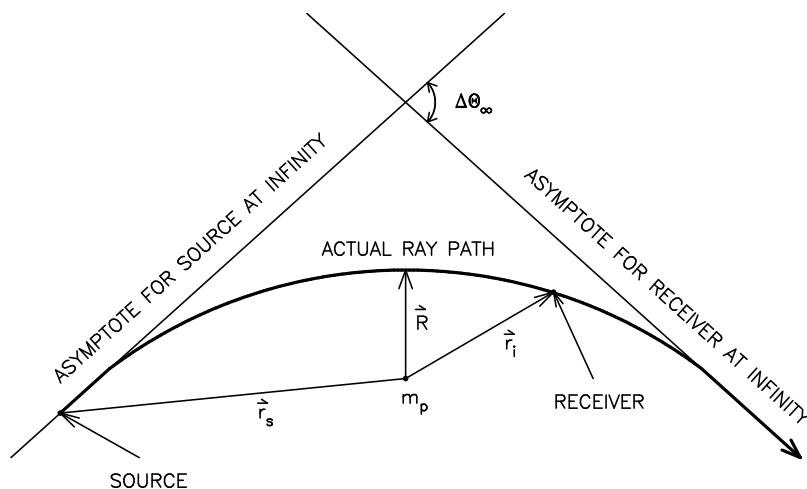


FIG. 6. Schematic representation of the geodesic connecting the source and receiver in the presence of a gravitational mass.

Depending on the particular source-receiver geometry in a VLBI experiment, a number of useful approximations are possible for the correction Δ_{Gp} of Eq. (3.14). Dropping the time arguments in Eq. (3.14), we have:

$$\Delta_{Gp} = \frac{(1 + \gamma_{\text{PPN}})\mu_p}{c^3} \ln \left[\left(\frac{r_s + r_2 + r_{s2}}{r_s + r_1 + r_{s1}} \right) \left(\frac{r_s + r_1 - r_{s1}}{r_s + r_2 - r_{s2}} \right) \right]. \quad (3.17)$$

This formulation is appropriate for the most general geometry, in which $r_s \approx r_i \approx r_{si}$. For the practical case of Earth-based VLBI with distant sources and closely spaced VLBI receivers, however, $|\mathbf{r}_2 - \mathbf{r}_1|/r_1 \rightarrow 0, r_i/r_s \rightarrow 0$. The gravitational time delay Δ_{Gp} may then be expanded in terms of $r_i/r_s, r_{si}/r_s$. Making use of the relationship

$$r_{si} = [\mathbf{r}_s^2 - 2\mathbf{r}_s \cdot \mathbf{r}_i + \mathbf{r}_i^2]^{1/2} \approx r_s - \mathbf{r}_i \cdot \hat{\mathbf{r}}_s \quad (3.18)$$

leads to

$$\Delta_{Gp} = \frac{(1 + \gamma_{\text{PPN}})\mu_p}{c^3} \ln \left(\frac{r_1 + \mathbf{r}_1 \cdot \hat{\mathbf{r}}_s}{r_2 + \mathbf{r}_2 \cdot \hat{\mathbf{r}}_s} \right) \quad (3.19)$$

for $r_i/r_s \rightarrow 0$. If we define $\mathbf{r}_2 = \mathbf{r}_1 + \Delta\mathbf{r}$, and require that $|\Delta\mathbf{r}|/r_1 \rightarrow 0$ (short baselines) then

$$r_2(1 + \hat{\mathbf{r}}_2 \cdot \hat{\mathbf{r}}_s) \approx r_1(1 + \hat{\mathbf{r}}_1 \cdot \hat{\mathbf{r}}_s) + \Delta\mathbf{r} \cdot (\hat{\mathbf{r}}_1 + \hat{\mathbf{r}}_s). \quad (3.20)$$

Substituting into Eq. (3.19) and expanding the logarithm, we obtain:

$$\Delta_{Gp} = \frac{-(1 + \gamma_{\text{PPN}})\mu_p}{c^3} \frac{(\mathbf{r}_2 - \mathbf{r}_1) \cdot (\hat{\mathbf{r}}_1 + \hat{\mathbf{r}}_s)}{r_1(1 + \hat{\mathbf{r}}_1 \cdot \hat{\mathbf{r}}_s)}. \quad (3.21)$$

These three formulations of Eqs. (3.17, 3.19 or 3.21) are computationally appropriate for different situations. For Earth-based VLBI observations, the correction Δ_{Gp} is calculated for each of the major bodies in the Solar System (Sun, planets, Earth, and Moon). The immense central mass of the Galaxy (on the order of 10^{11} solar masses) contributes an additional delay. Assuming a mass concentration of 2/3 in the nucleus and the current estimate of our distance from the center of 8.5 kpc (Binney and Tremaine, 1987), it can be estimated that the gravitational influence of the Galactic center on electromagnetic signals exceeds that of the Sun by a factor of ≈ 40 . Geometrically, this causes a bending of 4 arc seconds when ray paths approach within $\approx 10^\circ$ of the center (for the closest routinely observed radio source). However, because of the very slow rotation of the Solar System about the Galactic center (240 million years), the time variation of this bending is extremely small. Therefore, for practical purposes, Galactic bending merely produces a quasi-static distortion of the sky, and can be absorbed into the source coordinates which form the basis of our model of the celestial sphere.

Before the correction Δ_{Gp} can be applied to a proper delay computed according to Eq. (3.2), it must be converted from a coordinate-delay correction to a proper-delay correction appropriate to a near-Earth frame. For such proper delays, the gravitational correction is given (*e.g.* Hellings, 1986) to good approximation by

$$\Delta'_{Gp} = \Delta_{Gp} - (1 + \gamma_{\text{PPN}})U\tau, \quad (3.22)$$

where τ is the proper delay given by Eq. (3.2), and where $U = \mu_p/r_p c^2$ is the negative of the gravitational potential of the given mass divided by c^2 , as observed in the vicinity of the Earth (U is a positive quantity). The $U\tau$ term is a consequence of the relationship of coordinate time to proper time, and the $\gamma_{\text{PPN}}U\tau$ term is a consequence of the relationship of coordinate distance to proper distance.

The total gravitational correction used is

$$\Delta'_G = \sum_{p=1}^N \Delta'_{Gp}, \quad (3.23)$$

where the summation over p is for the N major bodies in the Solar System. For the Earth, the $(1 + \gamma_{\text{PPN}})U\tau$ term in Eq. (3.22) is omitted if one wishes to work in the ‘‘TDT spatial coordinates’’ that are used in reduction of Earth-orbiter data. The scale factor $(1 + \gamma_{\text{PPN}})U$ is approximately 19.7×10^{-9} for the Sun. A number of other conventions are possible. One of these, which includes the $(1 + \gamma_{\text{PPN}})U\tau$ term for the Earth evaluated at the Earth’s surface, yields an additional scale factor of 1.4×10^{-9} . In either case, the model delay is decreased relative to the proper delay. Consequently, all inferred ‘‘measured’’ lengths increase by the same fraction relative to proper lengths (*i.e.*, by 19.7 parts per billion and 21.1 ppb in the two cases).

Some care must be taken in defining the positions given by \mathbf{r}_s , $\mathbf{r}_2(t_2)$, and $\mathbf{r}_1(t_1)$. We have chosen the origin to be the position of the gravitational mass at the time of closest approach of the received signal to that object. The position \mathbf{r}_s of the source relative to this origin is the position of that source at the time t_e of the emission of the received signal. Likewise, the position $\mathbf{r}_i(t_i)$ of the i th receiver is its position in this coordinate system at the time of reception of the signal. Even with this care in the definition of the relative positions, we are making an approximation, and implicitly assuming that such an approximation is no worse than the approximations used by Moyer (1971) to obtain Eq. (3.14).

Some considerations follow, concerning the use of appropriate times to obtain the positions of the emitter, the gravitational object, and the receivers. For a grazing ray emitted by a source at infinity, using the position of the p th gravitating body at the time of reception of the signal at station 1 (t_r) rather than at the time of closest approach of the signal to m_p (t_a) can cause a substantial error on baselines with dimensions of the Earth, as shown by the following calculation. From Fig. 7, the distance of closest approach R changes during the light transit time t_{tr} of a signal from a gravitational object at a distance R_{EG} by

$$\Delta R \approx R_{EG} \dot{\alpha} t_{tr} = \dot{\alpha} R_{EG}^2 / c, \quad (3.24)$$

where $\dot{\alpha}$ is the time rate of change of the angular position of the deflecting body as observed from Earth. Since the deflection is

$$\Theta \approx 2 \frac{(1 + \gamma_{PPN}) \mu_p}{c^3} \left(\frac{c}{R} \right) \quad (3.25)$$

it changes by an amount

$$\Delta \Theta = -\Theta \left(\frac{\Delta R}{R} \right) = -\Theta \left(\frac{\dot{\alpha} R_{EG}^2}{cR} \right) \quad (3.26)$$

during the light transit time.

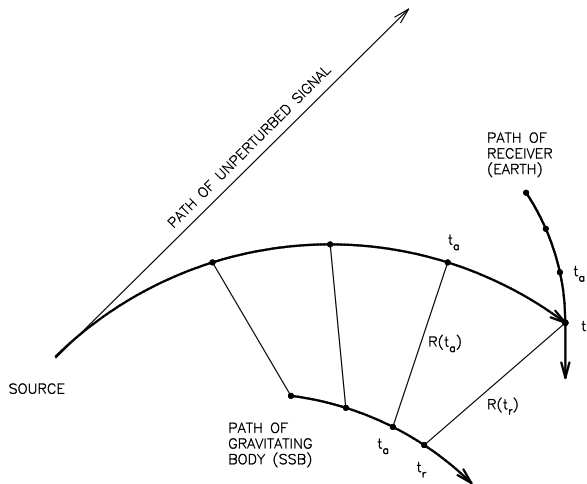


FIG. 7. Schematic representation of the motion of a gravitating object (Sun) during the transit time of a signal from the point of closest approach to reception by an antenna on Earth. Both move between the time t_a at closest approach $R(t_a)$ and the time t_r at reception. This motion needs to be taken into account for the highest accuracy.

We consider the two bodies of largest mass in the Solar System: the Sun and Jupiter. For rays that just graze the surfaces, their respective deflections $\Delta \Theta$ are 8470 and 79 nanoradians. From Solar System ephemerides, the barycentric angular velocities $\dot{\alpha}$ are estimated to be ≈ 0.05 and 17 nrad/s for the Sun and Jupiter. (The Sun's motion in the barycentric frame has approximately the orbital period of Jupiter, ≈ 12 years, with a radius on the order of the Sun's radius). Using approximate radii and distances from Earth to estimate R_{EG} and Θ , Eq. (3.26) gives 30 nrad for Jupiter; the corresponding value for the Sun is only 0.05 nrad. For a baseline whose length equals the radius of

the Earth, $\delta(\Delta\Theta)R_E$ is thus approximately 200 and 0.3 mm for Jupiter and the Sun, respectively. The effect is much smaller for the Sun in spite of its much larger mass, due to its extremely slow motion in the barycentric frame.

In view of the very rapid decrease of gravitational deflection with increasing distance of closest approach, it is extremely improbable that a random VLBI observation will involve rays passing close enough to a gravitating body for this correction to be of importance. Exceptions are experiments that are specifically designed to measure planetary gravitational delay (*e.g.* Treuhaft and Lowe, 1991). In order to guard against such an unlikely situation in routine work, and to provide analysis capability for special experiments, it is prudent to perform the transit-time correction for all planets for all observations. To obtain the positions of the gravitational objects, we employ an iterative procedure, using the positions and velocities of the objects at signal reception time. If $\mathbf{R}(t_r)$ is the position of the gravitational object at signal reception time t_r , then that object's position $\mathbf{R}(t_a)$ at the time t_a of closest approach of the ray path to the object \mathbf{R}_a was

$$\mathbf{R}(t_a) = \mathbf{R}(t_r) - (t_r - t_a)\bar{\mathbf{V}}, \quad (3.27)$$

$$t_r - t_a = |\mathbf{R}_c|/c. \quad (3.28)$$

This correction is done iteratively, using the velocity $\mathbf{V}(t_r)$ as an approximation of the mean velocity $\bar{\mathbf{V}}$. Because $v/c \approx 10^{-4}$, the iterative solution,

$$\mathbf{R}_n(t_a) = \mathbf{R}(t_r) - |\mathbf{R}_{n-1}(t_a)| \mathbf{V}(t_r)/c \quad (3.29)$$

rapidly converges to the required accuracy.

B. Time information

Before continuing with the description of the geometric model, some definitions must be introduced concerning time-tag information in the experiments, and the time units which will appear as arguments below. A general reference for time definitions is the *Explanatory Supplement* (Seidelmann *et al.*, 1992). The data epoch for VLBI observables is taken from the UTC (Coordinated Universal Time) time tags in the data stream at station 1, UTC_1 . This time is converted to Terrestrial Dynamic Time TDT, with the conversion consisting of the following components:

$$\begin{aligned} \text{TDT} = & (\text{TDT} - \text{TAI}) + (\text{TAI} - \text{UTC}_{\text{IERS}}) + (\text{UTC}_{\text{IERS}} - \text{UTC}_{\text{STD}}) \\ & + (\text{UTC}_{\text{STD}} - \text{UTC}_1) + \text{UTC}_1. \end{aligned} \quad (3.30)$$

The four offsets in Eq. (3.30) thus serve to convert the station 1 time tags to TDT. Their meanings are as follows:

1. $\text{TDT} - \text{TAI}$ is 32.184 seconds by definition; TAI (Temps Atomique International) is atomic time.
2. $\text{TAI} - \text{UTC}_{\text{IERS}}$ is the offset between atomic and coordinated time. It is a published integer second offset (accumulated leap seconds) for any epoch after 1 January, 1972. Prior to that time, it is a more complicated function, which will not be discussed here since normally no observations previous to the mid-1970s are modeled. The International Earth Rotation Service (IERS), its predecessor, Bureau International de l'Heure (BIH), and Bureau International des Poids et Mesures (BIPM) are the coordinating bodies responsible for upkeep and publication of standard time and Earth rotation quantities.
3. $\text{UTC}_{\text{IERS}} - \text{UTC}_{\text{STD}}$ is the offset in UTC between the coordinated time scales maintained by the IERS (BIPM) and secondary standards maintained by numerous national organizations. For VLBI stations in the U. S. these secondary standards are those of the National Institute of Standards and Technology in Boulder, Colorado, and the U. S. Naval Observatory in Washington, DC. These offsets can be obtained from BIPM Circular T (*e.g.* BIPM, 1997).
4. $\text{UTC}_{\text{STD}} - \text{UTC}_1$ is the (often unknown) offset between UTC kept by station 1 and the secondary national standard. This may be as large as several microseconds, and is not precisely known for all experiments. It can be a source of modeling error: an error Δt in epoch time causes an error of $\approx B\omega_E\Delta t = 7.3 \times 10^{-5}$ mm per km of baseline B per μs of clock error Δt , where ω_E is the rotation rate of the Earth. Even in the extreme case of a 10,000 km baseline, however, this amounts to only 0.7 mm per μs , while present-day clock synchronization is usually at least an order of magnitude better, at the 0.1- μs level.

Coordinated Universal Time and TDT are not convenient for modeling Earth orientation. This is normally done in terms of UT1, a quantity that is proportional to the angle of rotation of the Earth. The *a priori* offset UT1–UTC and the position of the Earth’s rotation pole can be obtained by interpolation of the IERS Bulletin A smoothed values. However, any other source of UT1–UTC and pole position could be used provided it is expressed in a left-handed coordinate system (see Sec. III.D.1). Part of the documentation for any particular set of results needs to include a clear statement of what values of UT1–UTC and pole position were used in the data reduction process.

For the Earth model based on the IAU conventions, the following definitions are employed throughout (Kaplan, 1981):

1. Julian date at epoch J2000.0 = 2451545.0.
2. All time arguments denoted by T below are measured in Julian centuries of 36525 days of the appropriate time relative to the epoch J2000.0, *i.e.*, $T = (JD - 2451545.0)/36525$.
3. For the time arguments used to obtain precession and nutation, or to refer to the Solar System ephemeris, Barycentric Dynamic Time (TDB, Temps Dynamique Barycentrique) is used. This is related to Terrestrial Dynamic Time (TDT, Temps Dynamique Terrestre) by the following approximation:

$$\text{TDB} = \text{TDT} + 0.^s001658 \sin(g + 0.0167 \sin(g)) , \quad (3.31)$$

where

$$g = 2\pi(357.^{\circ}528 + 35999.^{\circ}050 T)/360^{\circ} \quad (3.32)$$

is the mean anomaly of the Earth in its orbit.

For present analyses of Earth-based VLBI observations, Eq. (3.31) is adequate. Moyer (1981) gave a more accurate relation between TDB and TDT by accounting for the dominant gravitational effects of the major planets. Hirayama *et al.* (1987) and Fairhead and Bretagnon (1990) have extended this work to the nanosecond level. In the future, TDT and TDB will be replaced by two new time scales, TCG and TCB, geocentric and barycentric coordinate time (Fukushima *et al.*, 1986). These will eliminate the need to rescale spatial coordinates that was discussed in Sec. III.A.3.

C. Station locations

Coordinates of the observing stations are expressed in the Conventional International Origin (CIO 1903) reference system, with the reference point for each antenna defined as in Sec. III.G. The present accuracy level of space geodesy makes it imperative to account for various types of crustal motions. Among these deformations are tectonic motions, solid Earth tides, ocean effects, and alterations of the Earth’s surface due to local geological, hydrological, and atmospheric processes. Mismodeled effects will manifest themselves as temporal changes of the Earth-fixed baseline. It is therefore important to model all crustal motions as completely as possible. The current level of mismodeling of these motions is probably one of the leading sources of systematic error (along with the troposphere) in analyses of VLBI data.

Evaluation of the time dependence of station locations is most simply done by estimating a new set of coordinates in the least-squares process for each VLBI observing session (*e.g.*, Fig. 19 in Sec. VI.B). Subsequent fits to these results can then produce estimates of the linear time rate of change of the station location. For rigorous interpretation of the statistical significance of the results, correlations of coordinates estimated at different epochs must be fully taken into account when calculating uncertainties of the rates. The advantage of this approach is that the contribution of each session to the overall time rate may be independently evaluated, since it is clearly isolated. Any nonlinear (*e.g.*, seasonal) variations are easily detected. Also, no tectonic model information is imposed on the solution. An alternative approach is to model long-period tectonic motion directly, by introducing time rates of change of the station coordinates as parameters. The model is linear, with the position of station i at time t , $\mathbf{r}_i = (x_i, y_i, z_i)$, expressed in terms of its velocity $\dot{\mathbf{r}}_i$ as

$$\mathbf{r}_i = \mathbf{r}_i^0 + \dot{\mathbf{r}}_i(t - t_0) . \quad (3.33)$$

Here t_0 is a reference epoch, at which the station position is $\mathbf{r}_i^0 = (x_i^0, y_i^0, z_i^0)$.

1. Tectonic plate motion

As alternatives to estimating linear time dependence of the station coordinates from VLBI experiments, several standard models of tectonic plate motion are available. They all describe the motion as a rotation of a given rigid plate (spherical cap) about its rotation pole on the surface of a spherical Earth. Time dependence of the Cartesian station coordinates of station i which resides on plate j is expressed as

$$\mathbf{r}_i = \mathbf{r}_i^0 + (\boldsymbol{\omega}^j \times \mathbf{r}_i^0)(t - t_0), \quad (3.34)$$

where $\boldsymbol{\omega}^j = (\omega_x^j, \omega_y^j, \omega_z^j)$ is the angular velocity vector of the plate.

These tectonic motion models are based on paleomagnetic data spanning millions of years, but they also provide an excellent quantitative characterization of present-day plate motions. This attests to the smooth character of tectonic motion over immense time scales. Although the possibility of slow relative motions of the Earth's land masses was first suggested by Wegener before World War I (Wegener, 1912) mantle convection was identified as the driving mechanism only much later, and the reality of this phenomenon was not generally accepted until the 1960s (Menard, 1986). The first quantitative global tectonic motion model is due to Minster and Jordan (1978), and was also the first to be used in VLBI analyses. It is denoted AM0-2 in the original paper. More recent models, denoted Nuvel-1 and NNR-Nuvel-1, are due to DeMets *et al.* (1990) and Argus and Gordon (1991), respectively. In Nuvel-1, the Pacific plate is stationary,

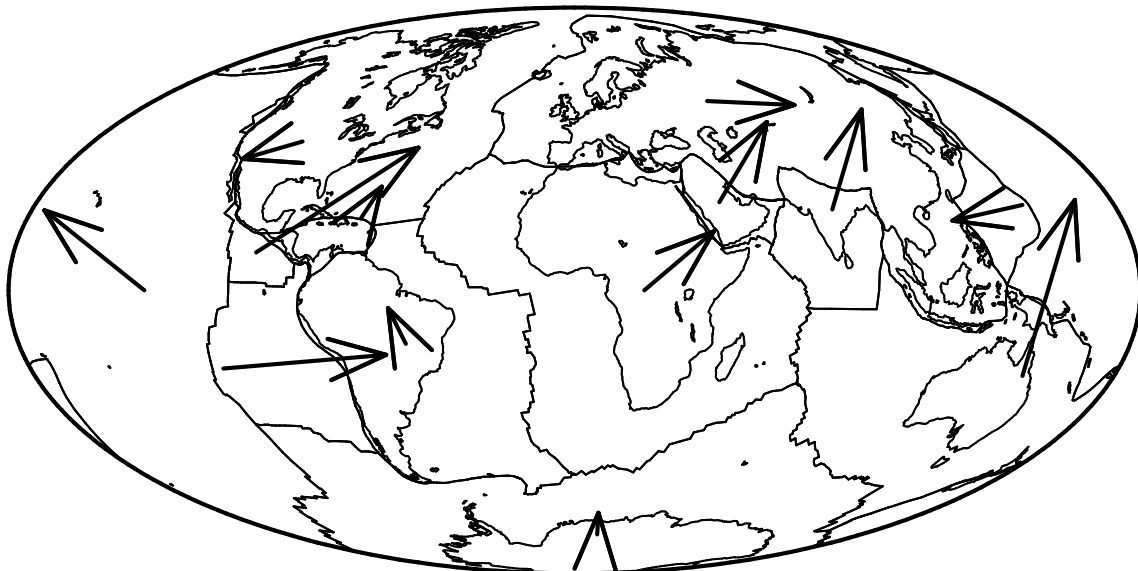


FIG. 8. Schematic directions and magnitudes of the motions of the major tectonic plates in the NNR-Nuvel-1A model. The longest arrows represent motions of approximately 10 cm/yr.

while NNR-Nuvel-1 is based on the imposition of a no-net-rotation (NNR) condition. Inadequate knowledge of the internal mechanics of the Earth makes uncertain any absolute determination of plate rotation relative to the deep interior. Hence the NNR condition is customarily imposed: $\mathbf{v} \times \mathbf{r}$ integrated over the Earth's surface is constrained to be zero, where \mathbf{v} is the velocity at point \mathbf{r} on one of the rigidly rotating tectonic plates. With some notable exceptions, the Nuvel-1 models give rates that are very close to those of the AM0-2 model. The AM0-2 India plate has been split into two: Australia and India, and there are four additional plates: Juan de Fuca, Philippine, Rivera and Scotia. A recent revision of the paleomagnetic time scale has led to a rescaling of the Nuvel-1 rates. These "Nuvel-1A" and "NNR-Nuvel-1A" model rates are equal to the Nuvel-1 and NNR-Nuvel-1 rates, respectively, multiplied by a factor of 0.9562 (DeMets *et al.*, 1994). Table II shows the angular velocities of the 16 tectonic plates in the NNR-Nuvel-1A model. Thirteen major plate motions are also shown in Fig. 8, with the velocities depicted approximately to scale. The largest arrows represent motions of ≈ 10 cm/yr. A more detailed example of the effect of tectonic motion on relative station locations is given in Fig. 19 of Sec. VI.B, which shows the convergence of the North American and Pacific plates.

2. Tidal station motion

The Earth is not perfectly rigid, and its crust deforms in response to the gravitational attraction of other massive bodies. The most important of these are the Sun and Moon, whose periodic orbits induce time-varying displacements of the Earth's crust. Such motions, with periodicities ranging from hours to years, are called tidal effects. Tides produce station displacements that can be far larger than those caused by tectonic motions in a year, necessitating their inclusion in models of VLBI observables. The tidal displacements can be classified into several categories, of which contemporary VLBI models normally include four. In the standard terrestrial coordinate system, these tidal effects modify the station location \mathbf{r}_0 by an amount

$$\Delta = \Delta_{\text{sol}} + \Delta_{\text{pol}} + \Delta_{\text{ocn}} + \Delta_{\text{atm}} , \quad (3.35)$$

where the four terms are due to solid Earth tides (the direct primary effect), pole tide, ocean loading, and atmosphere loading (secondary effects), respectively. Other Earth-fixed effects (*e.g.*, glacial loading) can be incorporated by extending the definition of Δ to include additional terms. All four tidal effects are most easily calculated in some variant of a VEN (Vertical, East, North) local geodetic coordinate system. Application of the transformation \mathbf{VW} (given in the next section, Eqs. 3.61) transforms them to the geocentric Earth-fixed coordinate frame.

a. Solid Earth tides

Calculating the shifts of the positions of the observing stations caused by solid Earth tides is rather complicated due to the solid tides' coupling with the ocean tides, and the effects of local geology. Some of these complications are addressed below (*e.g.*, ocean loading). An isolated simple model of Earth tides is the multipole response model developed by Williams (1970b), who used Melchior (1966) as a reference. Let \mathbf{R}_p be the position of a tide-producing body, and \mathbf{r}_0 the station position. To allow for a phase shift ψ of the tidal effects from a nominal value of 0, the phase-shifted station vector \mathbf{r}_s is calculated from \mathbf{r}_0 by applying a matrix \mathbf{L} , describing a right-handed rotation through an angle ψ about the Z axis of date, $\mathbf{r}_s = \mathbf{L}\mathbf{r}_0$. This lag matrix \mathbf{L} is

$$\mathbf{L} = \begin{pmatrix} \cos \psi & \sin \psi & 0 \\ -\sin \psi & \cos \psi & 0 \\ 0 & 0 & 1 \end{pmatrix} . \quad (3.36)$$

A positive value of ψ implies that the peak response on an Earth meridian occurs at a time $\delta t = \psi/\omega_E$ after that meridian plane containing \mathbf{r}_0 crosses the tide-producing object, where ω_E is the angular rotation rate of the Earth (Eq. 3.163). No significant departures from a zero phase shift have yet been detected: the peak response occurs when the meridian plane containing \mathbf{r}_s also includes \mathbf{R}_p . Some theoretical models predict out-of-phase components due to anelasticity.

The tidal potential at \mathbf{r}_s due to the perturbing body at \mathbf{R}_p may be expressed as a multipole expansion

$$\begin{aligned} U_{\text{tidal}} &= \frac{Gm_p}{R_p} \left[\left(\frac{r_s}{R_p} \right)^2 P_2(\cos \theta) + \left(\frac{r_s}{R_p} \right)^3 P_3(\cos \theta) \right] \\ &= U_2 + U_3 , \end{aligned} \quad (3.37)$$

where only the quadrupole and octupole terms have been retained. Here, G is the gravitational constant, m_p is the mass of the perturbing body, P_2 and P_3 are Legendre polynomials, and θ is the angle between \mathbf{r}_s and \mathbf{R}_p . While the quadrupole displacements are on the order of 500 mm, the mass and distance ratios of the Earth, Moon, and Sun limit the octupole terms to a few mm. An estimate of the retardation correction (employing the position of the tide-producing mass at a time earlier than that of the observation by an amount equal to the light-travel time) shows that this correction is well below 1 mm, and can therefore be neglected. We calculate tidal effects in the terrestrial CIO 1903 frame. While r_s is given in this frame, R_p is typically taken from the planetary ephemeris which is defined in the SSB frame. The Lorentz transform from the SSB to the geocentric celestial frame given the Earth's orbital velocity of $10^{-4}c$ may be neglected because the maximum solid tide is 500 mm ($\times 10^{-4} = 0.05$ mm). However, the rotation between the celestial frame and the terrestrial frame is large and must be accounted for:

$$\mathbf{R}_{p_t} = \mathbf{Q}^{-1}\mathbf{R}_{p_c} , \quad (3.38)$$

where \mathbf{Q} is the rotational transformation between frames defined by Eq. (3.76). The subscripts t and c on \mathbf{R}_p indicate when the vector is expressed in the terrestrial or celestial frame, respectively. The perturber unit vector $\hat{\mathbf{R}}_p$ has the form of the signal propagation vector from the radio source (Eq. 3.3), with the right ascension and declination of the perturbing body (α_p, δ_p) replacing the source coordinates (α, δ) and the vector direction reversed:

$$\hat{\mathbf{R}}_p = \mathbf{Q}^{-1} \begin{pmatrix} \cos \delta_p \sin \alpha_p \\ \cos \delta_p \cos \alpha_p \\ \sin \delta_p \end{pmatrix}. \quad (3.39)$$

The station unit vector takes a similar form in terms of the longitude and geocentric latitude:

$$\hat{\mathbf{r}}_s = \begin{pmatrix} \cos \phi_s \sin \lambda_s \\ \cos \phi_s \cos \lambda_s \\ \sin \phi_s \end{pmatrix}. \quad (3.40)$$

After the SSB coordinates of the perturbing body are rotated into the terrestrial frame of the station, the scalar product of the unit vectors yields the angle needed to calculate the Legendre polynomials in Eq. (3.37), $\cos \theta = \hat{\mathbf{r}}_s \cdot \hat{\mathbf{R}}_p$.

Once the tidal potential is obtained, the next step is to determine the displacement experienced by a station located at r_s . In a local geodetic VEN coordinate system on an elliptical Earth, the solid tidal displacement vector $\boldsymbol{\delta}_{\text{sol}}$ is

$$\boldsymbol{\delta}_{\text{sol}} = \sum_i [\delta_1^{(i)}, \delta_2^{(i)}, \delta_3^{(i)}]^T, \quad (3.41)$$

where the $\delta_j^{(i)}$ ($i = 2, 3$) are the quadrupole and octupole displacements. The components of $\boldsymbol{\delta}_{\text{sol}}$ are obtained from the tidal potential as

$$\delta_1^{(i)} = h_i U_i / g \quad (3.42)$$

$$\delta_2^{(i)} = l_i \cos \phi_s \left(\frac{\partial U_i}{\partial \lambda_s} \right) / g \quad (3.43)$$

$$\delta_3^{(i)} = l_i \left(\frac{\partial U_i}{\partial \phi_s} \right) / g, \quad (3.44)$$

where h_i ($i = 2, 3$) are the radial (quadrupole and octupole) Love numbers, l_i ($i = 2, 3$) the corresponding tangential Love numbers, and λ_s and ϕ_s are the station longitude and geocentric latitude, and g the surface acceleration due to gravity,

$$g = Gm_E / r_s^2. \quad (3.45)$$

Values of the various Love numbers range from 0 to 1, since the Earth is neither perfectly rigid nor perfectly elastic. For the highest accuracy, distinction must be made between displacements in the radial *vs.* vertical, and tangential *vs.* horizontal directions, which differ to the extent of the Earth's flattening (about 1 part in 300).

Reverting to Cartesian coordinates, some algebra then produces the following expressions for the quadrupole and octupole components of $\boldsymbol{\delta}_{\text{sol}}$ in terms of the coordinates of the station (x_s, y_s, z_s) and the tide-producing bodies (X_p, Y_p, Z_p) :

$$\delta_1^{(2)} = (h_2/g) \sum_p \frac{3\mu_p r_s^2}{R_p^5} \left[\frac{(\mathbf{r}_s \cdot \mathbf{R}_p)^2}{2} - \frac{r_s^2 R_p^2}{6} \right] \quad (3.46)$$

$$\delta_2^{(2)} = (l_2/g) \sum_p \frac{3\mu_p r_s^3}{R_p^5} (\mathbf{r}_s \cdot \mathbf{R}_p) (x_s Y_p - y_s X_p) / \sqrt{x_s^2 + y_s^2} \quad (3.47)$$

$$\delta_3^{(2)} = (l_2/g) \sum_p \frac{3\mu_p r_s^2}{R_p^5} (\mathbf{r}_s \cdot \mathbf{R}_p) \left[\sqrt{x_s^2 + y_s^2} Z_p - \frac{z_s}{\sqrt{x_s^2 + y_s^2}} (x_s X_p + y_s Y_p) \right] \quad (3.48)$$

$$\delta_1^{(3)} = (h_3/g) \sum_p \frac{\mu_p r_s^2}{2R_p^7} (\mathbf{r}_s \cdot \mathbf{R}_p) \left[5(\mathbf{r}_s \cdot \mathbf{R}_p)^2 - 3r_s^2 R_p^2 \right] \quad (3.49)$$

$$\delta_2^{(3)} = (l_3/g) \sum_p \frac{3\mu_p r_s^3}{2R_p^7} \left[5(\mathbf{r}_s \cdot \mathbf{R}_p)^2 - r_s^2 R_p^2 \right] (x_s Y_p - y_s X_p) / \sqrt{x_s^2 + y_s^2} \quad (3.50)$$

$$\delta_3^{(3)} = (l_3/g) \sum_p \frac{3\mu_p r_s^2}{2R_p^7} \left[5(\mathbf{r}_s \cdot \mathbf{R}_p)^2 - r_s^2 R_p^2 \right] \left[\sqrt{x_s^2 + y_s^2} Z_p - \frac{z_s}{\sqrt{x_s^2 + y_s^2}} (x_s X_p + y_s Y_p) \right], \quad (3.51)$$

where μ_p is the ratio of the mass of the disturbing body, p , to the mass of the Earth, and

$$\mathbf{R}_p = [X_p, Y_p, Z_p]^T \quad (3.52)$$

is the vector from the center of the Earth to that body. The summations are over tide-producing bodies, of which only the Sun and the Moon are normally included. Recent work considers low-level planetary contributions (Hartmann and Soffel, 1994; Hartmann and Wenzel, 1994; Williams, 1995), of which Venus' appear to be the most important. Mathews *et al.* (1995) have recently re-examined the basic definitions underlying the derivation of the tidal potential. They conclude that the most reasonable definition is one that uses the reference ellipsoid, and thus implies that the Love numbers have a slight latitude dependence.

The above formulation implicitly assumes that the Love numbers h_i and l_i are independent of the frequency of the tide-generating potential. A more accurate treatment entails a harmonic expansion of Eqs. (3.46)-(3.51) and use of a different set of h_i, l_i for each frequency component. Each harmonic term is denoted by its historical (Darwin) name, if one exists, and the Doodson code (IERS, 1992) (*e.g.*, K_1 has Doodson number = 165555). The Doodson notation classifies the tidal components according to increasing speed. The correction to the Love number which scales the solid tidal radial displacement for the k th harmonic term at station s is given by

$$\delta h_2^{sk} = 3 \sqrt{5/24\pi} \delta h_2^k H_k \sin \phi_s \cos \phi_s \sin(\lambda_s + \theta_k), \quad (3.53)$$

where δh_2^k is the difference between the nominal quadrupole Love number $h_2 = 0.609$ and the frequency dependent Love number (Wahr, 1979), H_k is the amplitude of the k th harmonic term in the tide generating expansion from Cartwright and Edden (1973), ϕ_s is the geocentric latitude of the station, λ_s is the East longitude of the station and θ_k is the k th harmonic tide argument. The Love numbers and tidal amplitudes of the six dominant nearly diurnal tides are listed in Table III. They yield purely vertical station displacements (Naudet, 1994) (in mm)

$$\psi_1 (166554) \quad \delta \Delta \delta_1 = 0.37 \sin 2\phi_s \sin(\lambda_s + \alpha_G + l') \quad (3.54)$$

$$(165565) \quad \delta \Delta \delta_1 = -1.84 \sin 2\phi_s \sin(\lambda_s + \alpha_G - \Omega) \quad (3.55)$$

$$K_1 (165555) \quad \delta \Delta \delta_1 = -12.68 \sin 2\phi_s \sin(\lambda_s + \alpha_G) \quad (3.56)$$

$$(165545) \quad \delta \Delta \delta_1 = 0.24 \sin 2\phi_s \sin(\lambda_s + \alpha_G + \Omega) \quad (3.57)$$

$$P_1 (163555) \quad \delta \Delta \delta_1 = 1.32 \sin 2\phi_s \sin[\lambda_s + \alpha_G - 2(\Omega + F - D)] \quad (3.58)$$

$$O_1 (145555) \quad \delta \Delta \delta_1 = 0.62 \sin 2\phi_s \sin[\lambda_s + \alpha_G - 2(\Omega + F)], \quad (3.59)$$

where ϕ_s, λ_s , and α_G are the station geocentric latitude and longitude and Greenwich RA, respectively. The astronomical arguments l', F, D, Ω (mean anomaly of the Sun, mean argument of the latitude of the Moon, mean elongation of the Moon from the Sun, and the mean longitude of the ascending lunar node) are defined in Sec. III.D. These displacements are then summed and the total is used as the first order correction to each station's vertical displacement. Horizontal corrections are presently ignored. Note that the largest correction, the K_1 term, is identical to that already recommended in 1983 by the MERIT standards (Melbourne *et al.*, 1983, 1985). A fairly complete recent treatment of the frequency dependence of tidal response has been given by Mathews *et al.* (1997). With such amendments, the solid tide model presented here should be adequate at the mm level.

To convert the locally referenced displacement, δ_{sol} , which is expressed in the local VEN coordinate system, to the Earth-fixed frame, two rotations must be performed. The first, \mathbf{W} , rotates by an angle $\phi_{s(\text{gd})}$ (station geodetic latitude) about the y axis to an equatorial system. The second, \mathbf{V} , rotates about the resultant z axis by an angle, $-\lambda_s$ (station longitude), to bring the displacements into the standard geocentric coordinate system. The result is

$$\mathbf{\Delta}_{\text{sol}} = \mathbf{V}\mathbf{W}\boldsymbol{\delta}_{\text{sol}}, \quad (3.60)$$

where

$$\mathbf{W} = \begin{pmatrix} \cos \phi_{s(\text{gd})} & 0 & -\sin \phi_{s(\text{gd})} \\ 0 & 1 & 0 \\ \sin \phi_{s(\text{gd})} & 0 & \cos \phi_{s(\text{gd})} \end{pmatrix}, \quad \mathbf{V} = \begin{pmatrix} \cos \lambda_s & -\sin \lambda_s & 0 \\ \sin \lambda_s & \cos \lambda_s & 0 \\ 0 & 0 & 1 \end{pmatrix}. \quad (3.61)$$

We calculate geodetic latitudes according to Bowring's (1976) formulation which properly accounts for stations that are at some altitude above the reference ellipsoid:

$$\phi_{s(\text{gd})} = \tan^{-1} \left[\frac{z_s + e_2^2 R_E \sin^3 \theta (1-f)}{r_{sp_s} - e_1^2 R_E \cos^3 \theta} \right], \quad (3.62)$$

where $r_{sp_s} = (x_s^2 + y_s^2)^{1/2}$ is the station radius from the Earth's spin axis, f ($\approx 1/300$) is the geoid flattening factor, $e_1^2 = 2f - f^2$, and $e_2^2 = e_1^2/(1 - e_1^2)$ are the first and second eccentricities squared, and

$$\theta = \tan^{-1} \left[\frac{z_s}{r_{sp_s} (1-f)} \right]. \quad (3.63)$$

Simpler formulas which assume that the station is on the ellipsoid make errors of order 10^{-7} radians for a mid-latitude station at 1 km altitude. The difference between geodetic and geocentric latitude can affect the tide model by as much as f times the tidal effect, or ≈ 1 mm.

b. Pole tide

One of the significant secondary tidal effects is the displacement of a station by the elastic response of the Earth's crust to shifts in the spin axis orientation. The spin axis is known to describe an approximately circular path of ≈ 20 -m diameter at the north pole with an irregular period of somewhat less than one year (see Fig. 16 in Sec. VI.B). Depending on where the spin axis pierces the crust at the instant of a VLBI measurement, the "pole tide" displacement will vary from time to time. This effect must be included if centimeter accuracy is desired.

Yoder (1984) and Wahr (1985) derived an expression for the displacement of a point at geodetic latitude $\phi_{s(\text{gd})}$ and longitude λ_s due to the pole tide:

$$\boldsymbol{\delta}_{\text{pol}} = -\frac{\omega_E^2 R_E}{g} \left[\begin{aligned} & \sin \phi_{s(\text{gd})} \cos \phi_{s(\text{gd})} (p_x \cos \lambda_s + p_y \sin \lambda_s) h \hat{\mathbf{r}} \\ & + \cos 2\phi_{s(\text{gd})} (p_x \cos \lambda_s + p_y \sin \lambda_s) l \hat{\boldsymbol{\phi}} \\ & + \sin \phi_{s(\text{gd})} (-p_x \sin \lambda_s + p_y \cos \lambda_s) l \hat{\boldsymbol{\lambda}} \end{aligned} \right]. \quad (3.64)$$

Here ω_E is the rotation rate of the Earth, R_E the equatorial radius of the Earth, g the acceleration due to gravity at the Earth's surface, and h and l the customary Love numbers. Displacements of the instantaneous spin axis from the long-term average spin axis along the x and y axes are given by p_x and p_y . Eq. (3.64) shows how these map into station displacements along the unit vectors in the radial ($\hat{\mathbf{r}}$), latitude ($\hat{\boldsymbol{\phi}}$), and longitude ($\hat{\boldsymbol{\lambda}}$) directions. With the standard values $\omega_E \approx 7.292 \times 10^{-5}$ rad/sec, $R_E \approx 6378$ km, and $g \approx 980.7$ cm/sec², the factor $\omega_E^2 R/g = 0.00346$. Since the maximum values of p_x and p_y are on the order of 10 meters, and $h \approx 0.6$, $l \approx 0.08$, the maximum displacement due to the pole tide is 1 to 2 cm, depending on the location of the station ($\phi_{s(\text{gd})}$, λ_s). The locally referenced displacement $\boldsymbol{\delta}_{\text{pol}}$ is transformed via the matrix $\mathbf{V}\mathbf{W}$ of Eqs. (3.61) to give the displacement $\mathbf{\Delta}_{\text{pol}}$ in the standard geocentric coordinate system.

c. Ocean loading

This section is concerned with another of the secondary tidal effects, namely the elastic response of the Earth’s crust to ocean tides, which moves the observing stations to the extent of a few cm. Such effects are commonly called “ocean loading.” The current standard model of ocean loading is general enough to accommodate externally derived parameters describing the tide phases and amplitudes at a number of frequencies. The locally referenced three-dimensional displacement δ_{ocn} (components δ_j) due to ocean loading is related to the frequencies ω_i , amplitudes ξ_{ij} , and phases φ_{ij} . In a local Cartesian coordinate system (usually with unit vectors in the vertical, East, and North directions) at time t ,

$$\delta_j = \sum_{i=1}^N \xi_{ij} \cos(\omega_i t + V_i - \varphi_{ij}) . \quad (3.65)$$

The quantities ω_i (frequency of tidal constituent i) and V_i (astronomical argument of constituent i) depend only on the ephemeris information (positions of the Sun and Moon). The algorithm of Goad (IERS, 1989; IERS, 1996b) is usually used to calculate these two quantities. On the other hand the amplitude ξ_{ij} and Greenwich phase lag φ_{ij} of component j are determined by the particular model assumed for the deformation of the Earth. The local displacement vector is transformed via Eqs. (3.61) to the displacement Δ_{ocn} in the standard geocentric frame.

In present models, the local displacements and their phases, ξ_{ij} and φ_{ij} , are calculated from ocean tidal loading models with as many as 11 frequencies. The eleven components are denoted, in standard notation: K_2 , S_2 , M_2 , and N_2 (all with approximately 12-hour periods), K_1 , P_1 , O_1 , Q_1 (24 h), M_f (14 day), M_m (monthly), and S_{sa} (semiannual).

Three ocean loading models have been used over the years. They differ in the displacements that are calculated and the number of components that are considered, as well as in the numerical values that they yield for ξ_{ij} and φ_{ij} . Scherneck’s results (1983; 1991) are the most complete in the sense of considering both vertical and horizontal displacements and all eleven tidal components. They have now been adopted for the IERS standards (1996b). Goad’s model (1983) was adopted in the MERIT and early IERS standards (1989), but only considers vertical displacements. Pagiatakis’s (1982) model (Pagiatakis, 1990), based on Pagiatakis *et al.* (1982), considers only six tidal components (S_2 , M_2 , N_2 , K_1 , P_1 , and O_1).

An extension of the 1991 Scherneck model (Scherneck, 1993) accounts for modulation of the eleven tidal frequencies by multiples of N' , which corresponds to the lunar nodal period (18.6 years). On the assumption that these additional terms yield ocean loading amplitudes which are in the same ratio to each main loading term as the companion tides are to the main tides, the additional station displacements can be written as

$$\delta'_j = \sum_{i=1}^N \sum_k r_{ki} \xi_{ij} \cos[(\omega_i + n_{ki} \omega_{N'})t + V_i + n_{ki} N' - \varphi_{ij}] , \quad (3.66)$$

where the k summation extends over all integer multiples n_{ki} of the lunar node N' , and r_{ki} is the ratio of the tidal amplitude of each companion k to the tidal amplitude of the parent i . Of 26 such components listed by Cartwright and Edden (1973), 20 are estimated to be significant in contributing to the largest ocean loading displacements at the 0.01 mm level. Table IV shows the multiples n_{ki} and amplitude ratios r_{ki} for these 20 components.

In pushing the limits of Earth modeling to below 1 cm accuracy in the mid-1990s, ocean loading station displacements are one aspect of the models that are undergoing close scrutiny. Initial studies indicate that ocean loading amplitudes can be derived from VLBI experiments at an approximate accuracy level of 1-2 mm (Sovers, 1994). When estimating parameters, great care must be used in order to avoid singularities due to the identity of certain components of station displacements due to nominally different physical effects (“confounding of parameters”). Since some components of ocean loading, solid Earth tides, and ocean tidally induced UTPM variations have the same frequencies, certain linear combinations of the station displacements that they cause are identical (see Secs. III.C.2.a and III.D.1.c).

3. Non-tidal station motion

Many other processes take place in the Earth’s atmosphere and in its crust that affect the location of an observing station on time scales ranging from seconds to years, and distance scales ranging from local to global. Present

knowledge of such processes is somewhat sketchy, but both theoretical and experimental research are starting to provide useful results. Local processes include the effects of ground water and snow cover redistribution (Chao, 1996), and magma chamber activity in volcanically active areas (Webb *et al.*, 1995). Effects that have more widespread repercussions are atmospheric loading and post-glacial relaxation. In contrast to the tidal effects, whose time dependence is fixed by the precisely known motions of the bodies of the Solar System, the non-tidal processes do not have well-known, periodic time dependencies. The two “global” effects, atmospheric loading and post-glacial relaxation, are discussed briefly in the next two sections. Two others have not yet been investigated in detail: non-tidal ocean surface height variations (Gaspar and Ponte, 1997), and surface displacements caused by pressure variations at the core-mantle boundary (Fang *et al.*, 1996).

a. Atmosphere loading

By analogy with the ocean tides that were considered in the previous section, a time-varying atmospheric pressure distribution can also induce crustal deformation. Rabbal and Schuh (1986) first estimated the effects of atmospheric loading on VLBI baseline determinations, and concluded that they may amount to many millimeters of seasonal variation. In contrast to ocean tidal effects, analysis of atmospheric loading does not benefit from the presence of a well-understood periodic driving force. Otherwise, estimation of atmospheric loading via Green’s function techniques is analogous to methods used to calculate ocean loading effects. Rabbal and Schuh recommend a simplified form of the dependence of the vertical crust displacement on pressure distribution. It involves only the instantaneous pressure at the site in question, and an average pressure anomaly over a circular region C of radius $R = 2000$ km surrounding the site. The expression for the vertical displacement (mm) is

$$\Delta r = -0.35\Delta p - 0.55\bar{p} , \quad (3.67)$$

where Δp is the local pressure anomaly ($p - p_{\text{STD}}$, mbar) relative to the standard pressure

$$p_{\text{STD}} = 1013.25 \exp(-h/8.567) . \quad (3.68)$$

The pressure anomaly \bar{p} (mbar) is averaged over the 2000-km circular region mentioned above. The site altitude h (km) should be calculated relative to the standard reference ellipsoid, using quantities defined in the solid Earth tide section above (Eq. 3.62):

$$h = \frac{r_{\text{sp}}}{\cos \phi_{\text{gd}}} - \frac{R_{\text{E}}}{\sqrt{1 - e_1^2 \sin^2 \phi_{\text{gd}}}} . \quad (3.69)$$

Note that the reference point for this displacement is the site location at its standard pressure. The locally referenced Δr is transformed to the standard geocentric coordinate system via the transformation of Eqs. (3.61).

Such a rudimentary model has been recently incorporated into VLBI analyses. A mechanism for characterizing the pressure anomaly \bar{p} expresses the two-dimensional surface pressure distribution (relative to the standard pressure) surrounding a site as a quadratic polynomial

$$p(x, y) = \Delta p + A_1 x + A_2 y + A_3 x^2 + A_4 xy + A_5 y^2 , \quad (3.70)$$

where x and y are the local East and North distances of the point in question from the VLBI site. The pressure anomaly may then be evaluated by the simple integration

$$\bar{p} = \frac{\iint_C dx dy p(x, y)}{\iint_C dx dy} , \quad (3.71)$$

giving

$$\bar{p} = \Delta p + (A_3 + A_5)R^2/4 \quad (3.72)$$

and

$$\Delta r = -0.90\Delta p - 0.14(A_3 + A_5)R^2 . \quad (3.73)$$

A quadratic fit to any available area pressure measurements can then determine the coefficients A_{1-5} . Future advances in understanding the atmosphere-crust elastic interaction can probably be accommodated by adjusting the coefficients in Eq. (3.67). As an initial step along these lines, a station-dependent factor f is introduced to scale the local coefficient in Eq. (3.73):

$$\Delta r = -0.90(1 + f)\Delta p - 0.14(A_3 + A_5)R^2 . \quad (3.74)$$

This may account for differing geographical features surrounding different sites. In particular, f may depend on the fraction of ocean within the 2000 km radius. Some recent analyses have produced empirical estimates of atmosphere loading coefficients for a number of sites (Manabe *et al.*, 1991; van Dam and Herring, 1994; MacMillan and Gipson, 1994; van Dam *et al.*, 1994). It is not yet clear whether the site-to-site variation of these coefficients is free from other systematic errors.

b. Post-glacial relaxation

Thick glacial ice sheets covering Scandinavia, Greenland, and Canada melted $\approx 10,000$ years ago. The removal of their considerable weight pressing on the Earth's crust is believed to result in relaxation ("rebound") that continues at present (Tushingham and Peltier, 1991). The magnitude of this motion is estimated to be as large as several mm/yr, predominantly in the vertical direction, at sites in and near the locations of ancient glaciers and ice sheets. Current theory of deglaciation effects is not yet sufficiently developed to produce definitive results. The parameters describing deglaciation history, as well as the rheological properties of the Earth's mantle, are not accurately known. Nevertheless, it appears that reasonable parameter choices yield some agreement with empirical measurements of baselines in the affected areas (Mitrovica *et al.*, 1993; Peltier, 1995).

In summary, models have been presented that describe the four major time-dependent station motions (solid, pole, and ocean tides, and atmospheric loading). Each of the locally referenced displacement vectors is then transformed to the standard geocentric coordinate system via rotations like Eq. (3.60). After this transformation, the final station location in the terrestrial frame is

$$\mathbf{r}_t = \mathbf{r}_0 + \Delta_{\text{sol}} + \Delta_{\text{pol}} + \Delta_{\text{ocn}} + \Delta_{\text{atm}} . \quad (3.75)$$

D. Earth orientation

The Earth is approximately an oblate spheroid, spinning in the presence of two massive moving objects, the Sun and the Moon. These are positioned such that their time-varying gravitational effects not only produce tides on the Earth, but also subject it to torques. In addition, the Earth is covered by a complicated fluid layer, and is not perfectly rigid internally. As a result, the orientation of the Earth is a very complicated function of time, which can be represented to first order as the composite of a time-varying rotation rate, a wobble, a nutation, and a precession. The exchange of angular momentum between the solid Earth and the fluids on its surface, as well as between its crust and deeper layers, is not readily predictable, and thus must be continually experimentally determined (Le Mouél *et al.*, 1993). Nutation and precession are fairly well modeled theoretically. At the accuracy with which VLBI can determine baseline vectors, however, even these models are not completely adequate.

Currently, the rotational transformation \mathbf{Q} of coordinates from the terrestrial frame to the celestial geocentric frame is composed of 6 separate transformations (actually 12 rotations, since the nutation, precession, and "perturbation" transformations \mathbf{N} , \mathbf{P} , and $\mathbf{\Omega}$ each consist of 3 rotations) applied to a vector in the terrestrial system:

$$\mathbf{Q} = \mathbf{\Omega P N U X Y} . \quad (3.76)$$

In order of appearance in Eq. (3.76), the transformations are the perturbation rotation, precession, nutation, UT1, and the x and y components of polar motion. All are discussed in detail in the following four sections. With this definition of \mathbf{Q} , if \mathbf{r}_t is a station location expressed in the terrestrial system, *e.g.*, the result of Eq. (3.75), then that location expressed in the geocentric celestial system is

$$\mathbf{r}_c = \mathbf{Q r}_t . \quad (3.77)$$

This particular formulation evolved from the historical development of astrometry, and is couched in that language. With modern measurement techniques, such a formulation is esthetically unsatisfactory, but it currently offers a practical way for merging VLBI results into the long historical record of astrometric data. The precession and nutation matrices (\mathbf{P} and \mathbf{N}) depend on two angles (nutation in celestial longitude $\Delta\psi$ and in obliquity $\Delta\varepsilon$) that vary slowly in the celestial reference frame. On the other hand, the UTPM matrices (\mathbf{U} , \mathbf{X} , and \mathbf{Y}) depend on three angles that vary slowly in a terrestrial reference frame co-rotating with the Earth. Thus the desire to have expressions that vary slowly with time led to a description that uses 5 angles to specify the orientation of the Earth, rather than the absolute minimum of 3 angles. Recently improving measurement accuracy demands high-frequency terms in \mathbf{UXY} , some of which duplicate parts of \mathbf{N} , and thus negate the advantages of the historical decomposition. Esthetically it would be much more pleasing to separate \mathbf{Q} into two rotation matrices:

$$\mathbf{Q} = \mathbf{Q}_1 \mathbf{Q}_2 , \quad (3.78)$$

where \mathbf{Q}_2 are those rotations to which the Earth would be subjected if all external torques were removed (approximately \mathbf{UXY} above), and where \mathbf{Q}_1 are those rotations arising from external torques (approximately $\mathbf{\Omega PN}$ above). Even then, the tidal response of the Earth prevents such a separation from being perfectly realized. Eventually, the entire problem of obtaining the matrix \mathbf{Q} and the tidal effects on station locations may be solved numerically. Note that the matrices appearing in the transformation of Eq. (3.76) are not the same as those historically used in astrometry. Since we rotate the Earth from “of date” to J2000.0 (rather than the celestial sphere from J2000.0 to coordinates of date), the matrices $\mathbf{\Omega}$, \mathbf{P} , and \mathbf{N} are transposes of the conventional transformations. We will now consider each of the rotations \mathbf{Y} , \mathbf{X} , \mathbf{U} , \mathbf{N} , \mathbf{P} , and $\mathbf{\Omega}$ in detail.

1. UT1 and polar motion

The Earth’s instantaneous spin axis traces a quasi-circular, quasi-periodic path approximately 20 m in diameter with a “period” somewhat less than one year, which is known as polar motion (see Fig. 16 in Sec. VI.B). The first transformation, \mathbf{Y} , is a right-handed rotation about the x axis of the terrestrial frame by an angle Θ_2 . Currently, the terrestrial frame is the CIO 1903 frame, except that the positive y axis is at 90 degrees east (toward Bangladesh). The x axis is coincident with the 1903.0 meridian of Greenwich, and the z axis is the 1903.0 standard pole.

$$\mathbf{Y} = \begin{pmatrix} 1 & 0 & 0 \\ 0 & \cos \Theta_2 & \sin \Theta_2 \\ 0 & -\sin \Theta_2 & \cos \Theta_2 \end{pmatrix} , \quad (3.79)$$

where Θ_2 is the y pole position published by IERS.

The next rotation in sequence is the right-handed rotation (through an angle Θ_1 about the y axis) obtained after the previous rotation has been applied:

$$\mathbf{X} = \begin{pmatrix} \cos \Theta_1 & 0 & -\sin \Theta_1 \\ 0 & 1 & 0 \\ \sin \Theta_1 & 0 & \cos \Theta_1 \end{pmatrix} . \quad (3.80)$$

In this rotation, Θ_1 is the IERS x pole position. Note that we have incorporated in the matrix definitions the transformation from the left-handed system used by IERS to the right-handed system we use. Note also that instead of IERS data used as a pole definition, we could instead use any other source of polar motion data provided it was represented in a left-handed system. The only effect would be a change in the definition of the terrestrial reference system.

The application of \mathbf{XY} to a vector in the terrestrial system of coordinates expresses that vector as it would be observed in a coordinate frame whose z axis was along the Earth’s ephemeris pole. The third rotation, \mathbf{U} , is about the resultant z axis obtained by applying \mathbf{XY} . It is a rotation through the angle $-H$, where H is the hour angle of the true equinox of date (*i.e.*, the dihedral angle measured westward between the xz plane defined above and the meridian plane containing the true equinox of date):

$$\mathbf{U} = \begin{pmatrix} \cos H & -\sin H & 0 \\ \sin H & \cos H & 0 \\ 0 & 0 & 1 \end{pmatrix} . \quad (3.81)$$

The equinox of date is the point defined on the celestial equator by the intersection of the mean ecliptic with that equator. It is that intersection where the mean ecliptic rises from below the equator to above it (ascending node). This angle H is composed of two parts:

$$H = h_{\Upsilon} + \alpha_E , \quad (3.82)$$

where h_{Υ} is the hour angle of the mean equinox of date, and α_E (equation of the equinoxes) is the difference in hour angle of the true equinox of date and the mean equinox of date, a difference which is due to the nutation of the Earth. This set of definitions is cumbersome and couples nutation effects with Earth rotation. However, in order to provide a direct estimate of conventional UT1 (universal time) it is necessary to endure this historical approach.

UT1 is defined to be such that the hour angle of the mean equinox of date is given by the following expression (Aoki *et al.*, 1982; Kaplan, 1981):

$$h_{\Upsilon} = \text{UT1} + 6^{\text{h}} 41^{\text{m}} 50^{\text{s}}.54841 + 8640184^{\text{s}}.812866 T + 0^{\text{s}}.093104 T^2 - 6^{\text{s}}.2 \times 10^{-6} T^3 , \quad (3.83)$$

where the quantity

$$T = (\text{Julian UT1 date} - 2451545.0)/36525.0 \quad (3.84)$$

represents the number of Julian centuries since J2000.0. An equivalent expression which is normally used is

$$h_{\Upsilon} = 86400^{\text{s}}(\text{UT1 Julian day fraction}) + 67310^{\text{s}}.54841 + 8640184^{\text{s}}.812866 T + 0^{\text{s}}.093104 T^2 - 6^{\text{s}}.2 \times 10^{-6} T^3 . \quad (3.85)$$

This expression produces a time UT1 which tracks the Greenwich hour angle of the real Sun to within 16^{m} . However, it really is sidereal time, modified to fit our intuitive desire to have the Sun directly overhead at noon on the Greenwich meridian. Historically, differences of UT1 from a uniform measure of time, such as atomic time (UTC or TAI), have been used in specifying the orientation of the Earth (see the plot of UT1–TAI in Fig. 17 of Sec. VI.B).

By the very definition of “mean of date” and “true of date”, nutation causes a difference in the hour angles of the mean equinox of date and the true equinox of date. This difference, called the “equation of the equinoxes”, is denoted by α_E and is obtained as follows:

$$\alpha_E = \tan^{-1} \left(\frac{y_{\Upsilon'}}{x_{\Upsilon'}} \right) = \tan^{-1} \left(\frac{N_{21}^{-1}}{N_{11}^{-1}} \right) = \tan^{-1} \left(\frac{N_{12}}{N_{11}} \right) , \quad (3.86)$$

where the vector

$$\begin{pmatrix} x'_{\Upsilon} \\ y'_{\Upsilon} \\ z'_{\Upsilon} \end{pmatrix} = N^{-1} \begin{pmatrix} 1 \\ 0 \\ 0 \end{pmatrix} \quad (3.87)$$

is the unit vector, in true equatorial coordinates of date, toward the mean equinox of date. In mean equatorial coordinates of date, this same unit vector is just $(1, 0, 0)^T$. The matrix \mathbf{N}^{-1} is the inverse (or equally, the transpose) of the transformation matrix \mathbf{N} , which will be defined below in Eq. (3.101), to effect the transformation from true equatorial coordinates of date to mean equatorial coordinates of date. To a very good approximation,

$$\alpha_E = \Delta\psi \cos(\bar{\varepsilon} + \Delta\varepsilon) . \quad (3.88)$$

The IERS Conventions (1992) had recommended a slightly different expression, which uses the mean obliquity $\bar{\varepsilon}$ rather than the true obliquity $\bar{\varepsilon} + \Delta\varepsilon$, and can change α_E by a few nanoradians:

$$\alpha_E = \Delta\psi \cos \bar{\varepsilon} . \quad (3.89)$$

More recently, the IERS (1996b) recommends including two additional terms so that the equation of the equinoxes involves the longitude of the lunar node Ω (to be defined in Sec. III.D.2):

$$\alpha_E = \Delta\psi \cos \bar{\varepsilon} + 0.''00264 \sin \Omega + 0.''000063 \sin 2\Omega . \quad (3.90)$$

This expression should be used in analyses done after 1 January, 1997 (including re-analyses of old data). That particular date is chosen to minimize the discontinuity of α_E ($\Omega = \pi$ on 26 February, 1997). One last note on the equation of the equinoxes: augmentation of the *a priori* precession constant will shift the position of the celestial ephemeris pole and thus require an adjustment to the equation of the equinoxes

$$\Delta\alpha_E = \Delta p_{LS} \cos \bar{\epsilon} - \Delta p_{PL} , \quad (3.91)$$

where Δp_{LS} and Δp_{PL} are the *a priori* shifts in lunisolar and planetary precession constants, respectively.

It is convenient to apply \mathbf{UXY} as a group. To parts in 10^{12} , $\mathbf{XY} = \mathbf{YX}$. However, to the same accuracy $\mathbf{UXY} \neq \mathbf{XYU}$. Neglecting terms of $O(\Theta^2)$ (which produce station location errors of approximately 0.006 mm):

$$\mathbf{UXY} = \begin{pmatrix} \cos H & -\sin H & -\sin \Theta_1 \cos H - \sin \Theta_2 \sin H \\ \sin H & \cos H & -\sin \Theta_1 \sin H + \sin \Theta_2 \cos H \\ \sin \Theta_1 & -\sin \Theta_2 & 1 \end{pmatrix} . \quad (3.92)$$

Over relatively short time spans, Earth rotation might be modeled as a time-linear function, by analogy with tectonic motion of the stations over longer periods. If the x, y components of polar motion and UT1 are symbolized by Θ_{1-3} , and the reference time is t_0 , then this model is

$$\Theta_i = \Theta_i^0 + \dot{\Theta}_i(t - t_0) , \quad (3.93)$$

where Θ_i^0 are the values of UTPM at the reference epoch.

a. Tidal UTPM variations

Tidally induced shifts of mass in the solid Earth, oceans, and atmosphere carry angular momenta which must be redistributed in a manner that conserves the total angular momentum. This leads to variations in the orientation and rotation rate of the Earth: modification of polar motion and UT1. Such small effects emerged above the detection threshold in space geodesy in the early 1990s. Modeling them is important if sub-centimeter accuracy is to be attained in the interpretation of VLBI measurements.

Just as various tidal forces affect the station locations (Secs. III.C.2.a - III.C.2.c), they also affect polar motion and UT1 (Θ_{1-3}). Equations similar to (3.35) may be written for each of the three components of Earth orientation:

$$\Theta_i = \Theta_{i0} + \Delta\Theta_{i\text{sol}} + \Delta\Theta_{i\text{ocn}} + \Delta\Theta_{i\text{atm}} , \quad (3.94)$$

where Θ_i ($i=1,3$) symbolizes each of the three components of UTPM, Θ_{i0} is its value in the absence of tidal effects, and the three Δ terms are the respective contributions of solid Earth, ocean, and atmospheric tides. The next two sections describe the current models of solid and ocean tide contributions that are presently included in VLBI analyses. At present not enough is known about atmospheric tidal effects, and only loose upper limits can be placed on their contribution.

b. Solid Earth tide UTPM variations

The pioneering work in tidal effects on Earth orientation was that of (Yoder *et al.*, 1981). It was limited to UT1, and included solid tidal and some ocean tidal effects. Their calculated ΔUT1 can be represented as

$$\Delta\text{UT1} = \sum_{i=1}^N \left[A_i \sin \left(\sum_{j=1}^5 k_{ij} \alpha_j \right) \right] , \quad (3.95)$$

where $N=41$ is chosen to include all terms with periods from 5 to 35 days. There are no longer-period contributions until a period of 90 days is reached. However, these long-period terms (*e.g.* IERS, 1996b) are already included in the results reported by the current Earth-orientation measurement services. The values for k_{ij} and A_i , along with the periods involved, are given in Table 4.37.1 of the *Explanatory Supplement* (Archinal, 1992a). The α_j are just the five fundamental arguments defined in Eqs. (3.104 - 3.108) as l, l', F, D , and Ω , respectively.

c. Ocean tide UTPM variations

Redistribution of the angular momentum produced by ocean tides affects the Earth's rotation pole position and velocity. This effect was first quantified by Brosche (1982), Baader *et al.* (1983), and Brosche *et al.* (1989; 1991). The dominant effects on polar motion and UT1 occur at diurnal, semidiurnal, fortnightly, monthly, and semiannual tidal periods. Assuming that the periods longer than one day are adequately accounted for either in modeling which combines solid and ocean tidal effects (not strictly true with the Yoder model), or are already present in the *a priori* UTPM series, only the diurnal and semidiurnal frequencies need to be modeled. Further limiting the model to tidal components with apparent amplitudes larger than $1 \mu\text{s}$ gives eight components.

For unified notation, again define Θ_l ($l=1,3$) = x, y polar motion and UT1, respectively. Then the ocean tidal effects $\Delta\Theta$ can be written as

$$\Delta\Theta_l = \sum_{i=1}^N \left[A_{il} \cos \left(\sum_{j=1}^5 k_{ij} \alpha_j + n_i (h\Upsilon + \pi) \right) + B_{il} \sin \left(\sum_{j=1}^5 k_{ij} \alpha_j + n_i (h\Upsilon + \pi) \right) \right], \quad (3.96)$$

A_{il} and B_{il} are the cosine and sine amplitudes that may be calculated from theoretical tidal models (as in the work of Brosche) or empirically determined from data (Sovers *et al.*, 1993; Herring and Dong, 1994; Watkins *et al.*, 1994; Gipson, 1996). Table V lists the eight dominant terms in the model. These numerical coefficients are taken from the empirical results of Sovers *et al.* (1993), and are representative of a number of recent empirical models. Note that the K_1 terms contain large arbitrary conventional components, and are thus not solely due to ocean effects. Theoretical calculations of polar motion ocean effects have been made by Chao *et al.* (1996), yielding the amplitudes A_{il} and B_{il} using models based on TOPEX/Poseidon altimetry (Fu *et al.*, 1994). The theoretical results agree well with empirical determinations, and confirm the dominant role of ocean tides in excitation of short-period UTPM variations.

The ocean tidal UTPM effects are also modulated by the 18.6-year lunar node variation N' . As in the case of ocean loading station displacements (Sec. III.C.2.c), the contributions $\Delta\Theta_l'$ of the companion tides to $\Delta\Theta_l$ can be written as

$$\Delta\Theta_l' = \sum_{i=1}^N \sum_k r_{ki} \left[A_{il} \cos \left(\sum_{j=1}^5 k_{ij} \alpha_j + n_i (h\Upsilon + \pi) + n_{ki} \omega_{N'} t + n_{ki} N' \right) + B_{il} \sin \left(\sum_{j=1}^5 k_{ij} \alpha_j + n_i (h\Upsilon + \pi) + n_{ki} \omega_{N'} t + n_{ki} N' \right) \right], \quad (3.97)$$

where the strengths of the companion tides r_{ki} are found in Table IV.

Polar motion as seen in the reference frame B which rotates with the Earth is identical to nutation in the space-fixed celestial frame S . A rotational frequency $\omega_B = 1$ cycle per sidereal day (cpsd) is identical to $\omega_S = 0$, while $\omega_B = 0$ corresponds to $\omega_S = -1$ cpsd. Generally, nutations at frequency ω_S correspond to polar motions with frequencies $\omega_B = -1 + \omega_S$. The retrograde diurnal parts of the polar motion terms with coefficients $A_{i(1,2)}$ and $B_{i(1,2)}$ corresponding to the tidal components listed in Table V ($i = 5$ to 8) are thus equivalent to components of the nutation model, and due care must be taken when both classes of parameters are estimated.

2. Nutation

With the completion of the UT1 and polar motion transformations, we are left with a station location vector, $\mathbf{r}_{\text{date}} = \mathbf{UXYr}_t$. This is the station location relative to true equatorial celestial coordinates of date. The last set of transformations are nutation \mathbf{N} , precession \mathbf{P} , and the perturbation rotation $\mathbf{\Omega}$, applied in that order. These transformations give the station location \mathbf{r}_c in celestial equatorial coordinates:

$$\mathbf{r}_c = \mathbf{\Omega P N r}_{\text{date}}. \quad (3.98)$$

The first of these transformations, the matrix \mathbf{N} , is a product of three separate rotations (Melbourne *et al.*, 1968):

1. $\mathbf{A}(\varepsilon)$: true equatorial coordinates of date to ecliptic coordinates of date,

$$\mathbf{A}(\varepsilon) = \begin{pmatrix} 1 & 0 & 0 \\ 0 & \cos \varepsilon & \sin \varepsilon \\ 0 & -\sin \varepsilon & \cos \varepsilon \end{pmatrix}, \quad (3.99)$$

where ε is the true obliquity of the ecliptic of date,

2. $\mathbf{C}^T(\Delta\psi)$: nutation in longitude from ecliptic coordinates of date to mean ecliptic coordinates of date,

$$\mathbf{C}^T(\Delta\psi) = \begin{pmatrix} \cos \Delta\psi & \sin \Delta\psi & 0 \\ -\sin \Delta\psi & \cos \Delta\psi & 0 \\ 0 & 0 & 1 \end{pmatrix}, \quad (3.100)$$

where $\Delta\psi$ is the nutation in ecliptic longitude, and

3. $\mathbf{A}^T(\bar{\varepsilon})$: ecliptic coordinates of date to mean equatorial coordinates.

In ecliptic coordinates of date, the mean equinox is at an angle $\Delta\psi$. The angle $\Delta\varepsilon = \varepsilon - \bar{\varepsilon}$ is the nutation in obliquity, and $\bar{\varepsilon}$ is the mean obliquity (the dihedral angle between the plane of the ecliptic and the mean plane of the equator). ‘‘Mean’’ as used in this section implies that the short-period ($T \leq 18.6$ years) effects of nutation have been removed. Actually, the separation between nutation and precession is rather arbitrary, but historical. The net rotation is

$$\begin{aligned} \mathbf{N} &= \mathbf{A}^T(\bar{\varepsilon})\mathbf{C}^T(\Delta\psi)\mathbf{A}(\varepsilon) \\ &= \begin{pmatrix} \cos \Delta\psi & \cos \varepsilon \sin \Delta\psi & \sin \varepsilon \sin \Delta\psi \\ -\cos \bar{\varepsilon} \sin \Delta\psi & \cos \bar{\varepsilon} \cos \varepsilon \cos \Delta\psi + \sin \bar{\varepsilon} \sin \varepsilon & \cos \bar{\varepsilon} \sin \varepsilon \cos \Delta\psi - \sin \bar{\varepsilon} \cos \varepsilon \\ -\sin \bar{\varepsilon} \sin \Delta\psi & \sin \bar{\varepsilon} \cos \varepsilon \cos \Delta\psi - \cos \bar{\varepsilon} \sin \varepsilon & \sin \bar{\varepsilon} \sin \varepsilon \cos \Delta\psi + \cos \bar{\varepsilon} \cos \varepsilon \end{pmatrix}. \end{aligned} \quad (3.101)$$

It should again be pointed out (see Sec. III.D above) that this is the reverse of the customary astronomical nutation.

The 1980 IAU nutation model (Seidelmann, 1982; Kaplan, 1981) is used to obtain the values of $\Delta\psi$ and $\varepsilon - \bar{\varepsilon}$. The mean obliquity is obtained from Lieske *et al.* (1977) or from Kaplan (1981):

$$\bar{\varepsilon} = 23^\circ 26' 21.''448 - 46.''8150 T - 5.''9 \times 10^{-4} T^2 + 1.''813 \times 10^{-3} T^3, \quad (3.102)$$

$$T = (\text{Julian TDB date} - 2451545.0)/36525.0. \quad (3.103)$$

The nutation in longitude $\Delta\psi$ and in obliquity $\Delta\varepsilon = \varepsilon - \bar{\varepsilon}$ can be represented by a series expansion of the sines and cosines of linear combinations of five fundamental arguments. The latter are nearly linear in time (Kaplan, 1981; Hohenkerk *et al.*, 1992) (in radians):

1. the mean anomaly of the Moon:

$$\alpha_1 = l = 2.35554839 + 8328.69142288T + 1.5180 \times 10^{-4} T^2 + 3.1 \times 10^{-7} T^3, \quad (3.104)$$

2. the mean anomaly of the Sun:

$$\alpha_2 = l' = 6.24003594 + 628.30195602T - 2.80 \times 10^{-6} T^2 - 5.8 \times 10^{-8} T^3, \quad (3.105)$$

3. the mean argument of latitude of the Moon:

$$\alpha_3 = F = 1.62790193 + 8433.46615832T - 6.4272 \times 10^{-5} T^2 + 5.3 \times 10^{-8} T^3, \quad (3.106)$$

4. the mean elongation of the Moon from the Sun:

$$\alpha_4 = D = 5.19846951 + 7771.37714617T - 3.341 \times 10^{-5} T^2 + 9.2 \times 10^{-8} T^3, \quad (3.107)$$

5. the mean longitude of the lunar ascending node on the ecliptic:

$$\alpha_5 = \Omega = 2.18243862 - 33.75704593T + 3.614 \times 10^{-5}T^2 + 3.9 \times 10^{-8}T^3 . \quad (3.108)$$

With these fundamental arguments, the 1980 IAU nutation quantities can then be represented by

$$\Delta\psi = \sum_{j=1}^N \left[(A_{0j} + A_{1j}T) \sin \left(\sum_{i=1}^5 k_{ji}\alpha_i(T) \right) \right] \quad (3.109)$$

and

$$\Delta\varepsilon = \sum_{j=1}^N \left[(B_{0j} + B_{1j}T) \cos \left(\sum_{i=1}^5 k_{ji}\alpha_i(T) \right) \right] , \quad (3.110)$$

where the various values of α_i , k_{ji} , A_j , and B_j are tabulated in Table 3.222.1 of the *Explanatory Supplement*.

Inadequacies of the standard nutation model can be corrected by adding various classes of terms to the nutations $\Delta\psi$ and $\Delta\varepsilon$ in Eqs. (3.109) and (3.110). These include the out-of-phase nutations, the free-core nutations (Yoder, 1983) with period ω_f (nominally 430 days), and the “nutation tweaks” $\delta\psi$ and $\delta\varepsilon$, which are arbitrary constant increments of the nutation angles $\Delta\psi$ and $\Delta\varepsilon$. Unlike the usual nutation expressions, the tweaks have no time dependence. The out-of-phase nutations $\Delta\psi^o$ and $\Delta\varepsilon^o$, which are not included in the 1980 IAU nutation series, are identical to Eqs. (3.109) and (3.110), with the replacements $\sin \leftrightarrow \cos$:

$$\Delta\psi^o = \sum_{j=1}^N \left[(A_{2j} + A_{3j}T) \cos \left(\sum_{i=1}^5 k_{ji}\alpha_i(T) \right) \right] \quad (3.111)$$

and

$$\Delta\varepsilon^o = \sum_{j=1}^N \left[(B_{2j} + B_{3j}T) \sin \left(\sum_{i=1}^5 k_{ji}\alpha_i(T) \right) \right] . \quad (3.112)$$

Expressions similar to these are adopted for the free-core nutations:

$$\Delta\psi^f = (A_{00} + A_{10}T) \sin(\omega_f T) + (A_{20} + A_{30}T) \cos(\omega_f T) \quad (3.113)$$

and

$$\Delta\varepsilon^f = (B_{00} + B_{10}T) \cos(\omega_f T) + (B_{20} + B_{30}T) \sin(\omega_f T) . \quad (3.114)$$

Since the free-core nutation is retrograde, ω_f is negative. The nutation model thus contains a total of 856 parameters: A_{ij} ($i=0,3; j=1,106$) and B_{ij} ($i=0,3; j=1,106$) plus the free-nutation amplitudes A_{i0} ($i=0,3$), B_{i0} ($i=0,3$). The only nonzero *a priori* amplitudes are the A_{0j} , A_{1j} , B_{0j} , B_{1j} ($j=1,106$).

The nutation tweaks are just constant additive factors to the angles $\Delta\psi$ and $\Delta\varepsilon$:

$$\Delta\psi \rightarrow \Delta\psi + \delta\psi \quad \text{and} \quad \Delta\varepsilon \rightarrow \Delta\varepsilon + \delta\varepsilon . \quad (3.115)$$

Deficiencies in the IAU nutation model became clearly evident in the 1980s (Herring *et al.*, 1986). Several methods of correcting them are in current use. The first possibility is to use empirically determined values of $\delta\psi$, $\delta\varepsilon$ that are available from the IERS (see also Fig. 18 in Sec. VI.B). With this choice the nutation angles are determined by interpolating among results from other VLBI experiments near the date of interest. An alternative is to estimate $\delta\psi$ and $\delta\varepsilon$ directly from the data.

Another avenue for improving the *a priori* nutation model is to select one of the published replacements of the 1980 IAU series. Early work by Zhu *et al.* (1989; 1990) refined the 1980 IAU theory of nutation both by re-examining the underlying Earth model and by incorporating experimental results. Herring (1991) has extended the work of Zhu *et al.* and used geophysical parameters from Mathews *et al.* (1991) to generate the ZMOA 1990-2 (Zhu, Mathews, Oceans, Anelasticity) nutation series. Kinoshita and Souchay (1990) have re-examined the rigid-Earth nutation theory, and attempted to include all terms larger than 0.005 mas, in particular planetary terms not present in any previous

theories. The 263 lunisolar terms have been corrected for the Earth's non-rigidity (Souchay, 1993). Other additions and corrections to the Kinoshita-Souchay model are found in Souchay and Kinoshita (1996), Williams (1994; 1995), and Hartmann *et al.* (1996).

The Kinoshita-Souchay planetary contributions to $\Delta\psi$ and $\Delta\varepsilon$ are

$$\Delta\psi = \sum_{j=1}^N \left[S_{\psi_j} \sin \left(\sum_{i=1}^{10} k_{ji} \beta_i(T) \right) + C_{\psi_j} \cos \left(\sum_{i=1}^{10} k_{ji} \beta_i(T) \right) \right] \quad (3.116)$$

and

$$\Delta\varepsilon = \sum_{j=1}^N \left[S_{\varepsilon_j} \sin \left(\sum_{i=1}^{10} k_{ji} \beta_i(T) \right) + C_{\varepsilon_j} \cos \left(\sum_{i=1}^{10} k_{ji} \beta_i(T) \right) \right], \quad (3.117)$$

where the astronomical arguments are symbolized by β_i ; the last four β_i are identical with the α_i defined above ($\beta_7 = D = \alpha_4$, $\beta_8 = F = \alpha_3$, $\beta_9 = l = \alpha_1$, $\beta_{10} = \Omega = \alpha_5$), while the first five are mean heliocentric longitudes of the planets (in units of radians):

$$1. \text{ Venus : } \beta_1 = l_V = 3.176146697 + 1021.3285546 T, \quad (3.118)$$

$$2. \text{ Earth : } \beta_2 = l_E = 1.753470314 + 628.30758492 T, \quad (3.119)$$

$$3. \text{ Mars : } \beta_3 = l_M = 6.203480913 + 334.06124315 T, \quad (3.120)$$

$$4. \text{ Jupiter : } \beta_4 = l_J = 0.599546497 + 52.96909651 T, \quad (3.121)$$

$$5. \text{ Saturn : } \beta_5 = l_S = 0.874016757 + 21.32990954 T, \quad (3.122)$$

and the sixth is the accumulated general precession:

$$\beta_6 = p_A = 0.02438175 T + 5.38691 \times 10^{-6} T^2. \quad (3.123)$$

It should be noted that the paper of Kinoshita and Souchay gives expressions for the lunisolar tidal arguments that are slightly at variance with the IAU formulas presented above in Eqs. (3.104 - 3.108). These differences may be of significance in high-accuracy modeling studies.

Since the present standard model of nutation is known to be in error by amounts that are large in comparison to present measurement capabilities (see Fig. 18 in Sec. VI.B), the International Astronomical Union considers it important to formulate and adopt an improved nutation model by the end of the century. A working group is presently considering variants of the ZMOA and Kinoshita-Souchay models in this connection. In the meantime, the IERS (1996a) maintains empirical time series of the nutation angles $\Delta\psi$, $\Delta\varepsilon$ for use in applications that require higher accuracy than the 1980 IAU model.

3. Precession

The next transformation in going from the terrestrial frame to the celestial frame is the rotation \mathbf{P} . This is the precession transformation from mean equatorial coordinates of date to the equatorial coordinates of the reference epoch (*e.g.*, J2000.0). As was the case with the nutation matrix of Eq. (3.101), this is a rotation whose sense is opposite to that of the conventional astrometric precession. It is a composite of three rotations discussed in detail by Melbourne *et al.* (1968) and Lieske *et al.* (1977):

$$\mathbf{R}(-Z) = \begin{pmatrix} \cos Z & \sin Z & 0 \\ -\sin Z & \cos Z & 0 \\ 0 & 0 & 1 \end{pmatrix}, \quad (3.124)$$

$$\mathbf{Q}(\Theta) = \begin{pmatrix} \cos \Theta & 0 & \sin \Theta \\ 0 & 1 & 0 \\ -\sin \Theta & 0 & \cos \Theta \end{pmatrix}, \quad (3.125)$$

$$\mathbf{R}(-\zeta) = \begin{pmatrix} \cos \zeta & \sin \zeta & 0 \\ -\sin \zeta & \cos \zeta & 0 \\ 0 & 0 & 1 \end{pmatrix}. \quad (3.126)$$

$$\mathbf{P} = \mathbf{R}(-\zeta)\mathbf{Q}(\Theta)\mathbf{R}(-Z) \quad (3.127)$$

$$= \begin{pmatrix} \cos \zeta \cos \Theta \cos Z - \sin \zeta \sin Z & \cos \zeta \cos \Theta \sin Z + \sin \zeta \cos Z & \cos \zeta \sin \Theta \\ -\sin \zeta \cos \Theta \cos Z - \cos \zeta \sin Z & -\sin \zeta \cos \Theta \sin Z + \cos \zeta \cos Z & -\sin \zeta \sin \Theta \\ -\sin \Theta \cos Z & -\sin \Theta \sin Z & \cos \Theta \end{pmatrix}.$$

The auxiliary angles ζ , Θ , Z depend on precession constants, obliquity, and time as

$$\zeta = 0.5mT + 0''.30188 T^2 + 0''.017998 T^3 \quad (3.128)$$

$$Z = 0.5mT + 1''.09468 T^2 + 0''.018203 T^3 \quad (3.129)$$

$$\Theta = nT - 0''.42665 T^2 - 0''.041833 T^3, \quad (3.130)$$

where the speeds of precession in right ascension and declination are, respectively,

$$m = p_{\text{LS}} \cos \bar{\epsilon}_0 - p_{\text{PL}} \quad (3.131)$$

$$n = p_{\text{LS}} \sin \bar{\epsilon}_0 \quad (3.132)$$

and p_{LS} = the lunisolar precession constant (including the geodesic precession), p_{PL} = the planetary precession constant, $\bar{\epsilon}_0$ = the obliquity at J2000.0, and T (Eq. 3.103) is the time in centuries past J2000.0. Nominal values at J2000.0 are $p_{\text{LS}} = 5038''.7784/\text{cy}$, $p_{\text{PL}} = 10''.5526/\text{cy}$; these yield the expressions given by Lieske *et al.* (1977) and Kaplan (1981):

$$\zeta = 2306''.2181 T + 0''.30188 T^2 + 0''.017998 T^3 \quad (3.133)$$

$$\Theta = 2004''.3109 T - 0''.42665 T^2 - 0''.041833 T^3 \quad (3.134)$$

$$Z = 2306''.2181 T + 1''.09468 T^2 + 0''.018203 T^3, \quad (3.135)$$

Direct estimates of precession corrections can be obtained from observations. The most recent such results (Charlot *et al.*, 1995; Walter and Sovers, 1996) indicate that the current IAU nominal value of p_{LS} is in error by -3.0 ± 0.2 milliarcseconds per year. The precession matrix completes the standard model for the orientation of the Earth.

4. Perturbation rotation

For exploring departures from the canonical precession, nutation, and UTPM transformations, the standard model for the rotation of the Earth as a whole may be modified by small incremental rotations about the resulting axes. Define such a perturbation rotation matrix as

$$\mathbf{\Omega} = \mathbf{\Delta}_x \mathbf{\Delta}_y \mathbf{\Delta}_z, \quad (3.136)$$

where

$$\mathbf{\Delta}_x = \begin{pmatrix} 1 & 0 & 0 \\ 0 & 1 & \delta\Theta_x \\ 0 & -\delta\Theta_x & 1 \end{pmatrix} \quad (3.137)$$

with $\delta\Theta_x$ being a small angle rotation about the x axis, in the sense of carrying y into z ;

$$\mathbf{\Delta}_y = \begin{pmatrix} 1 & 0 & -\delta\Theta_y \\ 0 & 1 & 0 \\ \delta\Theta_y & 0 & 1 \end{pmatrix} \quad (3.138)$$

with $\delta\Theta_y$ being a small angle rotation about the y axis, in the sense of carrying z into x ; and

$$\mathbf{\Delta}_z = \begin{pmatrix} 1 & \delta\Theta_z & 0 \\ -\delta\Theta_z & 1 & 0 \\ 0 & 0 & 1 \end{pmatrix} \quad (3.139)$$

with $\delta\Theta_z$ being a small angle rotation about the z axis, in the sense of carrying x into y . For angles on the order of 1 arc second we can neglect terms on the order $\delta\Theta^2 R_E$ as they give effects on the order of 0.15 mm. Thus, in that approximation

$$\mathbf{\Omega} = \begin{pmatrix} 1 & \delta\Theta_z & -\delta\Theta_y \\ -\delta\Theta_z & 1 & \delta\Theta_x \\ \delta\Theta_y & -\delta\Theta_x & 1 \end{pmatrix}. \quad (3.140)$$

Each of the rotation angles can be expressed as a function of time:

$$\delta\Theta_i = \delta\Theta_i(T) = \delta\Theta_{i0} + \delta\dot{\Theta}_i T + f_i(T), \quad (3.141)$$

which is the sum of an offset, a time-linear rate, and some higher order or oscillatory terms. In particular, a non-zero value of $\delta\dot{\Theta}_y$ is equivalent to a change in the precession constant, and $\delta\dot{\Theta}_x$ is equivalent to the time rate of change of the obliquity ε . Setting

$$\delta\Theta_x = \delta\Theta_y = \delta\Theta_z = 0 \quad (3.142)$$

gives the effect of applying only the standard rotation matrices.

Starting in the terrestrial frame with the Earth-fixed vector \mathbf{r}_0 to which tidal effects $\mathbf{\Delta}$ are added, we have shown (in Secs. III.C through III.D above) how we obtain the same vector \mathbf{r}_c expressed in the geocentric celestial frame:

$$\mathbf{r}_c = \mathbf{\Omega P N U X Y}(\mathbf{r}_0 + \mathbf{\Delta}). \quad (3.143)$$

E. Earth orbital motion

We now wish to transform these station locations from a geocentric celestial reference frame moving with the Earth to a celestial reference frame which is at rest relative to the center of mass of the Solar System. The reason for this apparent complication is that the Solar System barycentric (SSB) frame is particularly useful for expressing the source positions, formulating gravitational retardation, and performing trajectory calculations of interplanetary spacecraft. These SSB station locations will then be used to calculate the geometric delay (see Sec. III.A). We will then transform the resulting time interval back to the frame in which the time delay is actually measured by the interferometer – the geocentric celestial frame moving with the Earth.

Let Σ' be a celestial geocentric frame moving with vector velocity βc relative to a frame Σ at rest relative to the Solar System center of mass. Due to the Earth's orbital motion, β is on the order 10^{-4} . Further, let $\mathbf{r}(t)$ be the position of a point (*e.g.*, station location) in space as a function of time, t , as measured in the Σ (SSB) frame. In the Σ' (geocentric) frame, there is a corresponding position $\mathbf{r}'(t')$ as a function of time, t' . We normally observe and model $\mathbf{r}'(t')$ as shown in Secs. III.C through III.D. However, in order to calculate the geometric delay in the SSB frame Σ , we will need the transformations of $\mathbf{r}(t)$ and $\mathbf{r}'(t')$, as well as of t and t' , as we shift frames of reference. Measuring positions in units of light travel time, we have from Jackson (1975) the Lorentz transformation:

$$\mathbf{r}'(t') = \mathbf{r}(t) + (\gamma - 1)[\mathbf{r}(t) \cdot \boldsymbol{\beta}]\boldsymbol{\beta}/\beta^2 - \gamma\boldsymbol{\beta}t \quad (3.144)$$

$$t' = \gamma[t - \mathbf{r}(t) \cdot \boldsymbol{\beta}], \quad (3.145)$$

and the inverse transformation:

$$\mathbf{r}(t) = \mathbf{r}'(t') + (\gamma - 1)[\mathbf{r}'(t') \cdot \boldsymbol{\beta}]\boldsymbol{\beta}/\beta^2 + \gamma\boldsymbol{\beta}t' \quad (3.146)$$

$$t = \gamma[t' + \mathbf{r}'(t') \cdot \boldsymbol{\beta}], \quad (3.147)$$

where in this section

$$\gamma = (1 - \beta^2)^{-1/2} . \quad (3.148)$$

Let t_1 represent the time measured in the SSB frame Σ , at which a wave front crosses antenna 1 at position $\mathbf{r}_1(t_1)$. Let $\mathbf{r}_2(t_1)$ be the position of antenna 2 at this same time, as measured in the SSB frame. Also, let t_2 be the time measured in this frame at which that same wave front intersects station 2. This occurs at the position $\mathbf{r}_2(t_2)$. Following Sec. III.A, Eq. (3.2) we can calculate the geometric delay $t_2 - t_1$. Transforming this time interval back to the geocentric Σ' frame, we obtain

$$t_2' - t_1' = \gamma(t_2 - t_1) - \gamma[\mathbf{r}_2(t_2) - \mathbf{r}_1(t_1)] \cdot \boldsymbol{\beta} . \quad (3.149)$$

Assume further that the motion of station 2 (with barycentric velocity $\boldsymbol{\beta}_2$) is rectilinear over this time interval. This assumption is not strictly true but, as discussed below, the resulting error is much less than 1 mm in calculated delay. Thus

$$\mathbf{r}_2(t_2) = \mathbf{r}_2(t_1) + \boldsymbol{\beta}_2(t_2 - t_1) , \quad (3.150)$$

which gives

$$\mathbf{r}_2(t_2) - \mathbf{r}_1(t_1) = \mathbf{r}_2(t_1) - \mathbf{r}_1(t_1) + \boldsymbol{\beta}_2(t_2 - t_1) \quad (3.151)$$

and

$$\begin{aligned} t_2' - t_1' &= \gamma(t_2 - t_1) - \gamma[\mathbf{r}_2(t_1) - \mathbf{r}_1(t_1)] \cdot \boldsymbol{\beta} - \gamma\boldsymbol{\beta}_2 \cdot \boldsymbol{\beta}[t_2 - t_1] \\ &= \gamma(1 - \boldsymbol{\beta}_2 \cdot \boldsymbol{\beta})(t_2 - t_1) - \gamma[\mathbf{r}_2(t_1) - \mathbf{r}_1(t_1)] \cdot \boldsymbol{\beta} . \end{aligned} \quad (3.152)$$

This is the expression for the geometric delay that would be observed in the geocentric Σ' frame in terms of the SSB geometric delay and SSB station positions.

Since our calculation starts with station locations given in the geocentric frame, it is convenient to obtain an expression for $\mathbf{r}_2(t_1) - \mathbf{r}_1(t_1)$ in terms of quantities defined in that same geocentric frame. To obtain such an expression consider two events $[\mathbf{r}'_1(t'_1), \mathbf{r}'_2(t'_1)]$ that are geometrically separate, but simultaneous, in the geocentric frame, and occurring at time t'_1 . These two events appear in the SSB frame as

$$\mathbf{r}_1(t_1) = \mathbf{r}'_1(t'_1) + (\gamma - 1)[\mathbf{r}'_1(t'_1) \cdot \boldsymbol{\beta}]\boldsymbol{\beta}/\beta^2 + \gamma\boldsymbol{\beta}t'_1 \quad (3.153)$$

and as

$$\mathbf{r}_2(t_2) = \mathbf{r}'_2(t'_1) + (\gamma - 1)[\mathbf{r}'_2(t'_1) \cdot \boldsymbol{\beta}]\boldsymbol{\beta}/\beta^2 + \gamma\boldsymbol{\beta}t'_1 , \quad (3.154)$$

where

$$t_2 - t_1 = \gamma[\mathbf{r}'_2(t'_1) - \mathbf{r}'_1(t'_1)] \cdot \boldsymbol{\beta} . \quad (3.155)$$

With these three equations and the expression

$$\mathbf{r}_2(t_2) = \mathbf{r}_2(t_1) + \boldsymbol{\beta}_2[t_2 - t_1] \quad (3.156)$$

we may obtain the vector $\mathbf{r}_2(t_1)$:

$$\begin{aligned} \mathbf{r}_2(t_1) &= \mathbf{r}'_2(t'_1) + (\gamma - 1)[\mathbf{r}'_2(t'_1) \cdot \boldsymbol{\beta}]\boldsymbol{\beta}/\beta^2 \\ &\quad + \gamma\boldsymbol{\beta}t'_1 - \gamma\boldsymbol{\beta}_2[\mathbf{r}'_2(t'_1) - \mathbf{r}'_1(t'_1)] \cdot \boldsymbol{\beta} . \end{aligned} \quad (3.157)$$

This is the position of station 2 at the time t_1 as observed in Σ . From this we obtain:

$$\begin{aligned} \mathbf{r}_2(t_1) - \mathbf{r}_1(t_1) &= \mathbf{r}'_2(t'_1) - \mathbf{r}'_1(t'_1) + (\gamma - 1)\left([\mathbf{r}'_2(t'_1) - \mathbf{r}'_1(t'_1)] \cdot \boldsymbol{\beta}\right)\boldsymbol{\beta}/\beta^2 \\ &\quad - \gamma\boldsymbol{\beta}_2[\mathbf{r}'_2(t'_1) - \mathbf{r}'_1(t'_1)] \cdot \boldsymbol{\beta} . \end{aligned} \quad (3.158)$$

As shown in Sec. III.A, the vectors $[\mathbf{r}_2(t_1) - \mathbf{r}_1(t_1)]$ and $\boldsymbol{\beta}_2$ are all that is needed to obtain $t_2 - t_1$ for the case of plane waves. For curved wave fronts we will need to know the individual station locations in the barycentric frame as well.

These we obtain from Eqs. (3.153) and (3.157) with t'_1 set equal to zero. Setting $t'_1 = 0$ is justified since the origin of time is arbitrary when calculating time differences.

In implementing these transformations, the relationship for the transformation of velocities is also needed. Taking differentials of Eqs. (3.146) and (3.147) we have:

$$d\mathbf{r} = d\mathbf{r}' + (\gamma - 1)(d\mathbf{r}' \cdot \boldsymbol{\beta})\boldsymbol{\beta}/\beta^2 + \gamma\boldsymbol{\beta}dt' , \quad (3.159)$$

$$dt = \gamma(dt' + d\mathbf{r}' \cdot \boldsymbol{\beta}) . \quad (3.160)$$

Dividing to obtain $d\mathbf{r}/dt$ we obtain for station 2 in the SSB Σ frame:

$$\boldsymbol{\beta}_2 = \left[\boldsymbol{\beta}'_2 + (\gamma - 1)(\boldsymbol{\beta}'_2 \cdot \boldsymbol{\beta})\boldsymbol{\beta}/\beta^2 + \gamma\boldsymbol{\beta} \right] / \left[\gamma(1 + \boldsymbol{\beta}'_2 \cdot \boldsymbol{\beta}) \right] . \quad (3.161)$$

All barycentric positions and velocities required for the calculations in this section are obtained from planetary ephemerides in the J2000.0 frame (Standish, 1982; Standish and Newhall, 1985).

For station 2 relative to the geocentric origin, we have from Eqs. (3.76) and (3.77):

$$\boldsymbol{\beta}'_2 \approx \boldsymbol{\Omega} \mathbf{P} \mathbf{N} \frac{d\mathbf{U}}{dH} \mathbf{X} \mathbf{Y} \mathbf{r}'_2 \omega_E , \quad (3.162)$$

where the inertial rotation rate of the Earth is

$$\omega_E = 7.292115 \times 10^{-5} \text{ radians per second.} \quad (3.163)$$

This is not a critical number since it is used only for station velocities, or to extrapolate Earth rotation forward for very small fractions of a day (*i.e.*, typically less than 1000 seconds).

The assumption of rectilinear motion can be shown to result in negligible errors. Using the plane wave front approximation of Eq. (3.2), an estimate of the error $\delta\tau$ in the calculated delay due to an error $\Delta\boldsymbol{\beta}_2$ in the above value of $\boldsymbol{\beta}_2$ is

$$\delta\tau = \hat{\mathbf{k}} \cdot [\mathbf{r}_2(t_1) - \mathbf{r}_1(t_1)] \left(\frac{1}{1 - \hat{\mathbf{k}} \cdot (\boldsymbol{\beta}_2 + \Delta\boldsymbol{\beta}_2)} - \frac{1}{1 - \hat{\mathbf{k}} \cdot \boldsymbol{\beta}_2} \right) \approx \tau \Delta\boldsymbol{\beta}_2 . \quad (3.164)$$

Further, from Eq. (3.161) above (since $\gamma \approx 1 + 10^{-8}$),

$$\Delta\boldsymbol{\beta}_2 \approx \Delta\boldsymbol{\beta}'_2 . \quad (3.165)$$

For the vector $\boldsymbol{\beta}'_2$ in a frame rotating with angular velocity ω , the error $\Delta\boldsymbol{\beta}'_2$ that accumulates in the time interval τ due to neglecting the rotation of that frame is

$$\Delta\boldsymbol{\beta}'_2 \approx \boldsymbol{\beta}'_2 \omega \tau . \quad (3.166)$$

Thus for typical Earth-fixed baselines, where $\tau \leq 0.02$ s, neglecting the curvilinear motion of station 2 due to the rotation of the Earth causes an error of $< 4 \times 10^{-14}$ s, or 0.012 mm, in the calculation of τ . Similarly, neglecting the orbital character of the Earth's motion causes a maximum error on the order of 0.0024 mm.

A related transformation from the Σ to Σ' frames that is needed for models of antenna axis offsets and atmospheric effects is an expression for the ‘‘aberrated’’ source direction unit vector $\hat{\mathbf{s}}_0$. In the SSB Σ frame, this vector is just the negative of the propagation vector of Eq. (3.3): $\hat{\mathbf{s}}_0 = -\hat{\mathbf{k}}$. The Earth's diurnal rotational contribution to aberration is two orders of magnitude smaller than that due to the Earth's orbital velocity and can be neglected for axis offset and tropospheric models. The source unit vector $\hat{\mathbf{s}}$ in the geocentric celestial frame is then given by the Lorentz transformation

$$\hat{\mathbf{s}} = a_s \hat{\mathbf{s}}_0 + a_\beta \boldsymbol{\beta} \quad (3.167)$$

with the coefficients

$$a_s = \frac{1}{\gamma(1 + \boldsymbol{\beta} \cdot \hat{\mathbf{s}}_0)} \quad \text{and} \quad a_\beta = a_s \left[(1 - \gamma) \frac{\boldsymbol{\beta} \cdot \hat{\mathbf{s}}_0}{\beta^2} + \gamma \right] . \quad (3.168)$$

Working in a frame at rest with respect to the center of mass of the Solar System causes relativistic effects due to the motion of the Solar System in the “fixed frame” of the extragalactic radio sources to be absorbed into the mean positions of the sources and their proper motions. With observational data extending over a sufficiently long time span, this motion in inertial space should be separable from terrestrial and intra-Solar-System dynamics. The known motions of the Solar System barycenter with respect to four standards are listed in Table VI. Both the magnitudes and directions are tabulated, with the latter given in terms of Galactic longitude l and latitude b . In order of increasing velocity, they are given with respect to the local standard of rest (LSR), Galactic center (GC), Local Group (LG), and cosmic microwave background (CMB). Note that the motion of the SSB relative to the CMB is on the order of $10^{-3}c$, indicating that relativity should play a significant role in modeling its consequences for VLBI. Since the extragalactic radio sources are expected to be between the LG and CMB, the motion of the Solar System relative to the “fixed” extragalactic reference frame (EGRF) is also expected to be of similar magnitude. Detection of this motion could contribute significantly to understanding of the large-scale structure of the universe.

We note at this point that the extragalactic radio sources have a median redshift $z \approx 1.2$, whereas the more distant CMB is characterized by redshift $z = 10^3$ (Melchiorri, 1990). If the extragalactic radio sources are assumed to be at rest relative to the CMB, one then has an estimate of the SSB velocity in the extragalactic radio frame. Motion of the SSB relative to the EGRF potentially contributes to the observed delays in VLBI experiments in three ways: geometric, gravitational, and aberrational effects.

Geometric effects: The geometric effects of galactic rotation can be easily estimated. In the vicinity of the Sun, the period for galactic rotation is approximately 240 million years. Thus our angular velocity about the galactic center is $\approx 2\pi/2.4 \times 10^8 = 2.6 \times 10^{-8}$ radians/year. For sources within the Galaxy, at distances approximately equal to our distance from the galactic center, the apparent positions could change by ≈ 26 nrad/yr. An intercontinental baseline (10,000 km) could thus be in error by as much as 26 cm/yr (1 nrad \approx 1 cm) if measurements were based on sources within the Galaxy. Since our distance from the galactic center is 8.5 ± 1 kpc $\approx 2.7 \times 10^4$ light years (Binney and Tremaine, 1987), and most extragalactic radio sources are believed to be $\approx 10^9$ light years distant, the potential baseline error is scaled by the ratio of these two distances, $\approx 3 \times 10^{-5}$, and becomes only ≈ 0.01 mm/year. Even with the present near-20-year history of VLBI data, the purely geometric systematic error due to galactic rotation is negligible, and only exceeds the millimeter level for sources closer than 10 million light years.

Gravitational delay effects: Gravitational delay effects depend on the relative positions of the radio source, the intervening masses, and the receiving station. Thus one must consider how the motion of the SSB changes these effects. The central bulge of the Milky Way galaxy contains $\approx 10^{11}$ solar masses and it is about 8.5 kpc ($\approx 2 \times 10^9$ AU) from the Solar System. The Galactic gravitational delay is thus estimated to be approximately 40 times larger than the solar delay. While the solar effect varies on the time scale of a year, the galactic effect varies on a time scale of 240 million years. As with the galactic aberration effects, we choose to absorb the static portion (maximum of 4 arc seconds at 10° from the GC) into the reported radio source positions. We are left to model the variation of this effect with time. Given that the SSB’s angular motion about the GC is 5 mas/yr and that scintillations from the interstellar medium limit VLBI observations at 2 to 8 GHz frequencies to no closer than 10° from the GC, the largest expected change in deflection would be $< 0.5 \mu\text{as}$ per year.

Aberration effects: The $0.0012c$ SSB–CMB velocity will cause large (≈ 4 arc min) changes in apparent source positions due to aberration. To the extent that the SSB velocity does not change on time scales of decades, however, one is free to absorb these aberration effects into reported source positions. With such a convention, the problem is reduced to considering changes in the SSB velocity.

Based on the results of studies in galactic dynamics (*e.g.* Binney and Tremaine, 1987), one may construct a model of the SSB’s acceleration both toward the Galactic Center (GC) and toward the Local Standard of Rest (LSR). At present we have not modeled the motion of the GC relative to the Local Group (LG) nor have we modeled the motion of the Local Group relative to the cosmic microwave background. This is equivalent to assuming that the GC-LG and LG-CMB velocities are constant on time scales of decades (*i.e.*, acceleration $\ll 2 \times 10^{-11}c/\text{yr}$).

SSB-LSR velocity: We consider a circular motion of radius ≈ 1 kpc with a period of ≈ 200 million years. This gives a change in velocity

$$\dot{V}_{\text{SSB-LSR}} = 2 \times 10^{-12} c/\text{yr} \quad (3.169)$$

directed toward the local standard of rest. This acceleration will cause a maximum aberration of $\approx 0.5 \mu\text{as}/\text{yr}$ which can be ignored because of its small size.

LSR-GC velocity: We consider a circular motion of radius 8.5 kpc with a period of 240 million years. This gives a change in velocity

$$\dot{V}_{\text{LSR-GC}} = 2 \times 10^{-11} c/\text{yr} \quad (3.170)$$

directed toward the Galactic center ($\alpha = 17^{\text{h}}45^{\text{m}}.5$, $\delta = -28^{\circ}56'$). This velocity will cause a maximum aberration of $\approx 5 \mu\text{s}/\text{yr}$. This aberration effect is at present not included in *a priori* VLBI models. It is, however, possible to estimate the SSB's velocity *change* from the data.

F. Source structure

By analogy with the time dependence of station coordinates caused by tectonic and tidal motion, non-stationarity of the source coordinates must also be considered. In VLBI this complication arises because any structure or motion of the radio sources is manifested in slight variations of the observed delays. Likewise, in generalization of the model to ranging experiments (interplanetary spacecraft, GPS, SLR, LLR) the “structure” of the “source” includes positions of the transmitter relative to the center of mass of the satellite, and its orbital path relative to the Earth (*i.e.*, the GPS, Lageos, or Moon ephemerides). For VLBI, such effects can be eliminated to a large extent by judicious choice of objects in planning the experiments. With the exception of special purpose experiments (such as those of Lestrade *et al.* (1995) on radio stars), the sources are well outside our Galaxy, ensuring minimal proper motion. Numerous astrophysical studies during the past two decades have shown that compact extragalactic radio sources exhibit structure on a milliarcsecond scale (*e.g.* Kellermann and Pauliny-Toth, 1981). Such studies are important for developing models of the origin of radio emission of these objects. Many radio source structures are found to be quite variable with frequency and time (Zensus and Pearson, 1987; Taylor *et al.*, 1994a; Taylor *et al.*, 1994b; Polatidis *et al.*, 1995; Thakkar *et al.*, 1995; Henstock *et al.*, 1994; Fey *et al.*, 1996). Survey maps of 187 radio sources in the Taylor *et al.* (1994a) reference showed that the structures of only 8 sources did not exceed a scale of 1 mas at an observing frequency of 5 GHz. If extragalactic sources are to serve as reference points in a reference frame that is stable at a level below 1 mas, it is important to correct for the effects of their structures in astrometric VLBI observations.

Corrections for the effects of source internal structures are based on work by Thomas (1980), Ulvestad (1988), and Charlot (1989; 1990a). A varying non-point-like distribution of the intensity of a source yields time dependent corrections to the group delay and phase delay rate observables, $\Delta\tau_s$ and $\Delta\dot{\tau}_s$, that may be written in terms of the source's intensity distribution $I(\mathbf{s}, \omega, t)$ as

$$\Delta\tau_s = \partial\phi_s/\partial\omega, \quad \Delta\dot{\tau}_s = \partial\phi_s/\partial t, \quad (3.171)$$

with

$$\phi_s = \arctan(-Z_s/Z_c) \quad (3.172)$$

and

$$Z_{\{c\}^s} = \iint d\Omega I(\mathbf{s}, \omega, t) \left\{ \frac{\sin}{\cos} \right\} (2\pi\mathbf{B} \cdot \mathbf{s}/\lambda). \quad (3.173)$$

Here ϕ_s is the correction to the phase of the incoming signal, \mathbf{s} is a vector from the adopted reference point to a point within the source intensity distribution in the plane of the sky, ω and λ are the observing frequency and wavelength, \mathbf{B} the baseline vector, and the integration is over solid angle Ω . Source intensity distribution maps are most conveniently parametrized in terms of one of two models: superpositions of Dirac delta functions or Gaussians. At a given frequency, the corresponding intensity distributions are written as

$$I(\mathbf{s}) = \sum_k S_k \delta(x - x_k, y - y_k) \quad (3.174)$$

or

$$I(\mathbf{s}) = \sum_k \frac{S_k}{2\pi a_k b_k} \exp\left(- \left[(x - x_k) \cos \theta_k + (y - y_k) \sin \theta_k \right]^2 / 2a_k^2 - \left[(x - x_k) \sin \theta_k - (y - y_k) \cos \theta_k \right]^2 / 2b_k^2 \right), \quad (3.175)$$

where S_k is the flux of component k , and \mathbf{s}_k (with components x_k, y_k in the plane of the sky) is its position relative to the reference point. For Gaussian distributions, θ_k is the angle between the major axis of component k and the u axis (to be defined below), and (a_k, b_k) are the standard deviations: full widths at half maximum of the (major, minor) axes of component k normalized by $2\sqrt{2\log 2}$. The quantities $Z_{\{c\}^s}$ entering the structure phase ϕ_s (Eq. 3.172) are

$$Z_{\{c\}} = \sum_k S_k \left\{ \begin{matrix} \sin \\ \cos \end{matrix} \right\} (2\pi \mathbf{B} \cdot \mathbf{s}_k / \lambda) \quad (3.176)$$

for delta functions, and

$$Z_{\{c\}} = \sum_k S_k \exp[-2\pi^2(a_k^2 U_k^2 + b_k^2 V_k^2)] \left\{ \begin{matrix} \sin \\ \cos \end{matrix} \right\} (2\pi \mathbf{B} \cdot \mathbf{s}_k / \lambda) \quad (3.177)$$

for Gaussians. Here

$$\begin{aligned} U_k &= u \cos \theta_k + v \sin \theta_k \\ V_k &= -u \sin \theta_k + v \cos \theta_k, \end{aligned} \quad (3.178)$$

with u and v being the projections of the baseline vector \mathbf{B} on the plane of the sky in the E-W and N-S directions, respectively.

Maps may be specified in terms of an arbitrary number of either Gaussian or delta function components. At most, six parameters characterize each component: its polar coordinates and flux, and, for a Gaussian, its major and minor axes and the position angle of the major axis. The structural correction for phase is computed via Eqs. (3.172) and either (3.176) or (3.177). For the bandwidth synthesis delay observable, the structure correction is the slope of a straight line fitted to the individual structure phases calculated for each frequency channel used during the observation. For example, for Mark III data there are typically 8 channels spanning ≈ 8.2 to 8.6 GHz at X band, and 6 channels spanning ≈ 2.2 to 2.3 GHz at S band. Delay rate structure corrections are calculated by differencing the structure phases at the two times (Eq. 2.6) used to form the theoretical rate observable. In the case of dual-band (S-X) experiments, a linear combination (Eq. 5.11) of the structure corrections calculated independently for each band is applied to the dual-frequency observables.

The practical question to be resolved is whether structural corrections based on source intensity distribution maps yield significant and detectable corrections to the observables at the present levels of experimental and modeling uncertainty. Maps are becoming available for a considerable number of the sources currently observed by VLBI (Fey *et al.*, 1996; available at <http://maia.usno.navy.mil/rorf/rrfid.html>). Some of the extended sources show time variability on a scale of months. Since the corrections $\Delta\tau_s$ and $\Delta\dot{\tau}_s$ are quite sensitive to fine details of the structure, in such cases new maps may be required on short time scales. Depending on the relative orientation of the source and VLBI baseline, the delay correction can be as large as ≈ 1 ns for extended sources, which is equivalent to tens of cm. Despite the potentially large corrections and difficulties in producing and applying maps, the prognosis appears to be good. Charlot (1990b) found that data from a multiple baseline geodynamics experiment are adequate to map source structures with high angular resolution. The use of such maps for the source 3C 273 yields structure corrections that substantially improve modeling of observable delays (Charlot, 1994). Recent work has investigated the problem of time dependent structures by interpolating the positions and strengths of the components ejected from the core of 3C 273, from maps made many months apart, and using such interpolated maps to correct observations made in the time period between the maps (Charlot and Sovers, 1998). Since maps of many sources are becoming available from imaging studies using the VLBA (Fey *et al.*, 1996), it can be expected that structure corrections will become fairly routine for numerous extended radio sources used in astrometric work.

Empirical evaluation of the effects of unknown source structure on VLBI measurements could be made via the time rates of change of the source right ascension α and declination δ , based on a time-linear model of the source coordinates

$$\begin{aligned} \alpha &= \alpha_0 + \dot{\alpha}(t - t_0) \\ \delta &= \delta_0 + \dot{\delta}(t - t_0). \end{aligned} \quad (3.179)$$

Non-zero estimates of the rate parameters $\dot{\alpha}$ and $\dot{\delta}$ could arise either from genuine proper motion or from motion of the effective source centroid sampled by VLBI measurements. Unambiguous interpretation of such results is problematic, but non-zero rates can be used as crude diagnostics for the presence of structure effects. Apparent source position rates have been reported by Ma and Shaffer (1991), Jacobs *et al.* (1993), and Eubanks *et al.* (1996). Thus far, statistically significant rates are not believed to represent true proper motion, but rather to be the consequence of a change in the interference pattern caused by spectral redistribution or ejection of components from the central engine of the source. Galactic rotation and gravitational radiation (Pyne *et al.*, 1996; Gwinn *et al.*, 1997) may also contribute to apparent motions. Apparent position shifts and proper motions may likewise result from gravitational lensing within the Galaxy (Hosokawa *et al.*, 1997).

In the absence of maps, using parameter estimation from astrometric VLBI data, source structure may also be modeled as a superposition of two δ functions centered at points $P_1(x_1, y_1)$ and $P_2(x_2, y_2)$ respectively, as in Eq. (3.174) above. The parameters describing the two components are: 1) flux ratio $K = S_2/S_1$, where S_k is the flux of the k th component, 2) component separation $s = |\mathbf{s}| = |\overrightarrow{P_1 P_2}|$, and 3) position angle θ . The position angle is $\theta = 0^\circ$ when $\overrightarrow{P_1 P_2}$ is in the direction of increasing declination $\hat{\delta}$, and $\theta = 90^\circ$ when $\overrightarrow{P_1 P_2}$ is in the direction of increasing right ascension $\hat{\alpha}$. From Charlot (1990b), the group delay has the following dependence on the structural parameters:

$$\tau = \frac{2\pi K (1 - K)}{\omega (1 + K)} \frac{R[1 - \cos(2\pi R)]}{[K^2 + 2K \cos(2\pi R) + 1]}, \quad (3.180)$$

where

$$R = \mathbf{B} \cdot \mathbf{s} / \lambda. \quad (3.181)$$

Note that this model is not linear in its three parameters. This may complicate parameter estimation in the absence of accurate *a priori* values. For evaluating partial derivatives of τ that are needed for parameter estimation, the component separation \mathbf{s} and baseline \mathbf{B} are most conveniently written in terms of their components in the celestial system, as

$$\begin{aligned} \mathbf{s} &= \hat{\alpha} s \sin \theta + \hat{\delta} s \cos \theta \\ \mathbf{B} &= \hat{\alpha} u \lambda + \hat{\delta} v \lambda. \end{aligned} \quad (3.182)$$

Then R becomes

$$R = s(u \sin \theta + v \cos \theta). \quad (3.183)$$

G. Antenna structure

The development in Secs. III.A to III.E outlines how the time delay model would be calculated for two points fixed with respect to the Earth's crust. Just as the sources are not point-like (Sec. III.F), the antenna system likewise does not necessarily behave as an Earth-fixed point. Not only are there instrumental delays in the system, but portions of the antenna move relative to the Earth. To the extent that instrumental delays are independent of the antenna orientation, they are indistinguishable to the interferometer from clock offsets (which are treated in Sec. IV). If necessary, such instrumental delays can be separated from clock properties by careful calibration of each antenna system (*e.g.* Rogers, 1975). Physical motions of each antenna relative to the Earth's surface must be considered, however, since they are part of the geometric model. Fig. 9 shows the Deep Space Network's Deep Space Station 43, which is a 70-m diameter antenna located in Tidbinbilla, Australia (near Canberra). It can easily be imagined that establishing and measuring the stability of such a large structure is not a trivial matter. For comparison, the majority of contemporary steerable antennas are 20 to 35 meters in diameter.

PICTURE OF AUSTRALIAN DSN ANTENNA
 OMITTED BECAUSE POSTSCRIPT
 UNACCEPTABLE TO LANL ARCHIVE

FIG. 9. The 70-m diameter DSN antenna near Tidbinbilla, Australia.

The model of the antenna structure is divided into several components. First, we consider the geometric delay which arises when the two axes used to steer the antenna do not intersect. This effect is then modified to account for the slight distortion by tropospheric refraction of the direction in which the antenna is pointed. Variation in ambient temperature causes thermal expansion of the structure, and the force of gravity causes deformations that vary as the antenna changes orientation. For most types of antennas there is also a subtle effect caused by the rotation of the feed horn – relative to a fixed direction on the celestial sphere – as the antenna tracks the sidereal motion of a source. A small correction to the model of the zenith troposphere delay is required for antennas with non-intersecting axes. Lastly, we discuss the modeling of ‘site vectors’ which account for experiment-to-experiment variations in the position of a mobile antenna relative to a fixed benchmark.

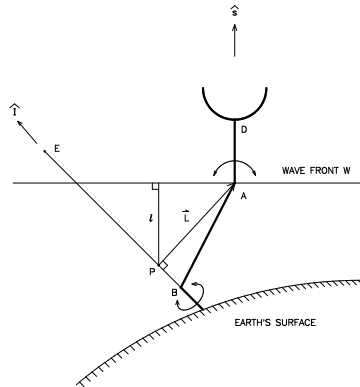


FIG. 10. Generalized schematic representation of the geometry of a steerable antenna. Two rotation axes and the “reference point” P are indicated.

Before giving the details of our model, let us describe a general antenna pointing system (shown schematically in Fig. 10) which applies to all antennas that are steerable along two coordinates. The unit vector $\hat{\mathbf{s}}$ to the aberrated source position is shown. Usually, a symmetry axis AD points parallel to $\hat{\mathbf{s}}$. The point A on the figure also represents the end view of an axis which allows rotation in the plane perpendicular to that axis. This axis is offset by some distance L from a second rotation axis BE. For many antennas this offset is zero or a few meters, but it can be as large as 15 m (for the 43-m diameter antenna at Green Bank, West Virginia). All points on this second rotation axis are fixed relative to the Earth. Consequently, any point along that axis is a candidate for the fiducial point which terminates this end of the baseline. The point we actually use is the point P. A plane containing the rotation axis A and perpendicular to BE intersects BE at the point P. This is a somewhat arbitrary choice, one of conceptual convenience.

Consider the plane W which is perpendicular to the dish symmetry axis, AD, and contains the antenna rotation axis A (perpendicular to the plane of Fig. 10). For plane wave fronts this is an isophase plane (it coincides with the wave front). For curved wave fronts, however, it deviates from an isophase surface by $\approx L^2/(2R)$, where R is the distance to the source, and L is taken as a typical antenna offset AP. For $L \approx 10$ meters, $R = R_{\text{moon}} = 60R_E \approx 3.6 \times 10^8$ m, and the curvature correction $L^2/(2R) \approx 1.4 \times 10^{-4}$ mm is totally negligible. The source has to be as close as $R = 50$ km, or $0.01R_E$, before this deviation approaches a 1 mm contribution to the delay. Consequently, for all anticipated applications of radio interferometry using high-gain radio antennas, the curvature of the wave front may be neglected in modeling the influence of antenna orientation on the time delay. Likewise, gravitational effects are sufficiently constant over a dimension L to permit the use of a single Cartesian frame over the antenna structure, to a very good approximation. Provided the instrumental delay of the antenna system is independent of the antenna orientation, the recorded signal is at a constant phase delay, independent of antenna orientation, at any point on the W plane. Since this delay is indistinguishable from a clock offset, it will be totally absorbed by that portion of our model (see Sec. IV). Any delay along the symmetry axis AD up to the position of the feed (inside the dish, along AD in the direction $\hat{\mathbf{s}}$) will likewise be absorbed into the clock model.

However, for millimeter accuracy one must consider the Earth’s orbital velocity of $\approx 10^{-4}c$ which causes Lorentz effects on the order of $10^{-4}L$. For a 10-m axis offset this amounts to 1 mm. The Lorentz effects from the Earth’s orbital velocity are accounted for by aberrating the source direction $\hat{\mathbf{s}}_0$ from the SSB frame into the geocentric celestial frame, yielding $\hat{\mathbf{s}}$ according to Eq. (3.167). Since the Earth’s diurnal rotational velocity is 100 times smaller than the orbital velocity, the diurnal Lorentz effects for a 10 m offset would be negligible (≤ 0.01 mm).

The advantage of choosing the W plane, rather than some other plane parallel to it, is that the axis A is contained in this plane, and axis A is fixed relative to the BE axis by the antenna structure. If l is the length of a line from P perpendicular to the W plane, the wave front will reach the Earth-fixed point P at a time $\tau_{ax} = l/c$ after passing through axis A. If τ_0 is the model delay for a wave front to pass between the reference points P of antennas 1 and 2, then the model for the observed delay τ should be amended as:

$$\tau = \tau_0 - (\tau_{ax_2} - \tau_{ax_1}) = \tau_0 + (l_1 - l_2)/c, \quad (3.184)$$

where the subscripts refer to antennas 1 and 2.

To calculate this “axis offset”, we follow the treatment given by Wade (1970). First define a unit vector $\hat{\mathbf{I}}$ along BE, in the sense of positive away from the Earth. For antennas with their steering axes in altazimuth, equatorial, or X-Y mounts, the direction $\hat{\mathbf{I}}$ points toward the local geodetic zenith, the celestial pole, or the local geodetic horizon, respectively. Next we define a vector \mathbf{L} from P to A, $L = |\mathbf{L}|$. Without much loss of generality in this antenna system, we assume that $\hat{\mathbf{s}}, \mathbf{L}$, and $\hat{\mathbf{I}}$ are coplanar. Then:

$$\mathbf{L} = \pm L \frac{\hat{\mathbf{I}} \times (\hat{\mathbf{s}} \times \hat{\mathbf{I}})}{|\hat{\mathbf{I}} \times (\hat{\mathbf{s}} \times \hat{\mathbf{I}})|}, \quad (3.185)$$

where the plus or minus sign is chosen to give \mathbf{L} the direction from P to A. When $\hat{\mathbf{s}}$ and \mathbf{L} are parallel or antiparallel, if the antenna comes closer to the source as L increases, the plus sign is used. Since

$$\hat{\mathbf{I}} \times (\hat{\mathbf{s}} \times \hat{\mathbf{I}}) = \hat{\mathbf{s}} - \hat{\mathbf{I}} (\hat{\mathbf{I}} \cdot \hat{\mathbf{s}}), \quad (3.186)$$

$$l = \hat{\mathbf{s}} \cdot \mathbf{L} = \pm L \sqrt{1 - (\hat{\mathbf{s}} \cdot \hat{\mathbf{I}})^2}, \quad (3.187)$$

where the sign choice above is carried through.

The vector $\hat{\mathbf{I}}$ is first defined in the terrestrial frame for a station s at geodetic latitude $\phi_{s(\text{gd})}$ and longitude λ_s . We will consider four standard mount types (Salzberg, 1967): altazimuth mounts, equatorial mounts, and X-Y mounts directed either North-South or East-West. Dropping the subscripts s and gd , for an altazimuth mount $\hat{\mathbf{I}}$ is in the direction of the local geodetic zenith:

$$\hat{\mathbf{I}} = \begin{pmatrix} \cos \phi \sin \lambda \\ \cos \phi \cos \lambda \\ \sin \phi \end{pmatrix}. \quad (3.188)$$

For an equatorial mount (also called HA-Dec), $\hat{\mathbf{I}}$ is in the direction of the celestial pole. The ± 1 is appropriate for a northern/southern hemisphere station with its polar axis pointing toward the North/South pole:

$$\hat{\mathbf{I}} = \begin{pmatrix} 0 \\ 0 \\ \pm 1 \end{pmatrix}. \quad (3.189)$$

For an X-Y mount antenna, $\hat{\mathbf{I}}$ is in the direction of the lower of the two axes (toward the local geodetic horizon), which can be either North-South or East-West depending on the particular orientation of the X-Y axes. For an X-Y mount directed North-South:

$$\hat{\mathbf{I}} = \begin{pmatrix} -\sin \phi \sin \lambda \\ \sin \phi \cos \lambda \\ \cos \phi \end{pmatrix}, \quad (3.190)$$

while for an X-Y East-West directed mount:

$$\hat{\mathbf{I}} = \begin{pmatrix} -\sin \lambda \\ \cos \lambda \\ 0 \end{pmatrix}. \quad (3.191)$$

For completeness, we mention three unique antennas that have been used in VLBI experiments, but do not fall into any of the standard categories considered above. One of these is an antenna that was extensively used by the

IRIS project of the National Oceanic and Atmospheric Administration in experiments during the 1980s. It was unique because it was an equatorial mount designed for the latitude of Washington, D.C. (ϕ_W), but was deployed at Richmond, Florida until it was destroyed in the hurricane of August 1992. The considerable latitude difference, and the axis offset of several meters, make it imperative that the antenna geometry be properly modeled. See Sovers and Jacobs (1996) for details. Two other unique antennas, in Arecibo, Puerto Rico and Nancay, France, are seldom used in astrometric and never in geodetic VLBI work. The Arecibo antenna has hardware features which make it equivalent to an altazimuth mount. The Nancay array has been treated by Ortega-Molina (1985).

Since $\hat{\mathbf{I}}$ is given in the terrestrial frame t and $\hat{\mathbf{s}}$ is in the celestial geocentric frame c , we rotate $\hat{\mathbf{I}}_t$ into the celestial frame using the matrix \mathbf{Q} given in Sec. III.D:

$$\hat{\mathbf{I}}_c = \mathbf{Q}\hat{\mathbf{I}}_t , \quad (3.192)$$

where the subscripts t and c indicate the terrestrial CIO 1903 frame and the geocentric celestial frame, respectively. With this done, one may now obtain $\hat{\mathbf{s}} \cdot \hat{\mathbf{I}}_c$ and subsequently the axis offset delay from Eq. (3.187).

Note that for “nearby” sources parallax must also be included (*i.e.*, geographically separate antennas are not pointing in the same direction). If \mathbf{R}_0 is the position of the source as seen from the center of the Earth, and \mathbf{r} is the position of a station in the same frame, then the position of the source relative to that station is

$$\mathbf{R} = \mathbf{R}_0 - \mathbf{r} \quad (3.193)$$

and in Eq. (3.187) we make the substitution

$$(\hat{\mathbf{s}} \cdot \hat{\mathbf{I}})^2 = \left[\frac{(\mathbf{R}_0 - \mathbf{r}) \cdot \hat{\mathbf{I}}}{|\mathbf{R}_0 - \mathbf{r}|} \right]^2 . \quad (3.194)$$

For an extreme antenna offset of 10 m = 10^4 mm and $|\mathbf{r}| = R_E = 6.4 \times 10^3$ km, the parallax contribution exceeds 1 mm only if the source is nearer than $\approx 6 \times 10^7$ km, or 40% of the Earth-Sun distance.

Another amendment to the antenna geometry is actually due to the atmosphere. The antenna tracks the apparent position of the source after the ray path has been refracted by an angle ΔE in the Earth’s atmosphere, rather than along the vacuum source direction vector $\hat{\mathbf{s}}$ (the aberrated source direction geocentric celestial frame). While this atmospheric refraction effect is already implicitly included in the tropospheric delay correction through the so-called mapping function (Sec. V.B), it must be explicitly accounted for in the antenna axis offset model by modifying $\hat{\mathbf{s}}$. For an extreme case of an elevation angle of 6° the deflection can be as large as 2×10^{-3} radians. Thus, for an antenna with dimension $L = 10$ meters, the component of the antenna model $\delta l \approx L\Delta E \approx 20$ mm. The Earth-fixed source direction vector $\hat{\mathbf{s}}$ is modified to take atmospheric refraction into account on the basis of the change from the vacuum elevation E to an apparent value $E + \Delta E$. In the notation of Sec. V.B, a single homogeneous spherical layer approximation yields the bending correction in terms of the dry and wet zenith troposphere delays $Z_{d,w}$, the first moment of the wet troposphere refractivity f_w , $M_w = \int_0^\infty dq f_w(q)$ (Sovers and Jacobs, 1996), the dry troposphere scale height Δ , and the Earth radius R_E :

$$\Delta E = \cos^{-1}[\cos(E + \alpha_0)/(1 + \chi_0)] - \alpha_0 , \quad (3.195)$$

where

$$\begin{aligned} \chi_0 &= (Z_d + Z_w/M_w)/\Delta , \\ \alpha_0 &= \cos^{-1}[(1 + \sigma')/(1 + \sigma)] , \\ \sigma &= \Delta/R_e , \\ \sigma' &= \left([1 + \sigma(\sigma + 2)]^{1/2} / \sin E - 1 \right) \sin^2 E . \end{aligned} \quad (3.196)$$

This formula agrees with atmospheric ray-tracing results to within 1% at 6° and $\approx 15\%$ at 1° elevation.

A further geometric effect on the antenna structure also has its origin in the environment: variations of the temperature cause vertical displacements of the antenna reference point, by analogy with the model for atmospheric loading in Sec. III.C.3.a. For large antennas, these can amount to several mm for ordinary diurnal and seasonal temperature variations of 10–20 K. If VLBI data acquired under diverse weather conditions are to be modeled

simultaneously, it may be important to account for the vertical motion of the reference point. A rudimentary model of the temperature effect assumes that the vertical displacement Δr of the antenna reference point, a distance Δh above the ground, is

$$\Delta r = \alpha(T - T_0)\Delta h , \quad (3.197)$$

where α is the coefficient of thermal expansion and T_0 is the reference temperature. The reference temperature is taken to be equal to the long-term average temperature at each station. A linear expansion coefficient of 12 ppm per kelvin is appropriate for both of the usual constituents of antenna structures, steel and concrete. The vertical motion is thus ≈ 0.42 mm/K for a 70-m antenna (assumed to have $\Delta h = 35$ m). Refinements of the simple model would have to consider details of the antenna structure, and allow for thermal lag relative to the ambient temperature (*e.g.* McGinnis, 1977; Nothnagel *et al.*, 1995), including thermal effects on the axis offsets.

Gravity loading of the flexible dish structure changes an antenna's focal length. Because the component of the gravity load along the antenna's primary axis of symmetry is proportional to $\sin E$ ($E =$ elevation angle), the changes in focal length also have sinusoidal elevation dependence (Clark and Thomsen, 1988). In some antennas the subreflector may be moved ("autofocused") to compensate for such gravity deformations and thereby maintain focus. However, this procedure does not maintain a constant signal path length through the antenna optics and thus introduces systematic errors in the antenna position derived from the measurements unless such changes in path are modeled. For example, the Deep Space Network antennas used in weekly Earth orientation measurements (Steppe *et al.*, 1994) are designed to be in focus with no subreflector compensation at $E = 45^\circ$. For these 70-m and 34-m high efficiency antennas the delays relative to nominal focus at $E = 45^\circ$ have been empirically determined to be, in mm (Jacobs and Rius, 1989; 1990):

$$\begin{aligned} \tau_{\text{sr}}(70\text{-m}) &= 77 \sin E - 54 \\ \tau_{\text{sr}}(34\text{-m}) &= 13.5 \sin E - 9.8 , \end{aligned} \quad (3.198)$$

where the coefficients are known to approximately 5%. This functional form clearly exhibits the relationship between subreflector motion and other model parameters. The elevation-dependent term biases the station vertical coordinate, while the constant term is equivalent to the clock offset. Other antennas are expected to require similar corrections with different coefficients.

One physical effect that pertains to both instrumental delays and antenna geometry is the differential feed rotation for circularly polarized receivers. This is caused by the changing orientation of the antenna feed relative to a fixed direction on the celestial sphere. The phase shift θ is zero for equatorially mounted antennas. For altazimuth mounts,

$$\tan \theta = \cos \phi \sin H / (\sin \phi \cos \delta - \cos \phi \sin \delta \cos H) , \quad (3.199)$$

with $\phi =$ station latitude, $H =$ hour angle, and $\delta =$ declination of the source. For X-Y mounts, two cases are distinguished: orientation N-S or E-W. The respective rotation angles are

$$\begin{aligned} \tan \theta &= -\sin \phi \sin H / (\cos \phi \cos \delta + \sin \phi \sin \delta \cos H) \quad (\text{N} - \text{S}) \\ \tan \theta &= \cos H / (\sin \delta \sin H) \quad (\text{E} - \text{W}). \end{aligned} \quad (3.200)$$

The effect cancels for group delay data, but can be significant for phase delay and delay rate data (up to 100 fs/s for the latter). The effect on phase delay is

$$\tau = (\theta_2 - \theta_1) / f , \quad (3.201)$$

where f is the observing frequency and θ_i the phase rotation at station i .

Another small correction, which couples atmospheric delay and antenna geometry, accounts for the effect of orientation of hour angle-declination (HA-Dec) and X-Y antennas on the tropospheric path delay. Antennas with non-zero axis offsets, whose second rotation axis (A in Fig. 10) moves vertically with changing orientation, have zenith troposphere delays that may vary by 1 to 2 mm over the range of available orientations. Equatorial and X-Y mounts fall in this class. At low elevation angles this zenith variation is magnified by the mapping function to 1-2 cm. These variations must be modeled in experiments whose accuracies are at the millimeter level (*e.g.*, short-baseline phase delay measurements). For the highest accuracy, tropospheric mapping functions that depend on altitude also need to account for variation of the altitude of the antenna reference point. Reports by Jacobs (1988; 1991) derive the corrections based on considering only the dry troposphere component, and include all terms necessary to achieve an

accuracy of a few millimeters at the lowest elevations. The correction to be added to the zenith dry tropospheric delay is

$$\delta Z_d = -Z_d(L/\Delta) \psi, \quad (3.202)$$

where L is the antenna axis offset, Δ the dry troposphere scale height (≈ 8.6 km), and ψ is an angular factor that varies with the type of mount. For equatorial mounts,

$$\psi = \cos \phi \cos H, \quad (3.203)$$

where ϕ is the geodetic latitude and H the local hour angle east of the meridian. The Richmond antenna correction has this form with the Richmond ϕ replaced by ϕ_W for Washington, and H by a pseudo-hour angle H_R , where

$$H_R = \arctan\left(\cos E \sin(\theta - \epsilon) / [\cos \phi_W \sin E - \sin \phi_W \cos E \cos(\theta + \epsilon)]\right). \quad (3.204)$$

For North-South oriented X-Y mounts,

$$\psi = \sin E / (1 - \cos^2 \theta \cos^2 E)^{1/2}, \quad (3.205)$$

where θ is the azimuth (E of N), and for East-West oriented X-Y mounts,

$$\psi = \sin E / (1 - \sin^2 \theta \cos^2 E)^{1/2}. \quad (3.206)$$

Finally, we need to consider experiments involving transportable antennas which are placed at slightly different locations each time a site is occupied. The most important part of the antenna “motion” between successive site occupations is expressed as an offset (“site vector”) between the current antenna location and some Earth-fixed benchmark. If it is desired to describe a series of such experiments in terms of a single set of site coordinates (those of the benchmark), then this offset vector must be determined as part of each observing session. It is usually expressed in local geodetic coordinates (vertical, East, and North). Models of this offset vector normally assume that the local geodetic vertical direction for the antenna is parallel to that for the benchmark (flat Earth). This implies that the changes derived for the benchmark coordinates are identical to those for the antenna coordinates. The error introduced by this assumption in a baseline adjustment is approximately $d\Delta B/R_E$, where ΔB is the baseline adjustment from its *a priori* value, d is the separation of the antenna from the benchmark, and R_E is the radius of the Earth. To keep this error smaller than 1 mm for baselines that differ from *a priori* values by ≈ 1 meter, it is sufficient for d to be < 6000 meters.

More troublesome is that an angular error $\delta\Theta$ in determining the local vertical, when using an antenna whose reference point is a distance Δh above the ground, can cause an error of $\Delta h \sin\delta\Theta \approx \Delta h \delta\Theta$ in measuring the baseline to the benchmark (Allen, 1982). Unless this error is already absorbed into the measurement of the offset vector, care must be taken in setting up the portable antenna so as to minimize $\delta\Theta$. To keep the baseline error < 1 mm for an antenna height of 10 meters, $\delta\Theta$ is required to be < 20 arcseconds. Often plumb bobs are used to locate the antenna position relative to a mark on the ground. This mark is, in turn, surveyed to the benchmark. Even the difference in geodetic vertical from the vertical defined by the plumb bob may be as large as 1 arc minute, thus causing a potential error of 3 mm for antennas of 10 meter height. Consequently, great care must be taken in these measurements, particularly if the site is to be repeatedly occupied by portable antennas.

IV. INSTRUMENTAL DELAY MODELS

The frequency standards (“clocks”) at each of the two antennas are normally independent of each other. Attempts are made to synchronize them before an experiment by conventional synchronization techniques such as GPS, but these techniques may be accurate to only $\approx 1 \mu\text{s}$ in epoch and $\approx 10^{-13}$ in rate. More importantly, clocks often exhibit “jumps” and instabilities at a level that would greatly degrade interferometer accuracy if not modeled. To account for these clock effects, an additional “delay” τ_c is included in the model delay, a delay that models the behavior of a station clock as a piecewise quadratic function of time throughout an observing session. Usually, however, only the linear portion of this model is needed. For each station this clock model is given by

$$\tau_c = \tau_{c1} + \tau_{c2}(t - t_0) + \tau_{c3}(t - t_0)^2/2. \quad (4.1)$$

In addition to the effects of the lack of synchronization of clocks between stations, there are other differential instrumental effects which may contribute to the observed delay. In general, it is adequate to model these effects as if they were “clock-like”. Note that the instrumental effects on delays measured using the multifrequency bandwidth synthesis technique (Rogers, 1970) may be different from the instrumental effects on delays obtained from phase measurements at a single frequency. This is because the bandwidth synthesis process obtains group delay from the slope of phase versus frequency [$\tau_{\text{gd}} = (\partial\phi/\partial\omega)$] across multiple frequency segments spanning the receiver passband. Thus, any frequency-independent instrumental contribution to the measured interferometer phase has no effect on the group delay determined by the bandwidth synthesis technique. However, if the delay is obtained directly from the phase measurement ϕ at a given frequency ω then the phase delay ($\tau_{\text{pd}} = \phi/\omega$) does have that instrumental contribution.

Because of this difference, it is necessary to augment the “clock” model for phase delay measurements:

$$\tau_{\text{c}_{\text{pd}}} = \tau_c + \tau_{c4}(t - t_0) + \tau_{c5}(t - t_0)^2/2, \quad (4.2)$$

where τ_c is the clock model for bandwidth synthesis observations and is defined in Eq. (4.1). Since present systems measure both bandwidth synthesis group delay and phase delay rate, all of the clock parameters described above must be used. However, in a perfectly calibrated interferometer, $\tau_{c4} = \tau_{c5} = 0$. This particular model implementation allows simultaneous use of delay rate data derived from phase delay, with group delay data derived by means of the bandwidth synthesis technique.

A refinement of the clock model may be required for dual-frequency (S/X) delays. It originates from the differential instrumental delay for S- and X-band data, which may be sizeable. For dual-frequency observables, the clock model depends on this differential instrumental delay and on the frequencies ω_S, ω_X in the individual bands as

$$\tau_{c6} \omega_X^2 / (\omega_X^2 - \omega_S^2). \quad (4.3)$$

The differential instrumental delay τ_{c6} is normally highly correlated with the usual clock offset τ_{c1} , but under some circumstances may convey additional information. For example, if the frequencies ω_S, ω_X are not exactly the same for all measurements, the τ_{c6} term will not be perfectly absorbed into the clock offset τ_{c1} .

To model the interferometer delay on a given baseline, a difference of station clock terms is formed:

$$\tau_c = \tau_c(2) - \tau_c(1). \quad (4.4)$$

Specification of a reference clock can be postponed until least-squares parameter adjustment, and is of no concern in the model description.

V. ATMOSPHERIC DELAY MODELS

During its journey from the radio source to the two Earth-based receivers, the radio wave front must pass through intergalactic, interstellar, interplanetary, and terrestrial atmospheric media. Both the neutral and charged components of these media (neutral molecules and ionized plasma, respectively) modify the propagation speed. This produces an overall delay relative to propagation in vacuum. Differential effects among the divergent paths of the two signals traversing different regions of the anisotropic medium distort the wave front, and thus contribute to differential delay in arrival times at the two Earth-based receivers. Only in the immediate vicinity of the Earth, however, do the two ray paths diverge sufficiently to cause measurable differences in arrival times. This section is concerned with models which correct the VLBI observables for such additional delays due to propagation effects. It is divided into two parts that consider contributions from charged particles and neutral molecules, respectively. In recognition of the dominant influence of the near-Earth environment, they are named “Ionosphere” and “Troposphere”.

A. Ionosphere

For a medium composed of charged particles (plasma), Spitzer (1962) gives the refractive index at frequency ν in the quasi-longitudinal approximation:

$$n = \left[1 - \left(\frac{\nu_p}{\nu} \right)^2 \left(1 \pm \frac{\nu_g}{\nu} \cos \Theta \right)^{-1} \right]^{1/2}, \quad (5.1)$$

where Θ is the angle between the magnetic field B and the direction of propagation of the wave front. The plasma frequency ν_p is

$$\nu_p = \left(\rho c^2 r_0 / \pi \right)^{1/2} \approx 8.98 \rho^{1/2} \text{ (Hz)} \quad (5.2)$$

and the electron gyrofrequency ν_g is

$$\nu_g = \frac{eB}{2\pi mc} \approx 2.80 \times 10^6 B \text{ (Hz)}. \quad (5.3)$$

Here ρ is the number density of the electrons (m^{-3}), c the speed of light, r_0 the classical electron radius, e and m the electron charge and mass, and B is measured in gauss.

Tables VII and VIII give approximate values of the plasma frequency ν_p and gyrofrequency ν_g for the three regimes along a radio signal's ray path: Earth, interplanetary, and interstellar space. The plasma parameters ρ and B represent typical conditions in these three regions, with the upper limit adopted in cases of substantial variability (Lang, 1980; Zombeck, 1990). For example, the "Earth" values are appropriate to the daytime ionosphere. For ray paths close to the Sun, however, the tabulated "interplanetary" values are several orders of magnitude too small. Intergalactic electron densities and magnetic fields are at least two orders of magnitude smaller than the tabulated interstellar values. Given the S-band ($\nu_S = 2.3$ GHz) and X-band ($\nu_X = 8.4$ GHz) frequencies typically used in geodetic and astrometric VLBI experiments, the corrections for plasma and gyrofrequency effects can be parametrized by the ratios of ν_p and ν_g to $\nu_{S,X}$ respectively. It can be seen from Table VII that there is an order-of-magnitude falloff in the plasma frequency as we proceed outward from the Earth to interplanetary and interstellar regions. Table VIII shows that electron gyrofrequency effects are a factor of 10 smaller than plasma effects near the Earth, and negligible in interplanetary and interstellar environments.

Relative to a perfect vacuum as a reference, the contribution Δ_{pd} to the VLBI phase delay τ_{pd} for a monochromatic signal traversing a medium of refractive index n is

$$\Delta_{\text{pd}} = \frac{1}{c} \int (n - 1) dl \approx -\frac{1}{2c} \int \left(\frac{\nu'_p}{\nu} \right)^2 \left[1 + \frac{1}{4} \left(\frac{\nu'_p}{\nu} \right)^2 + \frac{1}{8} \left(\frac{\nu'_p}{\nu} \right)^3 + \dots \right] dl, \quad (5.4)$$

where

$$\frac{\nu'_p}{\nu} = \left(\frac{\nu_p}{\nu} \right) \left[1 \pm \left(\frac{\nu_g}{\nu} \right) \cos \Theta \right]^{-1/2}. \quad (5.5)$$

For 8.4 GHz, we may approximate this effect to parts in $10^6 - 10^7$ by:

$$\Delta_{\text{pd}} \approx \frac{-q}{\nu^2} \left[1 \pm \left\langle \left(\frac{\nu_g}{\nu} \right) \cos \Theta \right\rangle \right]^{-1} \approx \frac{-q}{\nu^2} \left[1 - \left\langle \left(\frac{\pm \nu_g}{\nu} \right) \cos \Theta \right\rangle \right], \quad (5.6)$$

where

$$q = \frac{cr_0}{2\pi} \int \rho dl = \frac{cr_0 I_e}{2\pi} \quad (5.7)$$

and where I_e is the total number of electrons per unit area along the integrated line of sight. The angular brackets symbolize a geometrical average. If we also neglect the term $\langle \nu_g \cos \Theta \rangle / \nu$, then the expression for Δ_{pd} becomes simple and independent of the direction of travel of the wave front through the plasma:

$$\Delta_{\text{pd}} = -q/\nu^2. \quad (5.8)$$

This additional delay is negative. Thus, a phase *advance* occurs for a monochromatic signal. Since phase delay is obtained at a single frequency, observables derived from the phase delay (*e.g.*, phase delay rates) experience an increment which is negative (the observable with the medium present is smaller than it would be without the medium). In contrast, group delays measured by a technique such as bandwidth synthesis [$\tau_{\text{gd}} = (\partial\phi/\partial\omega)$] experience an additive delay which can be derived from Eq. (5.8) by differentiating $\phi = \nu\Delta_{\text{pd}}$ with respect to frequency:

$$\Delta_{\text{gd}} = q/\nu^2. \quad (5.9)$$

The group delay is of the same magnitude as the phase delay advance. For group delay measurements, the measured delay is larger with the medium present than without the medium.

The uppermost component of the Earth's atmosphere, the ionosphere, is a layer of plasma whose density peaks at about 350 km altitude, but is widely distributed between 80 and 1000 km above the Earth's surface. It is created primarily by the ultraviolet portion of the sunlight and the solar wind, and is a superposition of three Chapman layers (Bassiri and Hajj, 1993): E, F₁, and F₂, with height parameters of 110, 210, and 350 km, respectively. During daytime in a year near the maximum of the 11-year solar activity cycle the electron density peaks in the F₂ layer at about 3.7×10^{12} electrons/m³. For a typical ionosphere, $\Delta_{\text{gd}} \approx 0.1$ to 2 ns at local zenith for $\nu = 8.4$ GHz. This effect has a maximum at approximately 1400 hours local time and a broad minimum during local night. For long baselines, the effects at each station can be quite different. Thus, the differential effect may be of the same order as the maximum.

For the interplanetary medium at an observing frequency of 8.4 GHz and assuming that the ionized region extends over 10^7 km, a single ray path experiences a delay of approximately 6×10^{-7} s in traversing the Solar System. However, the differential delay between the ray paths to the two stations on the Earth is considerably smaller, since the gradient between the two ray paths should also be inversely proportional to the dimensions of the plasma region (*i.e.*, millions as opposed to a few thousand kilometers). An interstellar signal from a source at a distance of 1 megaparsec (3×10^{19} km) would experience an integrated plasma delay of approximately 600 seconds at a frequency of 8.4 GHz if the plasma density were that of Table VII everywhere along the ray path. In the near vacuum of intergalactic space, the average plasma density is ≈ 2 orders of magnitude lower than this, reducing the delay to ≈ 10 s. In this case, however, the typical dimension is also that much greater, and so the differential effect on two ray paths separated by one Earth radius is still not as large as the differential delay caused by the Earth's ionosphere.

Plasma effects can best be calibrated by the technique of observing the sources at two frequencies, ν_1 and ν_2 , where $\nu_{1,2} \gg \nu_p$ and where $|\nu_2 - \nu_1|/(\nu_2 + \nu_1) \approx 1$. For the VLBI delays τ at the two frequencies ν_1 and ν_2 we obtain

$$\tau_{\nu 1} = \tau + q/\nu_1^2 \quad \text{and} \quad \tau_{\nu 2} = \tau + q/\nu_2^2 . \quad (5.10)$$

Multiplying each expression by the square of the frequency involved and subtracting,

$$\tau = a \tau_{\nu 2} + b \tau_{\nu 1} , \quad (5.11)$$

where $a = \nu_2^2/(\nu_2^2 - \nu_1^2)$ and $b = -\nu_1^2/(\nu_2^2 - \nu_1^2)$. This linear combination of the observables at two frequencies thus removes the charged particle contribution to the delay. For uncorrelated errors in the frequency windows, the overall error in the derived delay can be modeled as

$$\sigma_\tau^2 = a^2 \sigma_{\tau_{\nu 2}}^2 + b^2 \sigma_{\tau_{\nu 1}}^2 . \quad (5.12)$$

Modeling of other error types is more difficult and will not be treated here. Since the values of a and b are independent of q , these same coefficients apply both to group delay and to phase delay.

If we had not neglected the effect of the electron gyrofrequency in the ionosphere, then instead of Eq. (5.11) above, the combined S/X delay would have been

$$\tau = a\tau_{\nu 2} + b\tau_{\nu 1} + q \langle \nu_g \cos \Theta \rangle / [\nu_2 \nu_1 (\nu_2 - \nu_1)] , \quad (5.13)$$

where a and b are defined as in Eq. (5.11). If the third term on the right-hand side is expressed in units of the contribution of the ionosphere at frequency ν_2 , we obtain

$$\tau = a\tau_{\nu 2} + b\tau_{\nu 1} + \Delta_{\text{pd}} \nu_2 \langle \nu_g \cos \Theta \rangle / [\nu_1 (\nu_2 + \nu_1)] . \quad (5.14)$$

For X band $\Delta_{\text{pd}} \approx 0.1$ to 2 ns at the zenith. When using S band as the other frequency in the pair, this third term is $\approx 2 \times 10^{-4} \Delta_{\text{pd}} \cos \Theta \approx 0.02$ to 0.4 ps at zenith. In the worst case of high ionospheric electron content, and at low elevation angles, this effect could reach 1 mm of total error in determining the total delay using the simple formula of Eq. (5.11) above. Notice that the effect becomes much more significant at lower frequencies. Bassiri and Hajj (1993) present a more detailed discussion of higher order ionospheric effects.

To avoid the complications of modeling the ionosphere, most contemporary VLBI experiments are performed at two frequencies. The dual-frequency calibration outlined above then permits us to consider the ionosphere problem to be solved at currently required accuracy levels, and to ignore ionospheric propagation effects in modeling. For completeness, we present a model of ionospheric delay that can be used for single-frequency experiments. In these cases, the interferometer model must use whatever measurements of the total electron content are available. The

model is very simple: the ionosphere is modeled as a spherical shell whose lower boundary is at the height h_1 above the geodetic surface of the Earth, and the upper boundary is at the height h_2 above that same surface (see Fig. 11). For each station the ionospheric delay assumed to be

$$\tau_1 = kgI_e S(E)/\nu^2 , \quad (5.15)$$

where

$$k = 0.1cr_0/2\pi . \quad (5.16)$$

I_e is the total electron content at zenith (in electrons per meter squared $\times 10^{-17}$), and $g = 1(-1)$ for group (phase) delay. E is the apparent geodetic elevation angle of the source, $S(E)$ is a slant range factor discussed below, and ν is the observing frequency in gigahertz.

The slant range factor (see Fig. 11) is

$$S(E) = \left(\sqrt{R^2 \sin^2 E + 2Rh_2 + h_2^2} - \sqrt{R^2 \sin^2 E + 2Rh_1 + h_1^2} \right) / (h_2 - h_1) , \quad (5.17)$$

which is strictly correct for a spherical Earth of radius R , and a source at apparent elevation angle E . The model uses this expression, with the local radius of curvature of the geoid surface at the receiving station R taken to be equal to the distance from the station to the center of the Earth. The model also assumes this same value of R can be used at the ionospheric penetration points, *i.e.*,

$$R_i = R + h_i . \quad (5.18)$$

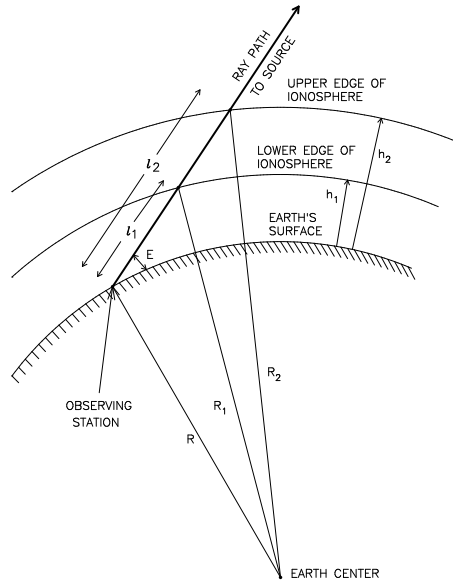


FIG. 11. Geometry of the spherical ionospheric shell used for ionospheric corrections. The slant range through the shell is $l_2 - l_1$ at elevation angle E .

This is not strictly true, but is a very close approximation, especially in view of the relatively crude nature of the total electron content determinations on which the model also depends. The total ionospheric contribution on a given baseline is

$$\tau_1 = \tau_1(2) - \tau_1(1) , \quad (5.19)$$

where the arguments 1 and 2 identify the stations. The ionospheric total electron content I_e is obtained by some external set of measurements such as Faraday rotation or GPS techniques. Such external measurements, in general, are not along directions in the ionosphere coincident with the ray paths to the interferometer. Thus, for each antenna,

it is necessary to map a measurement made along one ray path to the ray paths used by the interferometer. Many different techniques to do this mapping have been suggested and tried; Wilson *et al.* (1995) discuss recent progress.

The deficiencies of these ionosphere models for single-frequency observations are compounded by the lens effect of the solar plasma. In effect, the Solar System is a spherical plasma lens which causes the apparent positions of the radio sources to be shifted from their actual positions by an amount which depends on the solar weather and on the Sun-Earth-source angle. Since both the solar weather and the Sun-Earth-source angle change throughout the year, very accurate single-frequency observations over the time scale of a year are virtually impossible unless simultaneous auxiliary experiments are performed.

B. Troposphere

The lower few tens of kilometers of the Earth's atmosphere are known as the troposphere. In contrast to the ionosphere, this layer is to a good approximation electrically neutral (Houghton, 1986). Radio signals passing through the troposphere experience delay, bending, and attenuation relative to an equivalent path through a vacuum, because the index of refraction is not equal to the vacuum value. The additional delay is ≈ 2 m at zenith and increases to ≈ 20 m at 6° above the horizon; bending amounts to $\approx 0.1^\circ$ at elevations 6° above the horizon. This makes it imperative for accurate VLBI models to account for tropospheric delay. We review the refractivity of the moist air composing the troposphere, discuss mapping functions which model the integrated path length through the troposphere, and finally consider the limitations to the mapping function models due to azimuthal asymmetry and turbulence in the water vapor distribution.

Permanent and induced dipole moments of the molecular species present in the atmosphere modify its index of refraction and thus delay the passage of radiation at microwave frequencies. The excess path delay caused by the troposphere relative to a vacuum is

$$\tau_{\text{tr}} = \int_S (n - 1) dS, \quad (5.20)$$

where n is the index of refraction and S represents the signal's path through the troposphere. Since departures of n from unity are small, normally the "refractivity" $N = 10^6(n - 1)$ is used instead of the index of refraction. Detailed discussions of the refractivity of moist air are found in Thompson, Moran and Swenson (1986, Chap. 13), Bean and Dutton (1966), or Thayer (1974). To summarize these reviews, the refractivity of moist air at microwave frequencies depends on the permanent and induced dipole moments of the molecular species present in the atmosphere. The principal species, nitrogen and oxygen, have no permanent dipole moments, and contribute only via their induced moments. On the other hand, water vapor does have a substantial dipole moment. Induced and permanent dipole moments contribute to the refractivity as $\propto p/T$ and $\propto p/T^2$, respectively (Debye, 1929), where p and T are the pressure and temperature of the species under consideration. This is the basis of the Smith-Weintraub equation (Smith and Weintraub, 1953):

$$N = 77.6 \frac{p_D}{T} + 64.8 \frac{p_V}{T} + 3.776 \times 10^5 \frac{p_V}{T^2}, \quad (5.21)$$

where p_D and p_V are the partial pressures of "dry" air and water vapor in units of millibars. The coefficients are taken from Thayer (1974). The first term represents the aggregate induced dipole refractivity from all the dry constituents, and the second and third terms the induced dipole and permanent dipole refractivity from water vapor, respectively. Thus the troposphere problem becomes a matter of modeling pressure and temperature (p_D , p_V , T) along the ray path. Typically this problem is simplified by assuming the troposphere to be a mixture of perfect gases with unit compressibilities which are nearly in hydrostatic equilibrium. Parenthetically, as noted by Thompson, Moran and Swenson (1986), at visible wavelengths water vapor has a smaller influence on refractivity, so that the third term is not needed to model optical refractivity. This simplifies troposphere modeling for laser techniques.

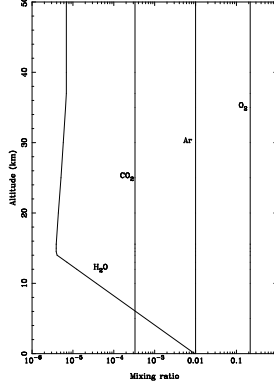


FIG. 12. Mixing ratios of four major constituents of the Earth’s atmosphere *vs.* altitude (based on Goody and Yung, 1989).

One of the biggest obstacles to modeling the tropospheric delay is the non-uniform and highly variable distribution of water vapor. In contrast to the smooth exponential decrease of N_2 and O_2 concentrations with altitude, the H_2O concentration generally decreases more rapidly within 1-2 km of the surface, and normally becomes negligible above ≈ 5 km altitude (Arya, 1988; AGU, 1995). Figure 12 shows the altitude dependence of the mixing ratios of four major atmospheric constituents. The fractions of O_2 , Ar, and CO_2 are seen to remain nearly perfectly constant from the surface up to 50 km, while the water vapor fraction falls by over 3 orders of magnitude up to the tropopause altitude (≈ 15 km) before leveling off at 7 ppm. Water vapor content can also easily vary by 50% during the few hours around sunrise and sunset. Weather changes have more pronounced effects on the wet than on the dry troposphere. The nitrogen and oxygen concentrations essentially scale with pressure while water vapor undergoes much larger concentration changes and redistribution with changing weather.

The next step in generating the troposphere model is to obtain the integrated refractivity for a signal propagating from the zenith. The dry portion, primarily oxygen and nitrogen, is very nearly in hydrostatic equilibrium. As a result the zenith delay does not depend on the details of p_D and T along the signal path. The delay can be quite accurately estimated simply by measuring the barometric pressure at the surface. The dry zenith delay Z_d (m) is related to the total surface pressure p (mbar) as

$$Z_d = 2.2768 \times 10^{-3} p / (1 - 0.00266 \cos 2\phi - 0.00028h) , \quad (5.22)$$

where the factor in the denominator corrects for a non-spherical Earth (Saastamoinen, 1972), ϕ is the station latitude, and h is the station altitude in km (see Eq. 3.69). Davis *et al.* (1985) discuss the reason for using the total surface pressure p instead of the dry partial pressure p_D . They also explain the related and subtle distinction between ‘dry’ and ‘hydrostatic’ delay, which has been glossed over in the present discussion. Typically, at sea level in the local zenith direction, the additional dry (or hydrostatic) delay that the incoming signal experiences due to the troposphere is ≈ 7.7 nanoseconds or 2.3 meters.

At each station i the delay experienced by the incoming signal due to the troposphere can most simply be modeled using a spherical-shell troposphere consisting of wet and dry components τ_{wi} and τ_{di} :

$$\tau_{tr}(i) = \tau_{wi} + \tau_{di} . \quad (5.23)$$

The total troposphere delay model for a given baseline is then:

$$\tau_{tr} = \tau_{tr}(2) - \tau_{tr}(1) . \quad (5.24)$$

If E_i is the unrefracted geodetic elevation angle of the observed source at station i , we have (dropping the subscript i):

$$\tau_{tr}(E) = \mathcal{M}_d(E)Z_d + \mathcal{M}_w(E)Z_w , \quad (5.25)$$

where $Z_{d,w}$ is the additional (dry, wet) delay at local zenith due to the presence of the troposphere, and \mathcal{M} are the so-called “mapping functions” which relate delays at an arbitrary elevation angle E to the zenith delays. Note that since E is the unrefracted elevation angle, refraction effects are contained within the mapping functions $\mathcal{M}_{d,w}$. These will be considered in some detail below.

For some geodetic experiments, the observed delay can be accurately calibrated for the total tropospheric delays at the two stations, which are in turn calculated on the basis of surface pressure measurements for the dry component, and water-vapor radiometer (WVR) measurements for the wet component. At a fixed location, the dry zenith delay (m) is related to the surface pressure p (mbar) via Eq. (5.22). The wet zenith delay Z_w can be inferred from WVR measurements performed in the vicinity of the VLBI stations at the time of the experiment. These corrections can be removed and replaced by an alternate model if desired. In the absence of such external calibrations, it was found that estimating the zenith delay as a linear function of time can improve troposphere modeling considerably. The dry and wet zenith parameters are written as

$$Z_{d,w} = Z_{d,w}^0 + \dot{Z}_{d,w}(t - t_0) , \quad (5.26)$$

where t_0 is a reference time. The time rates of change $\dot{Z}_{d,w}$ may then be estimated from fits to the data.

1. Mapping functions

The term “mapping function” is used to describe the relation between the tropospheric delay at zenith and an arbitrary angle E above the horizon. Throughout the history of VLBI, extensive attention has been paid to tropospheric mapping functions, in view of the dominance of tropospheric delay mismodeling in the error budget. The simplest way to relate the tropospheric delay for an oblique path to the delay for a signal received from directly overhead is to assume a flat Earth covered by an azimuthally symmetric troposphere layer. Since the delay is proportional to the path length through this layer, the mapping function is then simply equal to the cosecant of the elevation angle: $\mathcal{M}(E) = 1/\sin E$. Even in the early days of VLBI it was found that this approximation was inadequate, and Marini (1972) considered corrections accounting for the Earth’s curvature. This led to a mapping function in the form of a continued fraction,

$$\mathcal{M} = \frac{1}{\sin E + \frac{a}{\sin E + \frac{b}{\sin E + c}}} . \quad (5.27)$$

The simplest function, which was widely used in early VLBI modeling in the 1970s and early 1980s, was obtained by C. C. Chao (1974). It truncates Marini’s continued fraction and replaces the second $\sin E$ by $\tan E$ in order to force $\mathcal{M} = 1$ at zenith:

$$\mathcal{M}_{d,w} = \frac{1}{\sin E + \frac{A_{d,w}}{\tan E + B_{d,w}}} . \quad (5.28)$$

The dry and wet coefficients were determined from empirical fits to ray tracing results through measured average atmospheres: $A_d = 0.00143$, $B_d = 0.0445$, $A_w = 0.00035$, and $B_w = 0.017$. It was claimed to be accurate at the level of 1% at $E = 6^\circ$, and to become rapidly more accurate as zenith is approached.

As more accurate measurements in the 1980s demanded more accurate troposphere modeling, numerous improved mapping functions were developed. Many of these have mathematical forms that are slight variants of Marini’s continued fraction, and contain constants derived from analytic fits to ray-tracing results either for standard atmospheres or for observed atmospheric profiles based on radiosonde measurements. The functions of Davis *et al.* (1985), Ifadis (1986), Herring (1992), and Niell (1996) (NMF, Niell Mapping Function) fall into this category. Most of them contain parameters that are to be determined from surface meteorological measurements. The NMF function is unique in that it attempts to represent global weather variations analytically as a function of location and time of year, and contains no adjustable parameters. The NMF mapping functions provide an excellent model for situations in which data are not available to supply optimum parameters for some of the alternative mappings. Their seasonal, latitude, and altitude variations are based on interpolations of the U. S. standard atmospheres of Cole *et al.* (1965). Niell presents evidence that short term (hours to days) surface temperature variations are unimportant compared to the seasonal, latitude, and altitude variations of the temperature in the region from a few km up to the tropopause. Another tropospheric mapping function, due to Lanyi (1984) is unique in that it does not fully separate the dry and wet components and thus attempts to give a more faithful representation of the physical effects. It also contains the

most complete set of atmospheric parameters, and we will therefore present some details for this function. Several reviews have recently evaluated the multitude of tropospheric mapping functions that are now available: Gallini (1994), Mendes and Langley (1994), and Estefan and Sovers (1994).

Because of its potential to provide the most complete description of the tropospheric delay, including use of *in situ* temperature profile data, we will give some details of the Lanyi mapping function. Motivation for and details of its development were given by Lanyi (1984). It is based on an ideal model atmosphere whose temperature is constant from the surface to the top of the inversion layer h_1 , then decreases linearly with height at a rate W (lapse rate) from h_1 to the tropopause height h_2 , and is constant again above h_2 . Lanyi’s approach was to develop a semi-analytic approximation to the ray trace integral (5.20) which retains explicit temperature *vs.* altitude profile parameters that can be supplied from meteorological measurements. The goal was to provide an accurate approximation to ray tracing in a form that was less computationally intensive than performing a full numerical ray trace for every observation. The mapping function is expanded as a second order polynomial in Z_d and Z_w (plus the largest third order term). Unlike all the other functions mentioned above, the Lanyi mapping function is nonlinear in Z_d , Z_w . It differs from other mapping functions in the sense that it does not conform to the linear expression (5.25). In particular, we note that there is a $Z_d Z_w$ cross term which couples the dry and wet delays. This nonlinear term is present because for a given dry (wet) zenith delay the geometric path through the atmosphere is not independent of the amount of wet (dry) zenith delay. Hence the coefficients of the nonlinear terms have a subscript “*b*” to indicate that these terms arise from the *bending* of the signal path through the atmosphere.

Here we give only a brief summary of the functional form. The tropospheric delay is written as:

$$\tau_{\text{tr}} = F(E) / \sin E , \quad (5.29)$$

in order to factor out the $1/\sin E$ “flat Earth” model, where

$$F(E) = F_d(E)Z_d + F_w(E)Z_w + \left[F_{b1}(E)Z_d^2 + 2F_{b2}(E)Z_d Z_w + F_{b3}(E)Z_w^2 \right] / \Delta + F_{b4}(E)Z_d^3 / \Delta^2 . \quad (5.30)$$

The quantities Z_d and Z_w are the zenith dry and wet tropospheric delays, while Δ is the dry atmospheric scale height, $\Delta = kT_0/mg_c$, k = Boltzmann’s constant, T_0 = daily average surface temperature, m = mean molecular mass of dry air, and g_c = gravitational acceleration at the center of gravity of the air column. With the standard values of k , m , $g_c = 978.37 \text{ cm/s}^2$, and an average mid-latitude temperature $T_0 = 292 \text{ K}$, the scale height $\Delta = 8.6 \text{ km}$. The dry, wet, and bending contributions to the delay, $F_d(E)$, $F_w(E)$, and $F_{b1,b2,b3,b4}(E)$, are expressed in terms of moments of the refractivity. The latter are evaluated for the ideal model atmosphere and thus give the dependence of the tropospheric delay on the four model parameters T_0 , W , h_1 , and h_2 . Note that Lanyi’s formulation (Eq. 5.30) differs from the simple model (Eq. 5.25) in the presence of the “bending” terms F_{b1-4} . These account for the influence of the dry and wet constituents in bending the incoming ray path.

Four meteorological parameters describe the temperature *vs.* altitude profile in the Lanyi model. These have already been mentioned above: the surface temperature T_0 , temperature lapse rate W , inversion and tropopause altitudes h_1 and h_2 . Table IX summarizes their standard values, and also gives the approximate sensitivities of the tropospheric delay to the meteorological parameters. These values are calculated at 6° elevation, which is the approximate lower limit of validity of the Lanyi model. At this elevation, the ray path traverses the equivalent of approximately 10 “air masses”. A fifth parameter, the surface pressure p_0 , may be used to calibrate the dry zenith delay via Eq. (5.22). The full potential of the Lanyi function can only be realized if complete meteorological information is available for the time and place of a VLBI experiment. When interpolated standard global values (*e.g.* Cole *et al.*, 1965) are used for the four parameters, it is essentially equivalent to the NMF mapping.

While an exceptional amount of research has been devoted to improvement of tropospheric mapping functions during the past two decades, it is nevertheless becoming obvious that present measurement accuracy also demands characterization of azimuthal asymmetry and short-term weather variations. This may be achievable via real-time auxiliary measurements (such as WVRs), or statistical models of temporal and spatial correlations.

2. Limitations of mapping

In recent years the limitations of the mapping function have become apparent in VLBI observations. Winds at high altitudes, unusually strong lee waves behind mountains (*e.g.*, Owens Valley, California), and very high pressure gradients may all limit the accuracy of an azimuthally symmetric dry troposphere model based on measurements

of surface barometric pressure. Rough estimates indicate that, except in such unusual cases, errors in the simple model cause sub-centimeter errors in the baseline. The accuracy in more typical situations is expected to be limited by horizontal refractivity gradients caused by equator-to-pole (North-South) gradients in temperature, pressure, and humidity. These gradients were first accounted for in analyses of satellite laser ranging experiments by Gardner (1976; 1977). East-West gradients caused by motion of weather systems passing over a site may also contribute to the breakdown of the simplified mapping function model. The limits of validity of the azimuthal symmetry assumption in VLBI analysis are starting to be investigated (MacMillan, 1995; MacMillan and Ma, 1997; Chen and Herring, 1997).

While the limitations of dry mapping are small and in the case of North-South gradients may be modelable, the wet component of the atmosphere (both water vapor and condensed water in the form of clouds) is not so easily modeled. It is known to be highly variable in time and space (Fleagle and Businger, 1980). The experimental evidence (Resch, 1984) is that it is “clumpy”, and not azimuthally symmetric about the local vertical at a level which can cause many centimeters of error in a baseline measurement. Furthermore, because of incomplete mixing, surface measurements are inadequate in estimating this contribution which even at zenith can reach 20 or 30 cm. Ideally, this portion of the tropospheric delay should be determined experimentally at each site at the time of the VLBI measurements. Often the interferometer data themselves are used to quantify the effect of the water vapor as part of the parameter estimation process.

Independent quantitative estimates of the amount of water vapor along a path through the atmosphere can be made by employing “water vapor radiometers” (WVR). These instruments measure the intensity of thermal emission due to transitions between rotational energy levels of the water molecule at microwave frequencies (Elgered, 1993). They are steerable in both elevation and azimuth, have half-power beam widths of $6^\circ - 9^\circ$, and measure sky brightness temperatures at several frequencies near 22 and 31 GHz. While there is not a unique correspondence between the sky brightness temperature and water vapor content, current data retrieval procedures appear to be capable of accuracies as good as several mm of path delay (Keihm and Marsh, 1996). Recent measurements along the lines of sight of VLBI observations (Linfield *et al.*, 1996; Teitelbaum *et al.*, 1996) have yielded wet troposphere delays that agree with VLBI parameter estimates on the level of a few mm, and give a threefold reduction in residuals. Similar results have been obtained by Elgered *et al.* (1991). Despite optimism in the early years of WVR development, such calibrations have not been routinely available for the bulk of VLBI data collected during the past two decades. Because state-of-the-art WVR measurements have not been routinely available, VLBI analyses should at the minimum model the neutral atmosphere at each station as a two-component effect, with each component being an azimuthally symmetric function of the local geodetic elevation angle.

In an effort to properly account for unmodeled wet troposphere errors, a model of the spatial and temporal spectrum of wet troposphere refractivity fluctuations was developed by Treuhaft and Lanyi (1987). This Treuhaft-Lanyi model assumes that tropospheric delay errors are dominated by fluctuations in the distribution of water vapor. Furthermore, the model assumes that these fluctuations are well described by a Kolmogorov spatial distribution (*e.g.* Tatarski, 1961) that occurs in the bottom 1-2 km of the troposphere and is carried over the site by a constant wind on the order of 10 m/s. It introduces realistic variations of the troposphere with both time and geometry through this “frozen flow” assumption. The model is parametrized in terms of a “rockiness” coefficient, wind direction and speed, and the height of the turbulent layer.

The Treuhaft-Lanyi model is used to generate an *a priori* observable covariance matrix which is then included in the least squares parameter estimation procedure. It provides estimates of correlations of the tropospheric delays observed in different parts of the sky at different times. Correlations between phase rate observables are ignored. Linfield (1995) demonstrates that they typically do not exceed 10%, and decay to much smaller values on time scales of a few minutes. By accounting for spatial variations and not just temporal variations, the Treuhaft-Lanyi technique differs from filters which parametrize the troposphere as a stochastic time-varying parameter (Herring *et al.*, 1990). Lack of knowledge of the parameters required by the covariance model presently limits its potential for improving VLBI parameter estimates. Some of these parameters, which characterize the strength, extent, and direction of the turbulent flow, are starting to be quantified (Naudet, 1995). An important benefit of this technique is that data strength is not used to estimate frequent troposphere parameters in cases where the latter are not of primary interest. Thus the variances of the estimates of some important parameters (*e.g.*, baselines, source positions) are smaller than would otherwise be obtained. This benefit is in addition to the reduction of systematic parameter biases relative to estimates which use an inferior observation covariance (data weights).

VI. APPLICATIONS AND RESULTS

The model of VLBI observables which was developed in Secs. III–V has been used, with slight variations, by a number of research groups to analyze geodetic and astrometric experiments performed with various networks during the past two decades (*e.g.* Kondo *et al.*, 1992; Ma *et al.*, 1992; Sovers *et al.*, 1993; NEOS, 1994; Johnston *et al.*, 1995). The differences among groups generally involve minor variations in tropospheric and tidal modeling. Such analyses have presently reached an approximate accuracy level of 1 cm on intercontinental baselines (1 ppb). In this section we highlight some of the new insights into a wide variety of geophysics that have resulted from VLBI measurements. We intentionally exclude discussion of literature concerning internal structures of extragalactic radio sources and the associated astrophysical processes, since it is sufficiently extensive to merit a separate review. Thus, we again focus on the accomplishments of purely astrometric and geodetic VLBI. Some of these have already been introduced in the sections on model description. We will divide the applications of VLBI into three major categories: reference frames (both celestial and terrestrial), structure and dynamics of the Earth, and the orientation of the Earth in the quasi-inertial celestial frame of reference. Additional information can be extracted that relates to the Earth’s atmosphere, relativistic bending, and rudimentary details of source structure. In the near future, data that have accumulated over nearly two decades are also expected to permit quantification of the Earth’s long-term motion in inertial space (galactic rotation). Earlier in this decade, Robertson (1991) presented a survey of VLBI applications that we attempt to update here with our brief overview. More detailed reviews, including presentation of recent experiments, analyses, and results can be found in Volumes 24 and 25 of Smith and Turcotte (1993), which report the achievements of NASA’s Crustal Dynamics Project. A general introduction of the applications of many of the new space techniques, including radio interferometry, is provided by the book of Lambeck (1988). Much of the astrometric/geodetic data that have been accumulated since the 1970s are publicly available from the Crustal Dynamics Data Information System at Goddard Space Flight Center. This repository includes both raw data and selected results of analyses, and is accessible by computer at <http://cddisa.gsfc.nasa.gov/cddis.html>.

A. Reference frames

The accomplishment of VLBI that is of greatest significance is the establishment of reference frames which allow quantitative treatment of the dynamics of the Earth and Solar System at unprecedented levels of accuracy. There are two such reference systems: celestial and terrestrial. The remainder of this section summarizes determination and applications of these two fundamental reference frames, their hundred-fold accuracy improvement since the inception of VLBI and related methods, and problems of stability related to these new accuracy levels.

Astronomical objects have been used for millenia to construct celestial reference systems for measuring the passage of time, for navigation, and for investigating Solar System dynamics. To review some of the important milestones in the development of celestial reference frames: early astronomers measured the motions of the planets (*lit.* “wandering stars”) against the background of “fixed” stars. With improved observational precision, motions of these fixed stars became evident. Hipparchus is credited with recognizing precession circa 129 B.C. Proper motions of individual stars were observed in 1718 by Halley. Nutation of the Earth was discovered by Bradley in 1748. As observing precision continued to improve, Herschel and Laplace suggested using extremely distant objects to define astrometric reference frames. Such objects reduce or eliminate the effects of the proper motions on reference frame definition. The 1781 catalog of Messier (Robinson and Muirden, 1979), and the New General Catalog of Dreyer (1888) were important steps in identifying these more distant objects. The work of Leavitt (1912) and Hubble (1929) helped to establish the extreme distance of what are now classified as extragalactic objects. Present-day Earth-based optical measurements have culminated in the latest “fundamental catalog” FK5 (Fricke *et al.*, 1988), and the recent Hipparcos measurements from Earth orbit (ESA, 1997) have inaugurated a new era for optical catalogs.

The historical celestial reference frame, based on measurements at optical wavelengths, has been the unifying backdrop for centuries-long astronomical observations. It is a coordinate system whose origin is located at the barycenter of the Solar System, and which is used to establish locations of objects within the Solar System and beyond. Its present accuracy level in the FK5 realization is on the order of 0.1 arcsecond (Fricke *et al.*, 1988). Extension of observations into the microwave spectral region by early VLBI measurements already improved this accuracy by an order of magnitude. By the late 1990s, yet another order-of-magnitude improvement has brought it to 1 mas or better. Unfortunately there are very few objects emitting sufficient flux density to be observable at both optical and radio wavelengths. Thus special techniques must be employed in order to connect the VLBI celestial reference frame to the historical optical frame (Lestrade *et al.*, 1995).

Early determinations of the positions of extragalactic radio sources by Wade (1970) and Cohen and Shaffer (1971) yielded angular coordinates accurate at approximately the 1 arcsecond level. Within five years, this accuracy was improved by more than an order of magnitude (Wade and Johnston, 1977), and started to rival the best optical determinations. Improvement by approximately another two orders of magnitude has been achieved during the past two decades for several hundred radio sources. Launch of the astrometric satellite Hipparcos in 1989 (Kovalevsky *et al.*, 1995) has likewise extended the accuracy of optical positions of $\approx 10^5$ sources to the milliarcsecond level. Since the median optical apparent magnitude of the radio sources is ≈ 18 (well beyond Hipparcos sensitivity), a direct tie to the radio reference frame is not possible. A few optical sources (radio stars) also emit weakly at radio frequencies. These can be observed in both the optical and radio regions in order to relate the two reference frames (Lestrade *et al.*, 1995).

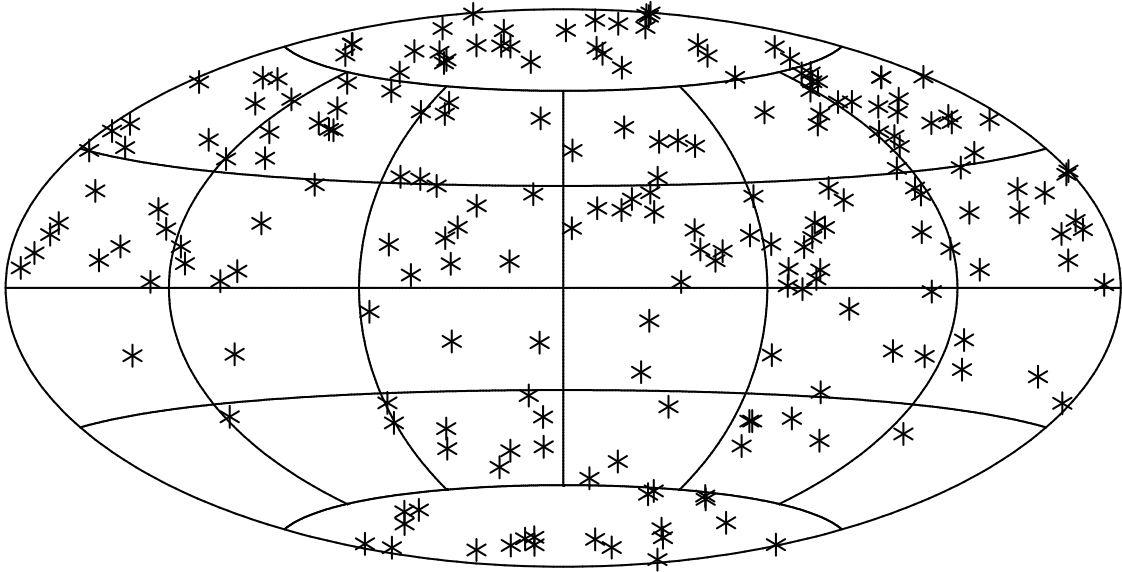


FIG. 13. Distribution of the 212 best-observed extragalactic sources comprising the new IAU celestial reference frame (ICRF). A conventional equal-area projection is used: declination increases from -90° to $+90^\circ$ (bottom to top), and right ascension from -12 to 12 hr (left to right). Note the relatively sparse population at negative declinations.

During the last two decades, several research groups have used the VLBI technique to catalog the positions of extragalactic radio sources (Robertson *et al.*, 1986; Sovers *et al.*, 1988; Ma *et al.*, 1990; Johnston *et al.*, 1995). The number of objects whose positions are known at the mas level now exceeds 400. A considerable fraction of these continue to be monitored in periodic experiments. Survey campaigns (*e.g.* Patnaik *et al.*, 1992) with the MERLIN and VLA arrays), meanwhile, have accumulated somewhat less precise coordinates of several thousand additional radio sources, which form a valuable pool of candidates for inclusion in the higher-precision reference frame. Some applications of extragalactic radio reference frames have been to deep space navigation (*e.g.* Border and Koukos, 1993), Earth orientation measurements (*e.g.* IERS, 1994), geodesy (*e.g.* Fallon and Dillinger, 1992), and astrometry (*e.g.* Bartel, 1985; Treuhaft and Lowe, 1991; Lebach *et al.*, 1995). In addition to the intrinsic scientific interest in the stability of dynamical systems, these diverse applications require accurate and stable positions of the objects composing the reference frames. The International Astronomical Union has now adopted a new fundamental celestial reference frame (the International Celestial Reference Frame, ICRF) that is based on the angular coordinates of 212 radio sources (IAU, 1996; Ma *et al.*, 1997). Figure 13 illustrates the distribution of the defining sources over the sky. This is the first time that the fundamental celestial coordinate system is no longer based on observations at visible wavelengths. The ICRF is approximately 100 times more accurate than the FK5 catalog, the present realization of the fundamental optical celestial frame.

Limitations of reference frames that are based on extragalactic radio sources have been recognized for some time. While estimates of the proper motion of quasars presently give null results at the approximate level of 50 μ rad/yr (Eubanks *et al.*, 1996), the extended structure of the emitting objects at the nrad level is ubiquitous. Structure that is constant in time can be handled by careful definition of a fiducial point for each source. Unfortunately, many sources show considerable time variability, and thus require constant monitoring to ensure stability of the reference frame.

Such variability can be considered to belong in the category of systematic errors. Specialized imaging experiments are being carried out in order to correct for source structure and its variation (Fey *et al.*, 1996). Imaging is also feasible, however, via reanalysis of older data collected primarily for geodetic purposes (*e.g.* Charlot, 1994; Piner and Kingham, 1997). Figure 14 shows such results for the source 3C 273 in 1986. It can be seen that the central core and neighboring components (“jet”) extend over several mas, making it impossible to establish a fiducial mark at the sub-milliarcsecond level without detailed study. Similar images at other epochs show that the components of the jet move rapidly, and new components are ejected sporadically. After this structure and its time variation was characterized in the 1980s, it was dropped from most observing schedules. The vast majority of the defining sources of the ICRF, however, are much more point-like.

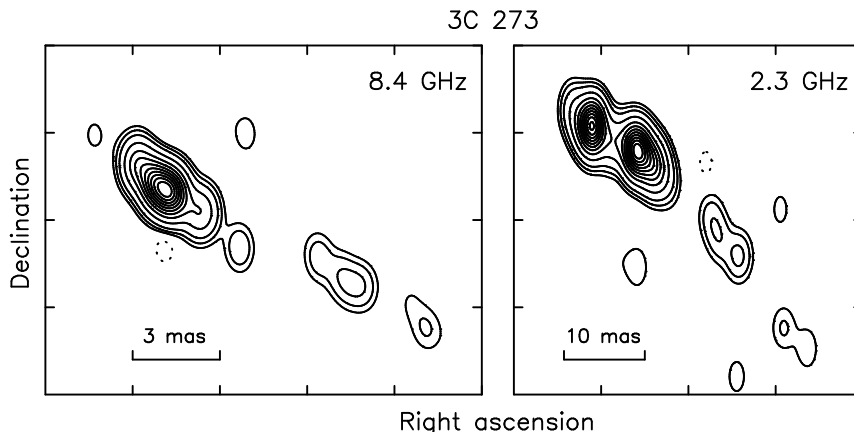


FIG. 14. Typical maps of the S- and X-band intensity distribution of the source 3C 273, generated from geodetic VLBI data for the epoch 1986.27.

Another source of instability of the extragalactic reference frame originates in the motion of the Solar System due to the rotation of our Galaxy relative to the extragalactic radio sources. Detection of the acceleration of the SSB is now on the borderline of possibility. As mentioned in Sec. III.E, the motion of the Solar System in inertial space makes its presence felt if observational data extend over a sufficiently long time span. To the extent that the Earth moves along with the uniform rotation of our Galaxy and the distance to the Galactic Center is known, this would amount to an indirect measurement of the period of galactic rotation. Such results could also make a contribution to our understanding of cosmology from comparisons to motion of the SSB with respect to the cosmic background radiation. A related topic is the proposed use of VLBI measurements to determine the distance to the Galactic center (Reid, 1993) which would be of importance in establishing a more reliable cosmic distance scale.

The terrestrial reference frame has its origin at the Earth’s center of mass and establishes fiducial points on the surface of the Earth. Prior to the advent of space geodetic experiments, there was no global connection of national geodetic grids at a level better than ≈ 1 meter. Doppler tracking of artificial Earth satellites improved this situation, and the advent of laser ranging, VLBI, and global positioning satellite tracking has further increased the accuracy of global reference frames to approach 1 cm in the late 1990s. In the arena of terrestrial reference frames, VLBI measurements have contributed significantly to the establishment of more than 100 fiducial points fairly uniformly distributed over the Earth’s surface, which collectively comprise the ITRF: International Terrestrial Reference Frame (Boucher *et al.*, 1996). Figure 15 shows the global distribution of VLBI stations that contribute to the ITRF, while Fig. 19 of Sec. VI.B gives an example of such results. The VLBI technique has not been the only contributor to an improved terrestrial reference frame. Laser ranging to satellites and the recent proliferation of GPS measurements have begun to play a dominant role in forming a unified terrestrial coordinate system that is accurate at the centimeter level. This provides a global reference for the national geodetic networks which have been traditionally established by conventional triangulation methods; these networks are being densified by GPS measurements. The result is a globally coherent reference system which provides a backdrop for numerous studies of the Earth’s behavior. Some limitations to its stability are discussed in the next section.

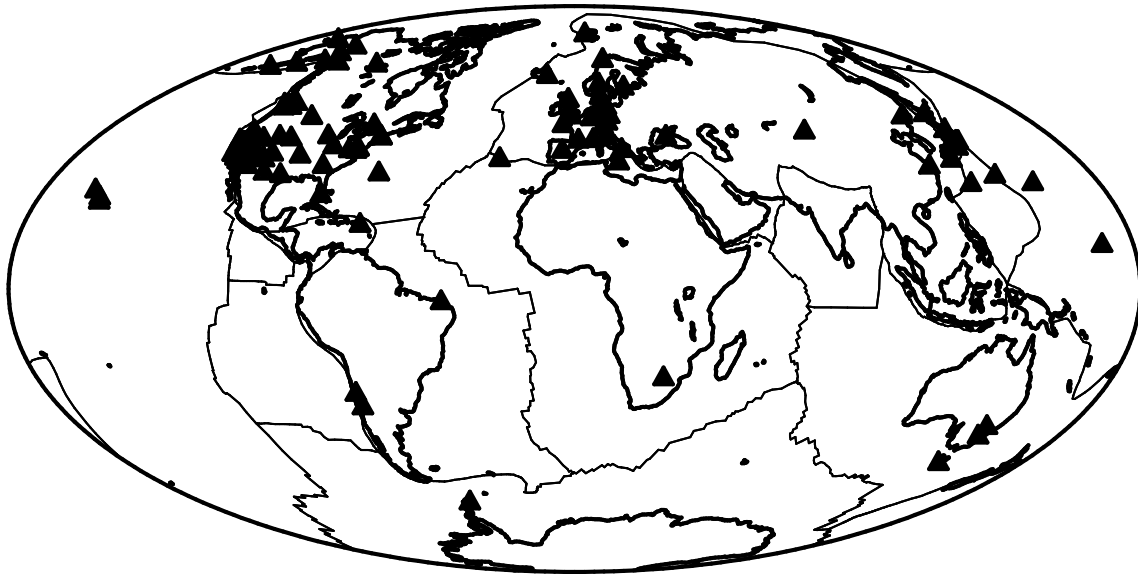


FIG. 15. Distribution of 104 VLBI observing stations that contribute to the International Terrestrial Reference Frame (ITRF). An equal-area projection of the Earth's surface is used. Note the heavy concentration in the northern hemisphere.

It must be noted that both current celestial and terrestrial reference frames exhibit a pronounced northern bias. Due to the dominance of observing stations in the northern hemisphere, there has been nonuniform coverage of both the Earth's surface and the celestial sphere. For example, fewer than one fifth of the 50 best-determined ITRF sites are in the southern hemisphere, and fewer than one third of the 212 sources that are included in the new ICRF are at negative declinations (Figs. 13 and 15). It is expected that future development of observatories in the southern hemisphere will remedy this situation to the extent possible with the limited land area available south of the Earth's equator.

B. Earth orientation and structure

The motion of the Earth as a whole, as well as its surface and bulk composition and structure, are also areas in which VLBI measurements have made significant contributions. There are basically two classes of Earth-related applications. They pertain either to orientation of the structure as a whole, or to motions of its crust. Both categories have varied root causes: Solar System dynamics and internal, oceanic, and atmospheric processes on the Earth. Manifestations of most of these complicated motions are for the most part far removed from ordinary human experience. One exception may be the irregular slowing of the Earth's rotation, which necessitates the introduction of occasional "leap seconds" in order to keep synchrony between the Earth's rotation and atomic time. Many of the remaining effects have amplitudes that are only on the order of a meter or less at the Earth's surface, but their characterization is of crucial importance in building a coherent picture of our planet and its environment.

Precise specification of the orientation of the Earth is of practical importance, for example, in navigating spacecraft to other planets. The seemingly minuscule errors of parts per billion are magnified into errors of kilometers near Jupiter. Predictions of future Earth rotation values (particularly UT1) lose accuracy very rapidly for times past a few weeks after the date of measurement and extrapolation. Continuous monitoring of Earth rotation is therefore imperative for applications that require high-quality real-time UTPM. Substantial help in this regard comes from a perhaps unexpected source: the global distribution of atmospheric winds or more precisely total atmospheric angular momentum (AAM), which is widely monitored in real time for weather forecasting.

Measurements of the rotation of the Earth and the wandering of its spin axis relative to the crust contain a great deal of information related to diverse physical processes. While to a good approximation the rotation rate is constant, it has slowed considerably over geological time scales. The length of a day was only 18 hours 900 million years ago as determined from recent analyses of tidal sediments (Sonett *et al.*, 1996). A number of phenomena come into play in determining the rotation rate, ranging from the lengthening of the Earth-Moon distance, to frictional and

electromagnetic forces between the Earth’s core and mantle, to frictional forces between winds and ocean water and the surface. Presently the rate of deceleration is much larger than the billion-year average, on the order of 2 ms per day, but it is known to have reversed sign within the last hundred years (Archinal, 1992b). The spin axis has a quasi-periodic motion that describes an approximate circle of ≈ 20 m diameter (see Fig. 16) in ≈ 300 days whose center also wanders by tens of meters over decades; the size of the circle fluctuates with a period of approximately 7 years. In addition to motions with respect to the Earth’s crust, the spin axis also exhibits motion in inertial space (nutation). The two nutation angles are usually included along with the three quantities describing Earth rotation to form a set of five “Earth orientation” parameters. The radio interferometric technique, along with other space geodetic experiments, has brought about orders-of-magnitude improvements in measurements of small irregularities in these motions, thereby opening prospects for detecting numerous periodic and aperiodic processes. We summarize the present accuracy of Earth orientation determinations, and present examples of contributions of the results to two diverse fields of geophysics.

With a network of several stations that are reasonably uniformly distributed over the surface of the Earth, and separated by baselines on the order of an Earth radius, it is possible to infer the Earth orientation parameters to an accuracy level that is better than 1 mas (a few nanoradians, or parts per billion). To illustrate VLBI measurements of Earth orientation, Figs. 16 and 17 show the variation of the position of the spin axis relative to the crust, and the rate of rotation, during a part of the 1980s and 1990s. As seen in Fig. 16 the spin axis follows a nearly circular path,

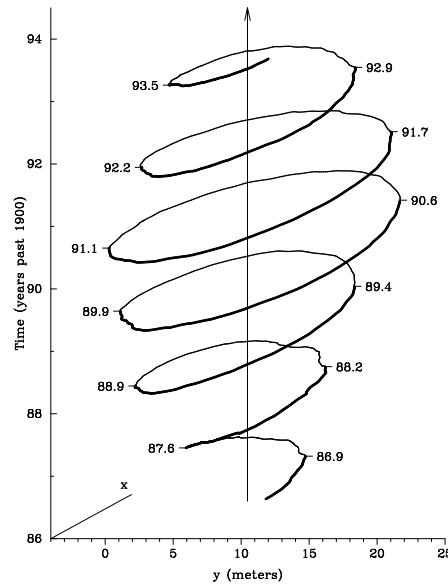


FIG. 16. Observed crust-fixed position of the Earth’s spin axis during the years 1986-1993. The origin is at the conventional pole of 1903, and the upward arrow indicates the approximate present-day average pole position.

with a diameter that oscillates between a few meters and 20 m with a period of approximately seven years. The deceleration of the Earth’s rotation rate is seen in the bottom part of Fig. 17 as a lag behind atomic time (TAI). The resulting excess length of day is seen in the top part of the figure: it exhibits a rich spectrum which is just now beginning to be understood in detail. The dominant oscillations are caused by the annual interchange of atmospheric angular momentum with the solid Earth.

Experimental determinations of the Earth’s rotation rate show that it is not constant at the level of a few parts per billion. There are annual and semiannual cycles in the length of day, both with amplitudes of approximately 0.3 ms and minima in January and July (Eubanks, 1993). Since the early 1980s it has been known that most of this variability is well correlated with the total AAM (Morgan *et al.*, 1985). Refinement of this correlation was made possible by the superior precision of VLBI relative to classical Earth orientation measurements using optical techniques. Variations in the atmospheric angular momentum are transferred (via friction and forces on mountain ranges) to variations of the angular momentum of the solid Earth, conserving total angular momentum. This discovery has made substantial improvements in our ability to perform short-range forecasts of Earth rotation. Global weather measurements play a significant role in this process, and their rapid availability is crucial in improving forecast quality (Freedman *et al.*, 1994). As with most global geophysical measurements, the spatial and temporal density is inadequate at some

level. Relatively few weather stations operate in the southern hemisphere, and the strong winds at high altitudes (pressures of 100 to 1 mbar) are significant (Rosen and Salstein, 1985). In addition to the dominant 0.6-ms effect of atmospheric angular momentum, a number of smaller meteorological and tidal effects contribute to irregularities in Earth rotation. Before considering some selected examples of these, we discuss the remaining components of Earth orientation: the two nutation angles that specify Earth orientation in an inertial frame.

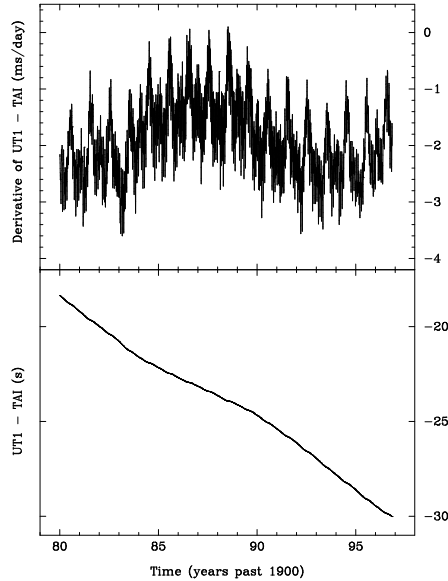


FIG. 17. Observed rotation rate of the Earth during the years 1980-1996. The bottom plot shows the discrepancy of time measured by atomic clocks and by the Earth's rotation, while the top plot shows the increase of a few ms per day in the length of the day. The annual variations are caused by wind-surface friction.

In response to torques exerted by the Sun and Moon, the Earth's spin axis oscillates in fundamental modes distributed over a wide range of frequencies. The amplitudes of these motions can be calculated fairly precisely based on classical dynamics. At the discrimination level of modern measurement techniques, however, the theoretical models are not adequate. The relatively poorly understood internal structure of the Earth plays a large role in some of these motions, and empirical measurements have just begun to shed light on the underlying mechanisms. In the 1970s it became increasingly clear that the then-standard Woolard nutation model was insufficiently accurate for analyses of modern data. Based on the theoretical work of Gilbert and Dziewonski (1975) and Kinoshita (1977), Wahr developed a new nutation series (1979; 1981), which was adopted by the International Astronomical Union in 1980 (Seidelmann, 1982). These two series describe the time variation of the nutations in longitude and obliquity by superposing oscillations at a total of 106 frequencies, with amplitudes of 0.1 mas precision. Only a few years after the adoption of the 1980 IAU model, VLBI measurements revealed significant errors, predominantly at semiannual, annual, and 18.6-yr periods. Herring *et al.* (1986) initially pointed out these discrepancies, and gave improved estimates of a number of amplitudes from VLBI analyses. Gwinn *et al.* (1986) subsequently interpreted them as manifestations of irregularities in the figure of the Earth's inner core.

As an example of the ability and evolution of VLBI techniques in the measurement of the Earth's spin axis in inertial space, Fig. 18 shows plots of the two nutation angles $\Delta\psi$ and $\Delta\varepsilon$ during the history of regular astrometric VLBI measurements. The plots show corrections to the standard (1980 IAU) theoretical model of nutation. It is apparent that there are highly regular deficiencies at the 10-mas level. Yearly and semiannual frequencies are clearly visible, along with long-term (linear and 18.6-y period) discrepancies of considerable size.

The dominant nutation in longitude, with a period of 18.6 years, is difficult to separate from precession (26,000-yr period) with short data spans. Only recently has the history of VLBI observations reached a time span of one 18.6-yr period, permitting this decoupling. Determinations of the nutation amplitudes and precession at the levels of a milliarcsecond and a few tenths of mas/yr, respectively, have been made by Herring (1988), Charlot *et al.* (1995), Walter and Ma (1994), and Walter and Sovers (1996). The value of the precession constant which was determined from optical measurements in the 1970s (Fricke, 1977) has been found to be in error by 3 mas/yr. Most recently, it has been found that torques from bodies other than the Sun and Moon can contribute to nutation of the Earth at a level

of 0.1 mas (Kinoshita and Souchay, 1990). These have not yet been directly detected, but evidence is accumulating that accounting for their cumulative effect improves the fit of the VLBI model to experiment. Another revision of the official IAU nutation series is expected to include several hundred additional terms, and to correct many amplitudes on the basis of empirical VLBI determinations.

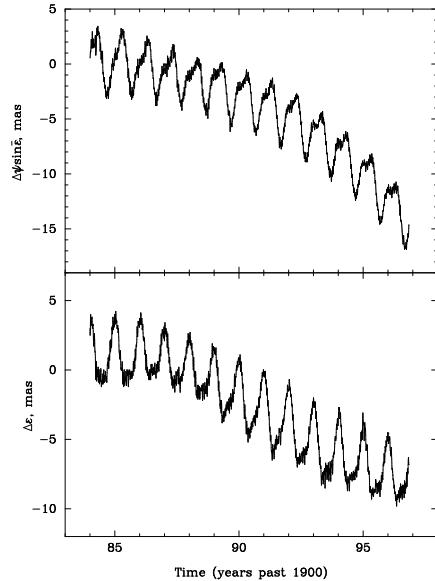


FIG. 18. Discrepancies of measured nutation angles and the 1980 IAU models during the years 1984-1996. Both the obliquity $\Delta\varepsilon$ and longitude $\Delta\psi \sin \bar{\varepsilon}$ are shown. Short-term (annual and semiannual) and long-term (linear and 18.6-year) discrepancies are evident.

Gravitational forces from the Solar System, predominantly the Sun and Moon, cause a rich spectrum in the tidal response of the solid Earth and its oceans and atmosphere. Direct motions of the Earth’s crust (with amplitudes on the order of a meter) are quite obvious in VLBI analyses, but smaller secondary effects on station positions and Earth orientation also cause measurable effects, and need to be considered. One of the first estimates of the solid Earth’s tidal response was the determination of Love numbers from VLBI by Herring *et al.* (1983): $h = 0.62 \pm 0.01$, $l = 0.11 \pm 0.03$, and a phase lag $\phi = 1^\circ \pm 1^\circ$. More recent work (Haas and Schuh, 1996; Gipson, 1996) shows that the response factors at numerous tidal frequencies can be reliably obtained from analyses of VLBI measurements.

Perhaps the most important of the secondary tidal effects is the modification of Earth orientation by mass redistribution in the oceans by global tides. This affects both the rotation rate (UT1) and orientation of the spin axis (PM). Brosche *et al.* (1989) made the initial attempts to model these “fast UTPM” variation amplitudes. In the early 1990s several independent determinations by VLBI and SLR of the Earth orientation amplitudes induced by 8 ocean tidal components gave results in good agreement with each other (Sovers *et al.*, 1993; Herring and Dong, 1994; Watkins *et al.*, 1994). Initially their agreement with purely theoretical values based on global tide models was not good, but it is improving (Gross, 1993; Ray *et al.*, 1994; Chao *et al.*, 1996; Gipson, 1996), as the global tide model is refined by TOPEX/Poseidon results. Agreement is now at the level of 10 μas .

In addition to affecting the orientation of the whole Earth, global redistribution of mass in the oceans by tidal action also causes local motions of stations on the Earth’s crust. These “ocean loading” amplitudes have been incorporated in VLBI models since the 1980s (Scherneck, 1983), and can amount to motions of several cm. Although their small size places them close to the current resolution limit of VLBI, long data spans are capable of yielding significant direct determination of their amplitudes (Sovers, 1994). By analogy with oscillations in the distribution of ocean water, variations in the atmospheric pressure at an observing site can also cause long-term vertical motions with amplitudes of many mm. This “atmospheric loading” has been detected in VLBI analyses (Rabbel and Schuh, 1986; Manabe *et al.*, 1991; van Dam *et al.*, 1994).

Another minor systematic effect which has only very recently been identified is post-glacial rebound: the slow relaxation of the Earth’s crust in response to melting of the thick ice sheets which covered it during the last glaciation. The dominant motion is vertical, and theoretical models produce estimates of several mm/year (Peltier, 1995). Unfortunately, determination of the vertical component of station motion is notoriously weak relative to the two

horizontal components, because of the strong correlation of the vertical with the zenith tropospheric delay. Nevertheless, recent empirical estimates for a number of VLBI observing stations with sufficiently long observation histories (Argus, 1996; Ryan *et al.*, 1997) have produced results that are in fair agreement with theoretical models (Mitrovica *et al.*, 1993).

A limitation to the stability of the terrestrial reference frame, which is also of great interest for its own sake, is the motion of the tectonic plates that constitute the Earth's solid surface. Since this possibility was proposed by Wegener in the early part of the 20th century, the existence of tectonic motion has been confirmed for time scales of millions of years. This was achieved by detailed cataloging of magnetization properties of crust near active plate boundaries (Minster and Jordan, 1978; DeMets *et al.*, 1990). As the time base for space geodetic station motions became sufficiently long in the 1980s, the astonishing result emerged that present-day (decade scale) plate motions are very similar to those inferred from paleomagnetic data (Myr scale). This attests to the relatively smooth character of the forces driving plate tectonics. At present, the rates of motion of more than a dozen tectonic plates that have been occupied by VLBI stations are known to within fractions of mm/year (Fallon and Dillinger, 1992; Argus and Gordon, 1996; Boucher *et al.*, 1996).

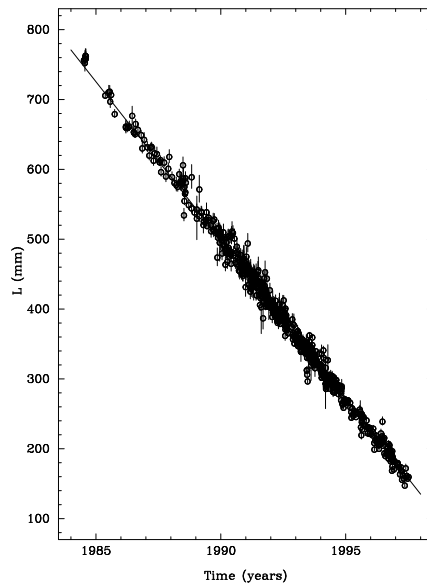


FIG. 19. Measured baseline between Alaska and Hawaii during 514 VLBI observing sessions, 1984-1997. L is the baseline length in mm, minus a constant offset of 4728114 meters. The weighted RMS scatter about the linear trend of -46 mm/yr is 7 mm.

As an example of the manifestation of tectonic station motion, Fig. 19 shows results of VLBI measurements of the length of the baseline connecting stations at Gilmore Creek, Alaska and Kokee Park, Hawaii (island of Kauai) during the years 1984-1997. This figure is derived from results of Goddard Space Flight Center 1997 data analyses, archived at the World Wide Web site <http://lupus.gsfc.nasa.gov/vlbi.html>. Several points of interest are illustrated by the time history of this particular baseline. First, the North American (Alaska) and Pacific (Hawaii) plates are one of the fastest moving pairs of tectonic plates, converging at nearly 5 cm/yr. Second, there is nearly perfect agreement of the measured rate of change (-46 mm/yr) with the Nuvel model rate of -45 mm/yr. Third, the weighted root-mean-square scatter about a perfectly linear trend is approximately 7 mm, which is a typical result for a baseline of this length (≈ 4700 km), and amounts to 1.5 ppb. Fourth, the evolution of the VLBI technique is illustrated by the increased frequency of experiments and the decrease in baseline length uncertainties during the 1980s and 1990s. Fifth, even the current theoretical models have some systematic errors, which may be manifested in some of the departures from linearity, *e.g.*, in 1994-96. Finally, the general stability of the experimental techniques is shown by the smooth transitions at the epochs of both a large natural and a man-made perturbation at Kauai: the hurricane damage in late 1992 and the transition to a new antenna, 40 meters distant, during the summer of 1993 are hardly noticeable in Fig. 19.

Proximity of VLBI stations to the epicenters of strong earthquakes, and to active faults (especially the San Andreas fault in California) is starting to contribute to improved understanding of the forces that are involved in these motions.

Several pairs of measurements of station coordinates before and after substantial earthquakes now exist (Clark *et al.*, 1990). They confirm permanent, essentially instantaneous displacements of several cm, but the resolution is not sufficient to detect any relaxation mechanisms in the subsequent hours and days. The relatively dense network of stations on both sides of the San Andreas fault show that the magnitude of horizontal motion associated with the fault movement decreases with increasing distance from the fault (Ward, 1988). Two reviews (DeMets, 1995; Larson, 1995) contain more detailed discussion of recent results related to global tectonics and crustal deformation. A recently developed technique of active interferometry, synthetic aperture radar (SAR), shows promise of accurate and timely determination of regional deformations associated with tectonic and earthquake activity (Zebker *et al.*, 1994).

C. Troposphere and ionosphere

Atmospheric effects have long been the bane of Earth-based astronomy. They continue to play that role for interferometry at radio wavelengths. In contrast to many of the more deterministic parts of the VLBI model, the effects of the atmosphere are not easily predicted or externally quantified. The experiments themselves must therefore serve to characterize atmospheric behavior. In addition to the global effects of the atmosphere (AAM) that were already mentioned in connection with the above discussion of Earth rotation, we consider two additional aspects here. At best, empirical estimation can yield time series of accurate atmospheric parameters, whose applicability is unfortunately limited to the times and locations of the experiments.

Determination of ionospheric electron content is possible whenever the VLBI measurements are performed at two widely separated frequencies. The details of this dual-frequency calibration process can be used to determine the integrated electron density along the incoming ray path. Limited sampling in both time and space, however, limits the utility of VLBI as a method for studying the global ionosphere. Satellite techniques give a much denser data set, and routine generation of ionospheric maps is currently being implemented using GPS measurements both with ground-based receivers and other satellites in low Earth orbit (Wilson *et al.*, 1995; Ho *et al.*, 1996).

Estimating the zenith tropospheric delay at frequent time intervals for each VLBI station during data analysis permits monitoring the time variation of water vapor content above that station. These intervals can even be reduced to essentially the intervals between observations if a stochastic filtering scheme is used (*e.g.* Herring *et al.*, 1990). If the observing schedule has ensured a good spatial distribution of measurements (including low elevation angles), then the uncertainties of the derived zenith wet delays are typically on the order of a few mm. Comparisons of water vapor radiometer and VLBI results have demonstrated the ability to track the atmospheric water vapor content quite faithfully (Elgered *et al.*, 1991; Teitelbaum *et al.*, 1996). For the highest accuracy, it is important to account for both the temporal and spatial correlations of fluctuations of the tropospheric delay. Stochastic estimation schemes can account for temporal correlations. To describe atmospheric spatial asymmetry, horizontal gradient parameters may be estimated. An analysis scheme utilizing a theoretical model of atmospheric turbulence which also contains parameters to quantify the “clumpiness” of the atmosphere (Treuhaft and Lanyi, 1987; Treuhaft and Lowe, 1991) accounts for correlations between VLBI delays as a function of both time and space. It also gives a better description of the influence of both the water vapor content and wind distribution surrounding a site (Naudet, 1995).

D. Relativity

At the precision level of intercontinental VLBI measurements, the incoming signals are affected by their passage through the varying gravitational potential within the Solar System. Since the positions and velocities (ephemerides) of all the major gravitating bodies are known to a high degree of accuracy, analyses of the experiments provide a means of testing alternative relativistic theories. Shapiro (1964) first suggested that timing experiments on radio waves propagating through the Solar System can be used to measure the parameter γ_{PPN} of parametrized post-Newtonian relativity theory. These original measurements of radar reflections from the inner planets (Shapiro, 1967) gave the result $\gamma_{\text{PPN}} = 0.9 \pm 0.2$. Determinations of γ_{PPN} from geodetic VLBI data spanning more than a decade gives $\gamma_{\text{PPN}} = 1.000 \pm 0.002$ (Robertson and Carter, 1984; Robertson *et al.*, 1991). This uncertainty, $\sigma_\gamma = 0.002$, is competitive with the results of specifically designed experiments of much shorter duration. An example of the latter is a VLBI experiment which also observes at a third frequency (K band, >12 GHz) in addition to the standard S-band and X-band wavelengths (Lebach *et al.*, 1995). This yields $\gamma_{\text{PPN}} = 0.9996 \pm 0.0017$, a somewhat improved σ_γ despite an order of magnitude fewer data. Experiments scheduling numerous observations in the vicinity of the Sun can achieve equivalent results with just a fraction of the data, because of the extremely steep variation of gravitational delay with closest approach to the Sun. The higher K-band frequency is less sensitive to the corrupting influence of

plasma-induced phase scintillation. The estimated value of unity for γ_{PPN} (within one standard deviation in all cases) indicates agreement with Einstein’s general relativity.

Unfortunately none of the other parameters of post-Newtonian relativity theory are accessible to measurement with VLBI experiments. Nonlinearity in the superposition of gravity β and the time dependence of the universal gravitational constant \dot{G}/G cannot be determined from VLBI, but limits are being placed on their magnitudes by analysis of lunar laser ranging data (Williams *et al.*, 1996). Initial searches for VLBI evidence of the passage of gravitational waves have placed loose bounds on their existence (Pyne *et al.*, 1996; Gwinn *et al.*, 1997). We also note that VLBI is weakly sensitive to the difference between Newtonian and Lorentzian aberration [$\propto 1/4(v/c)^2$], which is a 1-cm effect for long baselines and is implicitly included in the VLBI model.

VII. PROGNOSIS FOR FUTURE MODEL IMPROVEMENTS

Data analysis has provided continuous feedback to experiments by characterizing previously unknown or poorly quantified aspects of the model (*e.g.*, nutation, tidal variations, troposphere). Such interplay is certain to continue in the future, as both experimental and theoretical techniques are refined to eliminate remaining systematic errors. This section gives condensed summaries of areas which will require close attention in the future if improvements of the current VLBI model are to permit achieving true part-per-billion accuracy.

Both special and general relativistic aspects of the current model could be improved. Second-order general relativistic effects have not yet been thoroughly investigated, but probably do not contribute at the picosecond level. Theoretical studies such as that of Turyshev (1996) may make a valuable contribution here. If variations of the gravitational potential along the path of the baseline through the Earth are taken into account in calculating the proper distance, this correction was estimated by Thomas (1991) to amount to 2 mm for a 10,000 km baseline. Similarly, variations in the gravitational potential at the station clocks are only approximately accounted for by means of Eq. (3.31). Concerning special relativistic aspects, the Fairhead and Bretagnon (1990) extension of the work of Moyer (1981) on the “time ephemeris” produces higher-order terms that contribute to TDB–TDT at the μs level.

Galactic effects may soon emerge above the detection threshold. The rotational motion of the Galaxy produces aberrational effects which change by 20 prad/yr. This will need to be taken into account for observations spanning more than two decades.

The rich tidal spectrum of the solid Earth and its oceans will be a source of model refinements for some time to come. Direct contributions of the planets to solid Earth tidal displacements can reach the millimeter level. In addition to the eight frequencies considered in the model described in Sec. III.D.1.a, short-period variations of UTPM have additional components (Seiler and Wunsch, 1995; Gipson, 1996). Those which are significant at the mm level will emerge as data analyses are refined. Empirical estimates of ocean loading amplitudes for several IRIS stations (Sovers, 1994) indicate that the best theoretically derived amplitudes may be in error by several mm. Future refinements in data analyses, and improved global ocean models from the recent TOPEX/Poseidon mission (Le Provost *et al.*, 1995; Fu *et al.*, 1994) may improve the accuracy of the theoretical ocean loading model to the mm level. Resonance with the Earth’s free core nutation may modify some of the amplitude corrections at nearly diurnal frequencies by ≈ 1 mm. Ocean tides cause motion of the center of mass of the solid Earth due to motion of the center of mass of the oceans (Brosche and Wunsch, 1993). The amplitude of this displacement can be as large as 1 cm at the usual diurnal and semidiurnal tidal frequencies. Non-conservation of the total angular momentum of the Earth via interchange with the Sun and Moon is also not included in the tidal models (Brosche and Seiler, 1996). The effects of both of these refinements on VLBI observations must be assessed. The retarded tidal potential effect mentioned in Sec. III.C.2.a can be as large as several tenths of mm. Thus, for correct modeling at the mm level, the light travel time should be accounted for.

Non-point like flux distributions of the radio sources are being efficiently mapped by experimenters using the VLBA (Fey *et al.*, 1996). Their results are expected to provide improved models for astrometric and geodetic VLBI. Meanwhile, estimates of parameters for simplified structural models may improve data analyses.

There are short-period deficiencies in the present International Astronomical Union models for the orientation of the Earth in space that may be as large as 1 to 2 milliarcseconds, and longer-term deficiencies on the order of 1 mas per year (3 cm at one Earth radius). VLBI measurements made during the past decade indicate the need for revisions of this order of the annual nutation terms and the precession constant (Eubanks *et al.*, 1985; Herring *et al.*, 1986). The 18.6-year components of the IAU nutation series are also in error, and present data spans are just approaching durations long enough to separate them from precession. Options to improve the nutation model were discussed in Sec. III.D.2. Any of these constitute a provisionally improved model, especially for the annual and semiannual

nutations, until the IAU series is officially revised. Future refinements of the equation of the equinoxes (Eq. 3.86) will probably lead to changes on the order of tens of μs in the hour angle.

The large dish antennas that are used to collect signals from extragalactic sources are susceptible to various instabilities at the level of many mm. Gravity loading may cause systematic variations in the position of the reference point of a large antenna that are as large as 1 cm in the local vertical direction. Such systematic errors and their dependence on antenna orientation and temperature may be modeled (Clark and Thomsen, 1988; Jacobs and Rius, 1989). The geometric structure of each antenna, as well as its alignment with respect to local site features, should be carefully checked against design specifications. For example, hour angle misalignment on the order of 1 arc minute can cause 1 mm delay effects for HA-Dec antennas with 7-m axis offsets. Thermal expansion of the portion of an antenna above the reference point may induce delay signatures that are several mm peak-to-peak for a typical VLBI antenna (Nothnagel *et al.*, 1995). It is thus imperative to model this effect for achievement of the highest accuracy.

The limits of validity of the dual-frequency calibration procedure for ionospheric effects need to be carefully established, in conjunction with consideration of plasma effects for ray paths near the Sun. In addition, corrections for the gyrofrequency effect may reach a millimeter.

New techniques for characterizing the atmosphere are expected to allow more realistic modeling of the tropospheric delay than the simple spherical-shell model underlying all the results of Sec. V.B. When comprehensive atmospheric data from a region surrounding each observing site are available, present computer speeds should permit estimating the tropospheric delay by means of a complete ray-tracing solution for every observation. Meanwhile, improvements in tropospheric mapping can be sought by modeling variations of the temperature *vs.* altitude profile as a function of season, latitude, altitude, and diurnal cycle. Efforts are also under way (*e.g.* MacMillan and Ma, 1997; Chen and Herring, 1997), to model azimuthal gradients in the troposphere. Persistent equator-to-pole gradients in pressure, temperature, humidity, and tropopause height suggest that *a priori* modeling of North-South gradients may be beneficial. East-West gradients, which are probably dominated by weather systems passing over a site, are likely to be more difficult to model without extensive weather data.

By the late 1990s astrometric and geodetic radio interferometry has largely fulfilled the promise seen for the technique at its inception in the late 1960s. VLBI has yielded a new nearly inertial celestial reference frame that is accurate at a level of nanoradians, achieved point positioning on the Earth at the centimeter level, and produced the capability of determining the instantaneous orientation of Earth in space at similar accuracy levels. The VLBI technique has intersected many fields of physics, and its evolution has involved both routine and unexpected components. In addition to improved quantification of known physics, there was need to take into account a number of unexpected contributions, which led to enhanced understanding of the behavior of the Earth. The field is still developing vigorously both on the experimental and theoretical fronts. It can be hoped that progress will not be unduly impeded by numerous processes effective at the millimeter level. The future holds the promise of exciting and unexpected results characterizing the behavior of the Earth, the structure and emission mechanisms of extragalactic radio sources, and the motion the Earth in the universe.

ACKNOWLEDGMENTS

Numerous people at many organizations on several continents have contributed to the evolution of the present VLBI model during the past two decades, and we have personally benefitted from interacting with many of them. Our own initiation into VLBI studies at JPL was guided by J. B. Thomas and J. G. Williams during the 1970s. Critical internal reviews of this manuscript were kindly done by J. H. Lieske, W. M. Owen, Jr., and J. G. Williams, and externally by T. M. Eubanks, J.-F. Lestrade, L. Yu. Petrov, and H. G. Walter. Suggestions of a referee stimulated us to broaden its scope. The work described in this paper was performed at the Jet Propulsion Laboratory, California Institute of Technology, under contract with the National Aeronautics and Space Administration.

REFERENCES

- Adam, J., 1995, "Report of IAG Special Study Group 2.109: Application of Space VLBI in the Field of Astrometry and Geodynamics", in *Travaux de L'Association Internationale de Geodesie*, edited by P. Willis, Tome 30 (Int. Assoc. of Geodesy, Paris, France), p. 114.
- Allen, S. L., 1982, "Mobile Station Locations", Jet Propulsion Laboratory IOM 335.1-71, Pasadena, CA.
- American Geophysical Union, 1995, *Water Vapor in the Climate System*, Special Report (AGU, Washington, DC).

- Andersen, P.-H., 1995, "High-precision Station Positioning and Satellite Orbit Determination", NDRE *Publ. 95/01094*, Kjeller, Norway.
- Aoki, S., B. Guinot, G. H. Kaplan, H. Kinoshita, D. D. McCarthy, and P. K. Seidelmann, 1982, *Astron. Astrophys.* **105**, 359.
- Archinal, B. A., 1992a, in *Explanatory Supplement to the Astronomical Almanac*, edited by P. K. Seidelmann (University Science Books, Mill Valley, CA), p. 252.
- Archinal, B. A., 1992b, in *Explanatory Supplement to the Astronomical Almanac*, edited by P. K. Seidelmann (University Science Books, Mill Valley, CA), p. 267.
- Argus, D. F., 1996, *Geophys. Res. Lett.* **23**, 973.
- Argus, D. F., and R. G. Gordon, 1991, *Geophys. Res. Lett.* **18**, 2039.
- Argus, D. F., and R. G. Gordon, 1996, *J. Geophys. Res.* **101**, 13555.
- Arya, S. P., 1988, *Introduction to Micrometeorology*, (Academic Press, San Diego), Chap. 5.
- Baader, H.-R., P. Brosche, and W. Hövel, 1983, *J. Geophys.* **52**, 140.
- Bare, C., B. G. Clark, K. I. Kellermann, M. H. Cohen, and D. L. Jauncey, 1967, *Science* **157**, 189.
- Bartel, N., M. I. Ratner, I. I. Shapiro, R. J. Cappallo, A. E. E. Rogers, and A. R. Whitney, 1985, *Astron. J.* **90**, 318.
- Bassiri, S., and G. A. Hajj, 1993, *Manuscr. Geod.* **18**, 280.
- Batty, M. J., D. L. Jauncey, P. T. Rayner, and S. Gulkis, 1982, *Astron. J.* **87**, 938.
- Bean, B. R., and E. J. Dutton, 1966, *Radio Meteorology*, National Bureau of Standards Monograph 92, (U. S. Govt. Printing Office, Washington, DC).
- Bierman, G., 1977, *Factorization Methods for Discrete Sequential Estimation*, (Academic Press, New York).
- Binney, J., and S. Tremaine, 1987, *Galactic Dynamics*, (Princeton U. Press, Princeton, NJ).
- Bolton, J. G., A. Savage, and A. E. Wright, 1979, *Aust. J. Phys.* **46**, 1.
- Border, J. S., and J. A. Koukos, 1993, in *Report of the Proceedings of the RF and Modulation Subpanel at the German Space Operations Centre*, edited by T. M. Nguyen, CCSDS B20.0-Y-1 (Consultative Committee for Space Data Systems), p. 1.
- Bosworth, J. M., R. J. Coates, and T. L. Fischetti, 1993, in *Contributions of Space Geodesy to Geodynamics: Technology*, edited by D. E. Smith and D. L. Turcotte, Geodynamics Series, Vol. 25 (Amer. Geophys. Union, Washington, DC), p. 1.
- Boucher, C., Z. Altamimi, M. Feissel, and P. Sillard, 1996, *IERS Technical Note 20*, (Observatoire de Paris, Paris, France).
- Bowring, B. R., 1976, *Survey Review (U.K.)* **XXIII**, 181.
- Brosche, P., 1982, in *Sun and Planetary System*, edited by W. Fricke and G. Teleki, (Reidel, Dordrecht), p. 179.
- Brosche, P., and U. Seiler, 1996, *Astron. Nachr.* **317**, 211.
- Brosche, P., U. Seiler, J. Sundermann, and J. Wünsch, 1989, *Astron. Astrophys.* **220**, 318.
- Brosche, P., and J. Wünsch, 1993, *Astron. Nachr.* **314**, 87.
- Brosche, P., J. Wünsch, J. Campbell, and H. Schuh, 1991, *Astron. Astrophys.* **245**, 676.
- Broten, N. W., T. H. Legg, J. L. Locke, C. W. McLeish, R. S. Richards, R. M. Chisholm, H. P. Gush, J. L. Yen, and J. A. Galt, 1967, *Nature* **215**, 38.
- Bureau International de l'Heure, 1983, "Annual Report for 1982"* (Observatoire de Paris, Paris, France).
- Bureau International des Poids et Mesures, 1997, "Circular T108"*, Sèvres, France.
- Burke, B. F., 1991, "Introduction to Orbiting VLBI", in *Advances in Space Research*, **11**, 349.
- Campbell, J., 1988, "European VLBI for Geodynamics", in *Proceedings of the 3rd International Conference on the WEGENER/MEDLAS Project*, University of Bologna, Bologna, Italy, p. 361.
- Carr, T. D., J. May, C. N. Olson, and G. F. Walls, 1965, *IEEE NEREM Record* **7**, 222.
- Carter, W. E., 1983, *Revs. of Geophys. Space Phys.* **21**, 565.
- Cartwright, D. E., and A. C. Edden, 1973, *Geophys. J. Roy. Astron. Soc.* **33**, 253.
- Chao, C. C., 1974, "The Troposphere Calibration Model for Mariner Mars 1971", Jet Propulsion Laboratory Technical Report 32-1587, Pasadena, CA.
- Chao, B. F., 1996, *Geophys. Res. Lett.* **22**, 3529.
- Chao, B. F., R. D. Ray, J. M. Gipson, G. D. Egbert, and C. Ma, 1996, *J. Geophys. Res.* **101**, 20151.
- Charlot, P., 1989, "Structure des Sources Radio Extragalactiques dans les Observations VLBI d'Astrométrie et de Géodynamique" (Ph. D. thesis, Observatoire de Paris, Paris, France).
- Charlot, P., 1990a, *Astron. J.* **99**, 1309.
- Charlot, P., 1990b, *Astron. Astrophys.* **229**, 51.
- Charlot, P., 1994, in *URSI/IAU Symposium on VLBI Technology – Progress and Future Observational Possibilities*, edited by T. Sasao, S. Manabe, O. Kawaya, and M. Inoue (Terra Scientific Publishing, Tokyo, Japan), p. 287.
- Charlot, P., and O. J. Sovers, 1998, to be submitted to *Astron. Astrophys.*
- Charlot, P., O. J. Sovers, J. G. Williams, and X X Newhall, 1995, *Astron. J.* **109**, 418.
- Chen, G., and T. A. Herring, 1997, *J. Geophys. Res.* **102**, 20489.
- Clark, T. A., 1979, *Revs. of Geophys. Space Phys.* **17**, 1430.
- Clark, T. A., C. Ma, J. M. Sauber, J. W. Ryan, D. Gordon, D. B. Shaffer, D. S. Caprette, and N. R. Vandenberg, 1990, *Geophys. Res. Lett.* **17**, 1215.
- Clark, T. A., and P. Thomsen, 1988, *Deformations in VLBI Antennas*, NASA Technical Memo 100696, Goddard Space Flight Center (Greenbelt, MD).

- Cohen, M. H., 1972, *Astrophys. J. Let.* **12**, 81.
- Cohen, M. H., and D. B. Shaffer, 1971, *Astrophys. Let.* **76**, 91.
- Cole, A. E., A. Court, and A. J. Cantor, 1965, "Model Atmospheres", in *Handbook of Geophysics and Space Environments*, edited by S. L. Valley, (McGraw-Hill, New York), p. 2-1.
- Davidson, J. M., and D. W. Trask, 1985, *IEEE Trans. Geosci. Rem. Sens.* **GE-23**, 426.
- Davis, J. L., T. A. Herring, I. I. Shapiro, A. E. E. Rogers, and G. Elgered, 1985, *Radio Science* **20**, 1593.
- Debye, P., 1929, *Polar Molecules*, (Dover, New York).
- DeMets, C., 1995, in *Dynamics of the Solid Earth and Other Planets*, edited by G. Schubert, U. S. National Report, 1991-1994 (Amer. Geophys. Union, Washington, DC), p. 365.
- DeMets, C., R. G. Gordon, D. F. Argus, and S. Stein, 1990, *Geophys. J. Int.* **101**, 425.
- DeMets, C., R. G. Gordon, D. F. Argus, and S. Stein, 1994, *Geophys. Res. Lett.* **21**, 2191.
- Dreyer, J. L. E., 1888, *Memoirs of Roy. Astron. Soc.* **48**.
- Edge, D. O., J. R. Shakeshaft, W. B. McAdam, J. E. Baldwin, and S. Archer, 1959, *Mem. Roy. Astron. Soc.* **68**, 37.
- Einstein, A., 1911, in *The Principle of Relativity*, (Dover, New York 1952 republication of paper in *Ann. Phys. (Leipzig)* **35**).
- Einstein, A., 1916, in *The Principle of Relativity*, (Dover, New York 1952 republication of paper in *Ann. Phys. (Leipzig)* **49**).
- Elgered, G., 1993, in *Atmospheric Remote Sensing by Microwave Radiometry*, edited by M. Janssen (Wiley, New York), Chap. 5.
- Elgered, G., J. L. Davis, T. A. Herring, and I. I. Shapiro, 1991, *J. Geophys. Res.* **96**, 6541.
- Estefan, J. A., and O. J. Sovers, 1994, *A Comparative Survey of Current and Proposed Tropospheric Refraction-Delay Models for DSN Radio Metric Data Calibration*, Jet Propulsion Laboratory Publ. 94-24, Pasadena, CA.
- Eubanks, T. M., 1991, Ed., *Proceedings of the U. S. Naval Observatory Workshop on Relativistic Models for Use in Space Geodesy* (U. S. Naval Observatory, Washington, DC).
- Eubanks, T. M., 1993, in *Contributions of Space Geodesy to Geodynamics: Earth Dynamics*, edited by D. E. Smith and D. L. Turcotte, Geodynamics Series, Vol. 24 (Amer. Geophys. Union, Washington, DC), p. 1.
- Eubanks, T. M., D. N. Matsakis, F. J. Joesties, B. A. Archinal, K. A. Kingham, J. O. Martin, D. D. McCarthy, S. A. Klioner, and T. A. Herring, 1996, in *Proceedings of IAU Symposium 166: Astronomical and Astrophysical Objectives of Sub-milliarcsecond Optical Astrometry*, edited by E. Hog and P. K. Seidelmann (Kluwer, Dordrecht), p. 283.
- Eubanks, T. M., J. A. Steppe, and O. J. Sovers, 1985, in *Proceedings of the International Conference on Earth Rotation and the Terrestrial Reference Frame*, Ohio State University, Columbus, Ohio, Vol. 1, p. 326.
- European Space Agency, 1997, *The Hipparcos and Tycho Catalogues*, sci. coord. M. A. C. Perryman, ESA SP-1200.
- Fairhead, L., and P. Bretagnon, 1990, *Astron. Astrophys.* **229**, 240.
- Fallon, F. W., and W. H. Dillinger, 1992, *J. Geophys. Res.* **97**, 2179.
- Fang, M., B. H. Hager, and T. A. Herring, 1996, *Geophys. Res. Lett.* **23**, 1493.
- Fanselow, J. L., 1976, Jet Propulsion Laboratory IOM 315.2.011, Pasadena, CA.
- Fanselow, J. L., 1983, *Observation Model and Parameter Partial for the JPL VLBI Parameter Estimation Software "MAS-TERFIT" - V1.0*, Jet Propulsion Laboratory Publ. 83-39, Pasadena, CA.
- Fey, A. L., A. W. Clegg, and E. B. Fomalont, 1996, *Astrophys. J. Suppl. Ser.* **105**, 299.
- Fich, M., L. Blitz, and A. A. Stark, 1989, *Astrophys. J.* **342**, 272.
- Fleagle, R. G., and J. A. Businger, 1980, *Atmospheric Physics*, 2nd Edition (Academic Press, New York).
- Folkner, W. M., P. Charlot, M. H. Finger, J. G. Williams, O. J. Sovers, X X Newhall, and E. M. Standish, 1994, *Astron. Astrophys.* **287**, 279.
- Freedman, A. P., J. A. Steppe, J. O. Dickey, T. M. Eubanks, and L.-Y. Sung, 1994, *J. Geophys. Res.* **99**, 6981.
- Fricke, W., 1977, *Veroeffentl. Astron. Rechen-Institut, Heidelberg*, vol. 28 (G. Braun, Karlsruhe, Germany).
- Fricke, W., H. Schwan, and T. Lederle, 1988, *Veroeffentl. Astron. Rechen-Institut, Heidelberg*, vol. 32 (G. Braun, Karlsruhe, Germany).
- Fu, L. L., E. J. Christensen, C. A. Yamarone, M. Lefebvre, Y. Menard, and P. Escudier, 1994, *J. Geophys. Res.* **99**, 24369.
- Fukushima, T., 1994, *Astron. Astrophys.* **291**, 320.
- Fukushima, T., M. K. Fujimoto, H. Kinoshita, and S. Aoki, 1986, *Celestial Mechanics* **38**, 215.
- Gallini, T. E., 1994, *A Survey of Tropospheric Refraction Models* (Aerospace Corp., El Segundo, CA), Report TOR-94(4488)-11.
- Gardner, C. S., 1976, *Radio Science*, **11**, 1037.
- Gardner, C. S., 1977, *Appl. Optics*, **16**, 2427.
- Gaspar, P., and R. M. Ponte, 1997, *J. Geophys. Res.* **102**, 961.
- Gilbert, F., and A. M. Dziewonski, 1975, *Phil. Trans. Roy. Soc. London* **A278**, 187.
- Gipson, J. M., 1996, *J. Geophys. Res.* **101**, 28051.
- Goad, C. C., 1983, in IAU, IUGG Joint Working Group on the Rotation of the Earth, "Project MERIT Standards", *United States Naval Observatory Circular No.167* (U. S. Naval Observatory, Washington, DC), p. A7-1.
- Gontier, A.-M., "Orientation de la Terre par Mesure VLBI", Ph. D. thesis, Observatoire de Paris, Paris, France, 1992.
- Goody, R. M., and Y. L. Yung, 1989, *Atmospheric Radiation: Theoretical Basis* (Oxford, New York), 2nd Ed., p. 10.
- Gross, R. S., 1993, *Geophys. Res. Lett.* **20**, 293.
- GSFC VLBI Group, 1981, *CALC for the HP 1000: Version 5.0*, Computer Management Branch Report, Goddard Space Flight Center, Greenbelt, MD.

- Gwinn, C. R., T. M. Eubanks, T. Pyne, M. Birkinshaw, and D. N. Matsakis, 1997, *Astrophys. J.* **485**, 87.
- Gwinn, C. R., T. A. Herring, and I. I. Shapiro, 1986, *J. Geophys. Res.* **91**, 4755.
- Haas, R., and H. Schuh, 1996, *Geophys. Res. Lett.* **23**, 1509.
- Hartmann, T., and M. H. Soffel, 1994, *Astron. J.* **108**, 1115.
- Hartmann, T., and H.-G. Wenzel, 1994, *Geophys. Res. Lett.* **21**, 1991.
- Hartmann, T., J. G. Williams, and M. H. Soffel, 1996, *Astron. J.* **111**, 1400.
- Hellings, R. W., 1986, *Astron. J.* **91**, 650; erratum *ibid.*, p. 1446.
- Henstock, D. R., I. W. A. Browne, P. N. Wilkinson, G. B. Taylor, R. C. Vermeulen, T. J. Pearson, and A. C. S. Readhead, 1994, *Astrophys. J. Suppl. Ser.* **100**, 1.
- Herring, T. A., 1988, quoted in *Bureau International de l'Heure Annual Report for 1987*, (Observatoire de Paris, Paris, France), p. D107.
- Herring, T. A., 1991, in *Proceedings of the 127th Colloquium of the IAU: Reference Systems*, edited by J. A. Hughes, C. A. Smith, and G. H. Kaplan (U. S. Naval Observatory, Washington, DC), p. 157.
- Herring, T. A., 1992, in *Refraction of Transatmospheric Signals in Geodesy*, edited by J. C. DeMunck and T. A. Th. Spoelstra, Netherlands Geodetic Commission, Publications on Geodesy, No. 36 (Delft, Netherlands), p. 157.
- Herring, T. A., 1995, *Revs. of Geophys. Suppl.* **33**, 345.
- Herring, T. A., B. E. Corey, C. C. Counselman, I. I. Shapiro, A. E. E. Rogers, A. E. Whitney, T. A. Clark, C. A. Knight, C. Ma, J. W. Ryan, B. R. Schupler, N. R. Vandenberg, G. E. Elgered, G. Lundqvist, B. O. Rönnang, J. Campbell, and P. Richards, 1983, in *Proceedings of the 9th International Symposium on Earth Tides*, edited by J. T. Kuo, (E. Schweitzerbartsche Verlagsbuchhandlung, Stuttgart), p. 205.
- Herring, T. A., J. L. Davis, and I. I. Shapiro, 1990, *J. Geophys. Res.* **95**, 12561.
- Herring, T. A., and D. Dong, 1994, *J. Geophys. Res.* **99**, 18051.
- Herring, T. A., C. R. Gwinn, and I. I. Shapiro, 1986, *J. Geophys. Res.* **91**, 4745.
- Hinteregger, H. F., I. I. Shapiro, D. S. Robertson, C. A. Knight, R. A. Ergas, A. R. Whitney, A. E. E. Rogers, J. M. Moran, T. A. Clark, and B. F. Burke, 1972, *Science* **178**, 396.
- Hirabayashi, H., M. Inoue, and H. Kobayashi, 1991, Eds., *Frontiers of VLBI*, (Universal Academy Press, Tokyo).
- Hirayama, Th., H. Kinoshita, M.-K. Fujimoto, and T. Fukushima, 1987, in *Proc. IAG Symposia at IUGG XIX General Assembly, Vancouver, Canada*, (Bureau Central de l'IAG, Paris, France), Tome I, p. 91.
- Hjellming, R. M., and R. C. Bignell, 1982, *Science* **216**, 1279.
- Ho, C. M., A. T. Mannucci, U. J. Lindqwister, X. Q. Pi, and B. T. Tsurutani, 1996, *Geophys. Res. Lett.* **23**, 3219.
- Hohenkerk, C. Y., B. D. Yallop, C. A. Smith, and A. T. Sinclair, 1992, in *Explanatory Supplement to the Astronomical Almanac*, edited by P. K. Seidelmann (University Science Books, Mill Valley, CA), p. 114.
- Holdridge, D., 1967, in *JPL Space Programs Summary 37-48, Vol. III: Supporting Research and Advanced Development*, Jet Propulsion Laboratory, Pasadena, CA, p. 2.
- Hosokawa, M., K. Ohnishi, and T. Fukushima, 1997, *Astron. J.* **114**, 1508.
- Houghton, J. T., 1986, *The Physics of Atmospheres* (Cambridge U. Press, NY), 2nd Ed.
- Hubble, E. P., 1929, *Proc. Natl. Acad. Sci.* **15**, 168.
- Ifadis, I., 1986, *The Atmospheric Delay of Radio Waves: Modeling the Elevation Dependence on a Global Scale* (Chalmers University of Technology, School of Electronic and Computer Engineering, Gothenburg, Sweden), Tech. Report No. 38L.
- International Astronomical Union, 1996, *Proceedings of the 22nd General Assembly, the Hague*, edited by I. Appenzeller (Kluwer, Dordrecht), p. 27.
- International Earth Rotation Service, 1989, *IERS Standards (1989), IERS Technical Note 3*, edited by D. D. McCarthy (Observatoire de Paris, Paris, France), p. 37.
- International Earth Rotation Service, 1992, *IERS Standards (1992), IERS Technical Note 13*, edited by D. D. McCarthy (Observatoire de Paris, Paris, France).
- International Earth Rotation Service, 1994, *Earth Orientation, Reference Frames and Atmospheric Excitation Functions submitted for the 1993 IERS Annual Report*, edited by P. Charlot (Observatoire de Paris, Paris, France).
- International Earth Rotation Service, 1996a, "1995 IERS Annual Report", (Observatoire de Paris, Paris, France).
- International Earth Rotation Service, 1996b, *IERS Conventions, IERS Technical Note 21*, edited by D. D. McCarthy (Observatoire de Paris, Paris, France).
- Jackson, J. D., 1975, *Classical Electrodynamics* (Wiley, New York), p. 517.
- Jacobs, C. S., 1988, Jet Propulsion Laboratory IOM 335.3-88-019, Pasadena, CA.
- Jacobs, C. S., 1991, Jet Propulsion Laboratory IOM 335.6-91-015, Pasadena, CA.
- Jacobs, C. S., and A. Rius, 1989, in *Proceedings of the 7th Working Meeting on European VLBI for Geodesy and Astrometry*, held at Madrid, Spain, October 26-27, p. 64.
- Jacobs, C. S., and A. Rius, 1990, Jet Propulsion Laboratory IOM 335.6-90-034, Pasadena, CA.
- Jacobs, C. S., O. J. Sovers, J. G. Williams, and E. M. Standish, 1993, "The Extragalactic and Solar System Celestial Frames: Accuracy, Stability, and Interconnection", in *Advances in Space Research*, **13**, p. (11)161.
- Jansky, K. G., 1932, *Proc. IRE* **20**, 1920.
- Jansky, K. G., 1933, *Nature* **132**, 66.

- Johnston, K. J., A. L. Fey, N. Zacharias, J. L. Russell, C. Ma, C. de Vegt, D. L. Jauncey, J. E. Reynolds, B. A. Archinal, M. S. Carter, T. E. Corbin, T. M. Eubanks, D. R. Florkowski, D. M. Hall, D. D. McCarthy, P. M. McCulloch, G. D. Nicolson, and D. B. Shaffer, 1995, *Astron. J.* **110**, 880.
- Kaplan, G. H., 1981, in *United States Naval Observatory Circular No. 163*, U. S. Naval Observatory, Washington, DC.
- Keihm, S. J., and K. A. Marsh, 1996, in *Telecommunications and Data Acquisition Prog. Rept. 42-127*, p. 1, Jet Propulsion Laboratory, Pasadena, CA.
- Kellermann, K. I., and I. I. K. Pauliny-Toth, 1981, *Ann. Rev. Astron. Astrophys.* **19**, 373.
- Kerr, F. J., and D. Lynden-Bell, 1986, *Mon. Not. R. Astron. Soc.* **221**, 1023.
- Kinoshita, H., 1977, *Celestial Mechanics* **15**, 277.
- Kinoshita, H., and J. Souchay, 1990, *Cel. Mech. and Dyn. Astron.* **48**, 187.
- Kogut, A., C. Lineweaver, G. F. Smoot, C. L. Bennett, A. Banday, N. W. Boggess, E. S. Cheng, G. De Amici, D. J. Fixsen, G. Hinshaw, P. D. Jackson, M. Janssen, P. Keegstra, K. Loewenstein, P. Lubin, J. C. Mather, L. Tenorio, R. Weiss, D. T. Wilkinson, and E. L. Wright, 1993, *Astrophys. J.* **419**, 1.
- Kondo, T., J. Amagai, Y. Koyama, and K. Heki, 1992, "Data Analysis of Geodetic VLBI Organized by the Communications Research Laboratory", Kashima Space Center Report, Kashima, Japan.
- Kovalevsky, J., L. Lindegren, M. Froeschle, F. Van Leeuwen, M. A. C. Perryman, J. L. Falin, F. Mignard, M. J. Penston, C. S. Petersen, P. L. Bernacca, B. Bucciarelli, F. Donati, R. Hering, E. Hog, M. G. Lattanzi, H. Van der Marel, H. Schrijver, and H. G. Walter, 1995, *Astron. Astrophys.* **304**, 34.
- Kunimori, H., F. Takahashi, M. Imae, Y. Sugimoto, T. Yoshino, T. Kondo, K. Heki, S. Hama, Y. Takahashi, H. Takaba, H. Kuchi, J. Amagai, N. Kurihara, H. Kuroiwa, A. Kaneko, Y. Koyama, and K. Yoshimura, 1993, in *Contributions of Space Geodesy to Geodynamics: Technology*, edited by D. E. Smith and D. L. Turcotte, Geodynamics Series, Vol. 25 (Amer. Geophys. Union, Washington, DC), p. 65.
- Lambeck, K., 1988, *Geophysical Geodesy* (Oxford, New York).
- Lang, K. R., 1980, *Astrophysical Formulae* (Springer, Berlin), p. 52.
- Lanyi, G. E., 1984, in *Telecommunications and Data Acquisition Prog. Rept. 42-78*, p. 152, Jet Propulsion Laboratory, Pasadena, CA.
- Larson, K. M., 1995, in *Dynamics of the Solid Earth and Other Planets*, edited by G. Schubert, U. S. National Report, 1991-1994 (Amer. Geophys. Union, Washington, DC), p. 371.
- Leavitt, H., 1912, in *Harvard College Observatory Circular 173*, (Harvard Univ., Cambridge, MA), 1.
- Lebach, D. E., B. E. Corey, I. I. Shapiro, M. I. Ratner, J. C. Webber, A. E. E. Rogers, J. L. Davis, and T. A. Herring, 1995, *Phys. Rev. Lett.* **75**, 1439.
- Le Mouél, J.-L., D. E. Smylie, and T. Herring, 1993, Eds., *Dynamics of Earth's Deep Interior and Earth Rotation*, Geophysical Monograph 72, IUGG Volume 12 (IUGG/AGU, Washington, DC).
- Le Provost, C., A. F. Bennett, and D. E. Cartwright, 1995, *Science*, **267**, 639.
- Lestrade, J.-F., D. L. Jones, R. A. Preston, R. B. Phillips, M. A. Titus, J. Kovalevsky, L. Lindegren, R. Hering, M. Froeschle, J.-L. Falin, F. Mignard, C. S. Jacobs, O. J. Sovers, M. Eubanks, and D. Gabuzda, 1995, *Astron. Astrophys.* **304**, 182.
- Lestrade, J.-F., A. E. E. Rogers, A. R. Whitney, A. E. Niell, R. B. Phillips, and R. A. Preston, 1990, *Astron. J.* **99**, 1663.
- Lieske, J. H., T. Lederle, W. Fricke, and B. Morando, 1977, *Astron. Astrophys.* **58**, 1.
- Linfield, R. P., 1995, Jet Propulsion Laboratory IOM 335.1-95-023, Pasadena, CA.
- Linfield, R. P., S. J. Keihm, L. P. Teitelbaum, S. J. Walter, M. J. Mahoney, R. N. Treuhaft, and L. J. Skjerve, 1996, *Radio Science*, **31**, 129.
- Lowe, S. T., 1992, *Theory of Post-Block II VLBI Observable Extraction*, Jet Propulsion Laboratory Publ. 92-7, Pasadena, CA.
- Ma, C., 1978, NASA Technical Memo 79582, Goddard Space Flight Center (Greenbelt, MD).
- Ma, C., J. W. Ryan, and D. S. Caprette, 1992, *Crustal Dynamics Project Data Analysis – 1991: VLBI Geodetic Results 1979-1990*, NASA Technical Memo 104552, Goddard Space Flight Center (Greenbelt, MD).
- Ma, C., and D. B. Shaffer, 1991, in *Proceedings of the 127th Colloquium of the IAU: Reference Systems*, edited by J. A. Hughes, C. A. Smith, and G. H. Kaplan (U. S. Naval Observatory, Washington, DC), p. 135.
- Ma, C., D. B. Shaffer, C. de Vegt, K. J. Johnston, and J. L. Russell, 1990, *Astron. J.* **99**, 1284.
- Ma, C., E. F. Arias, T. M. Eubanks, A. L. Fey, A.-M. Gontier, C. S. Jacobs, O. J. Sovers, B. A. Archinal, and P. Charlot, 1997, in *IERS Technical Note 23*, edited by C. Ma and M. Feissel (Observatoire de Paris, Paris, France).
- MacDoran, P. F., 1974, *Acta Astronautica* **1**, 1427.
- MacMillan, D. S., 1995, *Geophys. Res. Lett.* **22**, 1041.
- MacMillan, D. S., and J. M. Gipson, 1994, *J. Geophys. Res.* **99**, 18081.
- MacMillan, D. S., and C. Ma, 1997, *Geophys. Res. Lett.* **24**, 453.
- Manabe, S., T. Sato, S. Sakai, and K. Yokoyama, 1991, "Atmospheric Loading Effect on VLBI Observations", in *Proceedings of the AGU Chapman Conference on Geodetic VLBI: Monitoring Global Change*, NOAA Tech. Report NOS 137 NGS 49, p. 111.
- Marcaide, J. M., P. Elósegui, and I. I. Shapiro, 1994, *Astron. J.* **108**, 368.
- Marini, J. W., 1972, *Radio Science*, **7**, 223.
- Mathews, P. M., B. A. Buffett, T. A. Herring, and I. I. Shapiro, 1991, *J. Geophys. Res.* **96B**, 8219.

- Mathews, P. M., B. A. Buffett, and I. I. Shapiro, 1995, *Geophys. Res. Lett.* **22**, 579.
- Mathews, P. M., V. Dehant, and J. M. Gipson, 1997, *J. Geophys. Res.* **102**, 20469.
- May, J., and T. D. Carr, 1967, *Quart. J. Florida Acad. Sci.* **30**, 1.
- McGinnis, H., 1977, in *Deep Space Network Prog. Rept. 42-41*, Jet Propulsion Laboratory, Pasadena, CA, 218.
- Meeks, M. L., 1976, Ed., *Astrophysics: Radio Observations*, Vol. 12, Part C, Methods of Experimental Physics (Academic Press, New York), Chap. 5.
- Melbourne, W., R. Anderle, M. Feissel, R. King, D. McCarthy, D. Smith, B. Tapley, R. Vicente, 1983, Eds., *Project MERIT Standards*, United States Naval Observatory Circular No. 167 (U. S. Naval Observatory, Washington, DC).
- Melbourne, W., R. Anderle, M. Feissel, R. King, D. McCarthy, D. Smith, B. Tapley, R. Vicente, 1985, Eds., *Project MERIT Standards*, United States Naval Observatory Circular No. 167, Update #1 (U. S. Naval Observatory, Washington, DC).
- Melbourne, W. G., J. D. Mulholland, W. L. Sjogren, and F. M. Sturms, Jr., 1968, Jet Propulsion Laboratory Technical Report 32-1306, Pasadena, CA.
- Melchior, P., 1966, *The Earth Tides* (Pergamon, New York), p. 114.
- Melchiorri, B., and F. Melchiorri, 1990, in *The Cosmic Microwave Background: 25 Years Later*, edited by N. Mandolesi and N. Vittorio, (Kluwer, Dordrecht), p. 241.
- Menard, H. W., 1986, *The Ocean of Truth* (Princeton U. Press, Princeton, NJ).
- Mendes, V. B., and R. B. Langley, 1994, *A Comprehensive Analysis of Mapping Functions in Modeling Tropospheric Propagation Delay in Space Geodetic Data*, paper presented at KIS94, International Symposium on Kinematic Systems in Geodesy, Geomatics and Navigation, Banff, Canada, Aug. 30 - Sept. 2.
- Minster, J. B., and T. H. Jordan, 1978, *J. Geophys. Res.* **83**, 5331.
- Misner, C. W., K. S. Thorne, and J. A. Wheeler, 1973, *Gravitation* (W. H. Freeman, New York).
- Mitrovica, J. X., J. L. Davis, and I. I. Shapiro, 1993, *Geophys. Res. Lett.* **20**, 2387.
- Moran, J. M., 1976, in *Astrophysics: Radio Observations*, edited by M. L. Meeks, Vol. 12, Part C, Methods of Experimental Physics (Academic Press, New York), pp. 174, 228.
- Moran, J. M., P. P. Crowther, B. F. Burke, A. H. Barrett, A. E. E. Rogers, J. A. Ball, J. C. Carter, and C. C. Bare, 1967, *Science* **157**, 676.
- Morgan, P. J., R. W. King, and I. I. Shapiro, 1985, *J. Geophys. Res.* **90**, 12645.
- Moyer, T. D., 1971, Jet Propulsion Laboratory Technical Report 32-1527, Pasadena, CA, p. 12.
- Moyer, T. D., 1981, *Cel. Mech.* **23**, 33.
- Napier, P. J., D. S. Bagri, B. G. Clark, A. E. E. Rogers, J. D. Romney, A. R. Thompson, and R. C. Walker, 1994, *Proc. IEEE* **82**, 658.
- Naudet, C. J., 1994, private communication.
- Naudet, C. J., 1995, *Eos Trans. AGU*, **76**, S92.
- NEOS Annual Report for 1993*, 1994, U. S. Naval Observatory (Washington, DC).
- Newhall, X X, Preston, R. A., and Esposito, P. B., 1986, in *Astrometric Techniques, Proceedings of IAU Symposium 109*, edited by H. K. Eichhorn and R. J. Leacock (Reidel, Dordrecht).
- Niell, A. E., 1996, *J. Geophys. Res.* **101**, 3227.
- Nothnagel, A., M. Pilhatsch, and R. Haas, 1995, in *Proceedings of the 10th Working Meeting on European VLBI for Geodesy and Astrometry*, held at Matera, Italy, May 24-26, 1995.
- Ong, K. M., P. F. MacDoran, J. B. Thomas, H. F. Fliegel, L. J. Skjerve, D. J. Spitzmesser, P. D. Batelaan, and S. R. Paine, 1976, *J. Geophys. Res.* **81**, 3587.
- Ortega-Molina, A., 1985, "Détermination du Centre de Phase du Radiotélescope de Nançay pour les Observations VLBI", Report of Observatoire de Paris-Meudon (Meudon, France).
- Pagiatakis, S. D., 1982, *Ocean Tide Loading, Body Tide and Polar Motion Effects on Very Long Baseline Interferometry*, (Dept. of Surveying Engineering, University of New Brunswick Fredericton, N. B., Canada), Technical Report No. 92.
- Pagiatakis, S. D., 1990, *Geophys. J. Int.* **103**, 541.
- Pagiatakis, S. D., R. B. Langley, and P. Vanicek, 1982, presented at the 3rd International Symposium on the Use of Artificial Satellites for Geodesy and Geodynamics (National Technical University, Athens, Greece).
- Patnaik, A., I. W. A. Browne, P. N. Wilkinson, and J. M. Wrobel, 1992, *Mon. Not. R. Astron. Soc.*, **254**, 655.
- Peltier, W. R., 1995, *Geophys. Res. Lett.* **22**, 465.
- Petrov, L. Yu., 1995, *Secondary Data Analysis of VLBI Observations*, (Institute of Applied Astronomy, Russian Academy of Sciences, St. Petersburg, Russia), Reports No. 74-76.
- Piner, B. G., and K. E. Kingham, 1997, *Astrophys. J.* **479**, 684.
- Polatidis, A. G., P. N. Wilkinson, W. Xu, A. C. S. Readhead, T. J. Pearson, G. B. Taylor, and R. C. Vermeulen, 1995, *Astrophys. J. Suppl. Ser.* **98**, 1.
- Pooley, G., 1976, in *Astrophysics: Radio Observations*, edited by M. L. Meeks, Vol. 12, Part C, Methods of Experimental Physics (Academic Press, New York), p. 158.
- Pyne, T., C. R. Gwinn, M. Birkinshaw, T. M. Eubanks, and D. N. Matsakis, 1996, *Astrophys. J.* **465**, 566.
- Rabbel, W., and H. Schuh, 1986, *J. Geophysics* **59**, 164.
- Ray, J. R., 1991, *Revs. of Geophys. Suppl.* **29**, 148.

- Ray, J. R., C. Ma, J. W. Ryan, T. E. Clark, R. J. Eanes, M. M. Watkins, B. E. Schutz, and B. D. Tapley, 1991, *Geophys. Res. Lett.* **18**, 231.
- Ray, R. D., D. J. Steinberg, B. F. Chao, and D. E. Cartwright, 1994, *Science* **264**, 830.
- Reber, G., 1940, *Astrophys. J.* **91**, 621.
- Reber, G., 1944, *Astrophys. J.* **100**, 279.
- Reid, M. J., 1993, *Ann. Rev. Astron. Astrophys.* **31**, 345.
- Resch, G. M., 1984, in *Geodetic Refraction: Effects of Electromagnetic Wave Propagation Through the Atmosphere*, edited by F. K. Brunner (Springer, Berlin), p. 53.
- Rius, A., N. Zarraoa, E. Sardon, and C. Ma, 1992, *Bull. Geod.* **66**, 21.
- Robertson, D. S., 1975, "Geodetic and Astrometric Measurements with Very Long Baseline Interferometry", Ph. D. Thesis, M.I.T. Also available as NASA GSFC X-document # X-922-77-228 and NOAA reprint, National Geodetic Information Center, Silver Spring, MD, 1985.
- Robertson, D. S., 1987, *Revs. of Geophys.* **25**, 867.
- Robertson, D. S., 1991, *Rev. Mod. Phys.* **63**, 899.
- Robertson, D. S., and W. E. Carter, 1984, *Nature* **310**, 572.
- Robertson, D. S., W. E. Carter, and W. H. Dillinger, 1991, *Nature* **349**, 768.
- Robertson, D. S., F. W. Fallon, and W. E. Carter, 1986, *Astron. J.* **91**, 1456.
- Robinson, J. H., and J. Muirden, 1979, *Astronomy Data Book*, (Wiley, New York), pp. 38, 258.
- Rogers, A. E. E., 1970, *Radio Science* **5**, 1239.
- Rogers, A. E. E., 1975, "A Receiver Phase and Group Delay Calibrator for Use in Very Long Baseline Interferometry", *Haystack Observatory Tech. Note*, Haystack Observatory, Westford, MA.
- Rogers, A. E. E., 1976, in *Astrophysics: Radio Observations*, edited by M. L. Meeks, Vol. 12, Part C, Methods of Experimental Physics (Academic Press, New York), p. 139.
- Rogers, A. E. E., 1991, in *Proceedings of the AGU Chapman Conference on Geodetic VLBI: Monitoring Global Change*, NOAA Tech. Report NOS 137 NGS 49, p. 1.
- Rogers, A. E. E., R. J. Cappalo, H. F. Hinteregger, J. I. Levine, E. F. Nesman, J. C. Webber, A. R. Whitney, T. A. Clark, C. Ma, J. Ryan, B. E. Corey, C. C. Counselman, T. A. Herring, I. I. Shapiro, C. A. Knight, D. B. Shaffer, N. R. Vandenberg, R. Lacasse, R. Mauzy, B. Rayhrer, B. R. Schupler, and J. C. Pigg, 1983, *Science* **219**, 51.
- Rosen, R. D., and D. A. Salstein, 1985, *J. Geophys. Res.* **90**, 8033.
- Ryan, J. W., C. Ma, and J. M. Gipson, 1997, submitted to *J. Geophys. Res.*
- Saastamoinen, J., 1972, "Atmospheric Correction for the Troposphere and Stratosphere in Radio Ranging of Satellites", in *The Use of Artificial Satellites for Geodesy*, edited by S. W. Hendrickson, A. Mancini and B. H. Chovitz, Geophys. Monograph 15, Amer. Geophys. Union, Washington, DC.
- Salzberg, I. M., 1967, "Mathematical Relationships of MFOD Antenna Axes", NASA GSFC Report TM-X-55956 (accession # N67-39334), Goddard Space Flight Center, Greenbelt, MD.
- Scherneck, H. G., 1983, *Crustal Loading Affecting VLBI Sites* (University of Uppsala, Institute of Geophysics, Dept. of Geodesy, Uppsala, Sweden), Report No. 20.
- Scherneck, H. G., 1991, *Geophys. J. Int.* **106**, 677.
- Scherneck, H. G., 1993, private communication.
- Schmidt, M., 1963, *Nature* **197**, 1040.
- Seidelmann, P. K., 1982, *Celestial Mechanics* **27**, 79.
- Seidelmann, P. K., B. Guinot, and L. E. Doggett, 1992, in *Explanatory Supplement to the Astronomical Almanac*, edited by P. K. Seidelmann (University Science Books, Mill Valley, CA), p. 39.
- Seiler, U., and J. Wunsch, 1995, *Astron. Nachr.* **316**, 419.
- Shahid-Saless, B., R. W. Hellings, and N. Ashby, 1991, *Geophys. Res. Lett.* **18**, 1139.
- Shapiro, I. I., 1964, *Phys. Rev. Lett.* **13**, 789.
- Shapiro, I. I., 1967, *Science* **157**, 806.
- Shapiro, I. I., 1976, in *Astrophysics: Radio Observations*, edited by M. L. Meeks, Vol. 12, Part C, Methods of Experimental Physics (Academic Press, New York), p. 261.
- Sigman, E. H., 1987, in *Telecommunications and Data Acquisition Prog. Rept. 42-92*, p. 86, Jet Propulsion Laboratory, Pasadena, CA.
- Smith, D. E., and D. L. Turcotte, 1993, Eds., *Contributions of Space Geodesy to Geodynamics: Crustal Dynamics*, Geodynamics Series, Vols. 23-25 (Amer. Geophys. Union, Washington, DC).
- Smith, E. K., and S. Weintraub, 1953, *Proc. IRE* **41**, 1035.
- Sonett, C. P., E. P. Kvale, A. Zakharian, M. A. Chan, and T. M. Demko, 1996, *Science* **273**, 100.
- Souchay, J., 1993, private communication.
- Souchay, J., and H. Kinoshita, 1996, *Astron. Astrophys.* **312**, 1017.
- Sovers, O. J., 1994, *Geophys. Res. Letters* **21**, 357.
- Sovers, O. J., C. D. Edwards, C. S. Jacobs, G. E. Lanyi, K. M. Liewer, and R. N. Treuhaft, 1988, *Astron. J.* **95**, 1647.
- Sovers, O. J., C. S. Jacobs, and R. S. Gross, 1993, *J. Geophys. Res.* **98**, 19959.

- Sovers, O. J., and C. S. Jacobs, 1996, *Observation Model and Parameter Partial for the JPL VLBI Parameter Estimation Software "MODEST" - 1996*, Jet Propulsion Laboratory Publ. 83-39, Rev. 6, Pasadena, CA.
- Sovers, O. J., and C. Ma, 1985, in *Telecommunications and Data Acquisition Prog. Rept. 42-83*, p. 101, Jet Propulsion Laboratory, Pasadena, CA.
- Spitzer, L., Jr., 1962, *Physics of Fully Ionized Gases*, (Interscience Publishers, New York).
- Standish, E. M., 1982, *Astron. Astrophys.* **114**, 297.
- Standish, E. M., and X X Newhall, 1995, in *Dynamics, Ephemerides, and Astrometry of Solar System Bodies*, Proceedings of IAU Symp. 172, Kluwer, Dordrecht.
- Steppe, J. A., S. H. Oliveau, and O. J. Sovers, 1994, "Earth Rotation Parameters from DSN VLBI: 1994", in *Earth Orientation, Reference Frames and Atmospheric Excitation Functions submitted for the 1993 IERS Annual Report*, edited by P. Charlot (Observatoire de Paris, Paris, France), p. R-19.
- Sullivan III, W. T., 1984, *The Early Years of Radio Astronomy*, (Cambridge U. Press, New York).
- Tatarski, V. I., 1961, *Wave Propagation in a Turbulent Medium*, (Dover, New York).
- Tausner, M. J., 1966, *General Relativity and its Effects on Planetary Orbits and Interplanetary Observations*, (Lincoln Laboratory, Massachusetts Institute of Technology, Cambridge, MA), Technical Report No. 425.
- Taylor, G. B., R. C. Vermeulen, T. J. Pearson, A. C. S. Readhead, D. R. Henstock, I. W. A. Browne, and P. N. Wilkinson, 1994a, in *Compact Extragalactic Radio Sources*, Proceedings of a workshop at Socorro, NM, Feb. 11-12, 1994, edited by J. A. Zensus and K. I. Kellermann.
- Taylor, G. B., R. C. Vermeulen, T. J. Pearson, A. C. S. Readhead, D. R. Henstock, I. W. A. Browne, and P. N. Wilkinson, 1994b, *Astrophys. J. Suppl. Ser.* **95**, 345.
- Teitelbaum, L. P., R. P. Linfield, G. M. Resch, S. J. Keihm, and M. J. Mahoney, 1996, *Geophys. Res. Letters* **23**, 3719.
- Thakkar, D. D., W. Xu, A. C. S. Readhead, T. J. Pearson, G. B. Taylor, R. C. Vermeulen, A. G. Polatidis, and P. N. Wilkinson, 1995, *Astrophys. J. Suppl. Ser.* **98**, 33.
- Thayer, G. D., 1974, *Radio Science* **9**, 803.
- Thomas, J. B., 1978, in *NASA DSN Progress Report 42-44*, Jet Propulsion Laboratory, Pasadena, CA, 63.
- Thomas, J. B., 1980, Jet Propulsion Laboratory Publ. 80-84, Pasadena, CA.
- Thomas, J. B., 1981, Jet Propulsion Laboratory Publ. 81-49, Pasadena, CA.
- Thomas, J. B., 1987, Jet Propulsion Laboratory Publ. 87-29, Pasadena, CA.
- Thomas, J. B., 1991, private communication.
- Thompson, A. R., J. M. Moran, and G. W. Swenson, Jr., 1986, *Interferometry and Synthesis in Radio Astronomy*, (Wiley, New York).
- Treuhaft, R. N., 1991, private communication.
- Treuhaft, R. N., and G. E. Lanyi, 1987, *Radio Science* **22**, 251.
- Treuhaft, R. N., and S. T. Lowe, 1991, *Astron. J.* **102**, 1879.
- Treuhaft, R. N., and J. B. Thomas, 1991, Jet Propulsion Laboratory IOM 335.6-91-016, Pasadena, CA.
- Turyshchev, S. G., 1996, *Relativistic Navigation: A Theoretical Foundation*, Jet Propulsion Laboratory Publ. 96-13, Pasadena, CA.
- Tushingham, A. M., and W. R. Peltier, 1991, *J. Geophys. Res.* **96**, 4497.
- Ulvestad, J. S., 1988, in *The Impact of VLBI on Astrophysics and Geophysics*, Proceedings of IAU Symp. 129, edited by M. J. Reid and J. M. Moran, Kluwer, Dordrecht, p. 429.
- van Dam, T. M., G. Blewitt, and M. B. Heflin, 1994, *J. Geophys. Res.* **99**, 23939.
- van Dam, T. M., and T. A. Herring, 1994, *J. Geophys. Res.* **99**, 4505.
- van Vleck, J. H., and D. Middleton, 1966, *Proc. IEEE*, **54**, 2.
- Vessot, R. F. C., 1976, in *Astrophysics: Radio Observations*, edited by M. L. Meeks, Vol. 12, Part C, Methods of Experimental Physics (Academic Press, New York), p. 198.
- Vigue, Y., S. M. Lichten, G. Blewitt, M. B. Heflin, and R. P. Malla, 1992, *Geophys. Res. Letters* **19**, 1487.
- Wade, C. M., 1970, *Astrophys. J.* **162**, 381.
- Wade, C. M., and K. J. Johnston, 1977, *Astron. J.* **82**, 791.
- Wahr, J. M., 1979, "The Tidal Motions of a Rotating, Elliptical, Elastic, and Oceanless Earth", (Ph. D. Thesis, University of Colorado, Boulder, CO).
- Wahr, J. M., 1981, *Geophys. J. Roy. Astron. Soc.* **64**, 705.
- Wahr, J. M., 1985, *J. Geophys. Res.* **90**, 9363.
- Walter, H. G., and C. Ma, 1994, *Astron. Astrophys.* **284**, 1000.
- Walter, H. G., and O. J. Sovers, 1996, *Astron. Astrophys.* **308**, 1001.
- Ward, S. N., 1988, *J. Geophys. Res.* **93**, 7716.
- Watkins, M. M., and R. J. Eanes, 1994, *J. Geophys. Res.* **99**, 18073.
- Webb, F. H., M. Bursik, T. Dixon, F. Farina, G. Marshall, and R. S. Stein, 1995, *Geophys. Res. Letters* **22**, 195.
- Wegener, A., 1912, *The Origin of Continents and Oceans*, (Dover, New York 1966 republication).
- Whitney, A. R., 1974, "Precision Geodesy and Astrometry Via Very-Long-Baseline Interferometry", Ph. D. Thesis, M.I.T.
- Williams, J. G., 1970a, in *JPL Space Programs Summary 37-62, Vol. II: The Deep Space Network*, Jet Propulsion Laboratory,

- Pasadena, CA, p. 49.
- Williams, J. G., 1970b, Jet Propulsion Laboratory IOM 391-109, Pasadena, CA.
- Williams, J. G., 1994, *Astron. J.* **108**, 711.
- Williams, J. G., 1995, *Astron. J.* **110**, 1420.
- Williams, J. G., X X Newhall, and J. O. Dickey, 1996, *Phys. Rev. D* **53**, 6370.
- Wilson, B. D., A. J. Mannucci, and C. D. Edwards, 1995, *Radio Science*, **30**, 639.
- Yahil, A., G. A. Tammann, and A. Sandage, 1977, *Astrophys. J.* **217**, 903.
- Yatskiv, Ya. S., A. N. Kur'janova, and M. M. Medvedsky, 1991, "Program Complex "Kiev-GR1" for Reduction of the VLBI Observations", Preprint ITF-91-37P, (Institute for Theoretical Physics, Kiev, Ukraine).
- Yoder, C. F., 1983, private communication.
- Yoder, C. F., 1984, private communication.
- Yoder, C. F., J. G. Williams, and M. E. Parke, 1981, *J. Geophys. Res.* **86**, 881.
- Zarraoa, N., A. Rius, E. Sardon, H. Schuh, and J. Vierbuchen, 1989, in *Proceedings of the 7th Working Meeting on European VLBI for Geodesy and Astrometry*, edited by A. Rius, Madrid, Spain, p. 92.
- Zebker, H. A., P. Rosen, R. M. Goldstein, A. Gabriel, and C. L. Werner, 1994, *J. Geophys. Res.* **99**, 19617.
- Zensus, J. A., and T. J. Pearson, 1987, Eds., *Superluminal Radio Sources*, (Cambridge U. Press, New York).
- Zhu, S. Y., and E. Groten, 1989, *Astron. J.* **98**, 1104.
- Zhu, S. Y., E. Groten, and Ch. Reigber, 1990, *Astron. J.* **99**, 1024.
- Zombeck, M. V., 1990, *Handbook of Space Astronomy and Astrophysics* (Cambridge U. Press, NY), 2nd Ed., p. 286.

TABLE I. Maximum Magnitudes and Present Uncertainties of Portions of the VLBI Delay Model (mm).

Model component	Maximum delay	Present model uncertainty
BASELINE GEOMETRY		
Zero-order geometric delay	6×10^9	...
Earth orbital motion	6×10^5	1
Gravitational delay	2×10^3	2
STATION POSITIONS		
Tectonic motion	100	1
Tidal motion	500	3
Non-tidal motion	50	5
EARTH ORIENTATION		
UTPM	2×10^4	2
Nutation/precession	3×10^5	3
SOURCE STRUCTURE	50	10
ANTENNA STRUCTURE	10^4	10
INSTRUMENTATION	3×10^5	5
ATMOSPHERE		
Ionosphere	10^3	1
Troposphere	2×10^4	20

TABLE II. Tectonic Plate Rotation Velocities: NNR-Nuvel-1A Model (Units are nanoradians/year).

Plate	ω_x	ω_y	ω_z
Africa	0.891	-3.099	3.922
Antarctica	-0.821	-1.701	3.706
Arabia	6.685	-0.521	6.760
Australia	7.839	5.124	6.282
Caribbean	-0.178	-3.385	1.581
Cocos	-9.705	-21.605	10.925
Eurasia	-0.981	-2.395	3.153
India	6.670	0.040	6.790
Juan de Fuca	5.200	8.610	-5.820
Nazca	-1.532	-8.577	9.609
North America	0.258	-3.599	-0.153
Pacific	-1.510	4.840	-9.970
Philippine	10.090	-7.160	-9.670
Rivera	-9.390	-30.960	12.050
Scotia	-0.410	-2.660	-1.270
South America	-1.038	-1.515	-0.870

TABLE III. Frequency Dependent Solid Earth Tide Parameters.

Component k	h_2^k	H_k (mm)
ψ_1 (166554)	0.937	3
(165565)	0.514	50
K_1 (165555)	0.520	369
(165545)	0.526	-7
P_1 (163555)	0.581	-122
O_1 (145555)	0.603	-262

TABLE IV. Lunar Node Companions to Ocean Tides.

i Component	n_{ki} Companion	r_{ki} : Relative Amplitude
K_2 (275555)	-1	-0.0128
	+1	+0.2980
	+2	+0.0324
S_2 (273555)	-1	+0.0022
M_2 (255555)	-2	+0.0005
	-1	-0.0373
N_2 (245655)	-1	-0.0373
K_1 (165555)	-1	-0.0198
	+1	+0.1356
	+2	-0.0029
P_1 (163555)	-1	-0.0112
O_1 (145555)	-2	-0.0058
	-1	+0.1885
Q_1 (135655)	-2	+0.0057
	-1	+0.1884
M_f (075555)	+1	+0.4143
	+2	+0.0387
M_m (065455)	-1	-0.0657
	+1	-0.0649
S_{sa} (057555)	+1	-0.0247

 TABLE V. Ocean Tidally Induced Periodic Variations in Polar Motion (Sovers *et al.*, 1993).

Index i	Tide, period (hours)	Argument coefficient							A_{i1}	B_{i1} (μ as)	A_{i2}	B_{i2}	A_{i3} (0.1μ s)	B_{i3}
		k_{i1}	k_{i2}	k_{i3}	k_{i4}	k_{i5}	n_j							
1	K_2 11.967	0	0	0	0	0	-2	-2	65	44	-57	-9	26	
2	S_2 12.000	0	0	2	-2	2	-2	101	166	126	-89	-4	52	
3	M_2 12.421	0	0	2	0	2	-2	26	283	247	-2	-104	149	
4	N_2 12.658	1	0	2	0	2	-2	-15	56	19	-11	-23	20	
5	K_1 23.934	0	0	0	0	0	-1	-583	-2780	-2950	376	35	151	
6	P_1 24.066	0	0	2	-2	2	-1	154	46	42	-17	-32	-64	
7	O_1 25.819	0	0	2	0	2	-1	242	-152	2	-30	-135	-166	
8	Q_1 26.868	1	0	2	0	2	-1	72	-32	26	7	-40	-53	

TABLE VI. Solar System Velocity Relative to Various Standards of Rest.

Reference	Velocity (km/s)	l (deg)	b (deg)
Local standard of rest ^a	20 ± 1	57	23
Galactic center ^{a,b}	240 ± 5	90	0
Local Group ^c	308 ± 23	105	-7
Cosmic microwave background ^d	370 ± 3	264	48

^a Kerr and Lynden-Bell (1986)

^b Fich *et al.* (1989)

^c Yahil *et al.* (1977)

^d Kogut *et al.* (1993)

TABLE VII. Plasma Effects.

Plasma	$\rho(e/m^3)$	ν_p (kHz)	(ν_p/ν_S)	(ν_p/ν_X)
Earth	10^{12}	8980	4×10^{-3}	10^{-3}
Interplanetary	10^{10}	898	4×10^{-4}	10^{-4}
Interstellar	10^7	28	1×10^{-5}	3×10^{-6}

TABLE VIII. Electron Gyrofrequency Effects.

Magnetic field	B (gauss)	ν_g (kHz)	(ν_g/ν_S)	(ν_g/ν_X)
Earth	0.3	840	4×10^{-4}	10^{-4}
Interplanetary	10^{-5}	0.028	1.2×10^{-8}	3×10^{-9}
Interstellar	10^{-6}	0.003	1.2×10^{-9}	3×10^{-10}

TABLE IX. Sensitivity of Tropospheric Delay to Lanyi Mapping Function Parameters.

Parameter	Standard value	Sensitivity (6°)
T_0	292 K	-7 mm/K
W	6.8165 K/km	20 mm/K/km
h_1	1.25 km	-20 mm/km
h_2	12.2 km	5 mm/km